Experimental Investigations on Mechanical Properties, Smart Functional Capabilities and Corrosion Behavior of Friction Stir Welded Nitinol Shape Memory Alloys

Ph.D. Thesis

By

S. S. MANI PRABU

DISCIPLINE OF METALLURGY ENGINEERING AND MATERIALS SCIENCE

INDIAN INSTITUTE OF TECHNOLOGY INDORE

JULY 2019

Experimental Investigations on Mechanical Properties, Smart Functional Capabilities and Corrosion Behavior of Friction Stir Welded Nitinol Shape Memory Alloys

A THESIS

Submitted in partial fulfillment of the requirements for the award of the degree

of

DOCTOR OF PHILOSOPHY

by

S. S. MANI PRABU

DISCIPLINE OF METALLURGY ENGINEERING AND MATERIALS SCIENCE

INDIAN INSTITUTE OF TECHNOLOGY INDORE

JULY 2019

ACKNOWLEDGEMENTS

I am grateful to my thesis supervisor **Dr. I. A. Palani** for his eminent guidance and support throughout the PhD program. He has constantly motivated and aided me with necessary facilities to successfully complete the work in stipulated tenure. His consistent discussions have yielded fruitful suggestions and ideas to carry out the thesis work in a comprehensive way. I am thankful to my former co-supervisor **Dr. M. Anbarasu** for his suggestions and support.

I would like to thank **Prof. Pradeep Mathur**, Director, IIT Indore and **Dr. Parasharam M. Shirage**, Head of the department, Metallurgy Engineering and Materials Science for the opportunity and support to conduct my research. I thank the PSPC members **Dr. Santhosh S. Hosmani and Dr. Yuvraj K. Madhukar** for their valuable suggestions. I am thankful to DPGC convener **Dr. Rupesh Devan** and former PSPC members **Dr. Vipul Singh and Dr. Devendra Deshmukh** for their valuable comments and support during yearly comprehensive examinations.

I convey my sincere thanks to **Ministry of Human Resource and Development (MHRD)**, India for the teaching assistantship form June, 2015 to May, 2019. I am grateful to Japan Science and Technology Agency (JST) for the award of Sakura fellowship to visit Nagaoka Institute of Technology (NUT), Japan during 19-27 January 2019.

I am grateful to **Prof. Satish V. Kailas** of IISc Bangalore for providing the Friction Stir Welding facility. I thank the discipline of metallurgy engineering and materials science and sophisticated instrumentation center of IIT Indore for providing the necessary characterization facility. I am thankful to department of mechanical engineering and materials engineering of IISc Bangalore for providing the necessary support and facilities for successful completion of the work.

I would like to thank **Dr. H. C. Madhu and Dr. Chandra S. Perugu of IISc Bangalore** for their assistance during welding and characterization. I thank **Dr. K. Akash, Dr. R. Deepak Selvakumar and Mr. R. Mithun** for their research companionship throughout my PhD career. I am indebted to these great minds who have played an important role in shaping me as a researcher with great ideas and perseverance.

I am thankful to my research colleagues **Dr. S. Shiva, Dr. Tameshwer nath, Dr. Ashish K. Shukla, Mrs. Nandini Patra, Dr. P Rajagopalan, Mr. S Jayachandran, Mr. M Muralidharan, Mr. M Manikandan, Mr. D. Suresh, Mr. MS Arjun, Mr. Sarathkumar, Mr. Vijay Choyal** and **Mr. Gowthamraju.** I express my gratitude to **Mr. Ashutosh Jangde** of IISc Bangalore for his support and guidance during electrochemical corrosion testing. I acknowledge the support from **Mr. Aditya Litoria and Mr. Mayur Dhake** during WEDM and metallographic sample preparation. My sincere thanks to **Dr. Santhosh S. Hosmani**, Associate Professor, MEMS, IIT Indore and his PhD student **Mr. Manoj Joshi** for providing the facilities and support for performing SMAT. I am thankful to **Mr. Abhinav** and **Ms. Tulika** for their kind assistance during dynamic mechanical analysis. I am thankful to **Mr. Sachin Bhirodkar** and **Mr. Ashwin Wagh** of OMG group for their support. I would like to thank all the members of OMG and PCM laboratory for their affection and support.

I am thankful and indebted to my parents and sister’s family for showering me with endless love and support. Especially, I am thankful to my father **Mr. S. Sakthivelsamy** for his trust and constant motivation throughout my life which has enabled to be better person who I am today.

Dedicated to My Family and Friends

PREFACE

Welding of shape memory alloys without deterioration of shape memory effect could vastly extend their applications. To retain shape memory behavior, a solid-state welding technique called friction stir welding was employed in this study. NiTi alloy sheets of thickness 1.2 mm were joined at tool rotational speeds of 800, 1000, and 1200 rpm. Due to dynamic recrystallization, the grain refinement has occurred in the weld region. Interestingly, the weld produced at 1000 rpm had ultimate tensile strength of 638 MPa (66 % of the base metal) and yield strength of 602 MPa which is 17 % higher than the base metal. The weld at 1000 rpm has a crucial superelastic plateau near 600 MPa until 7.25 % strain while the weld at 800 rpm showed close to 460 MPa until 5 % strain. The phase transformation behavior of different weld regions was studied in detail using differential scanning calorimetry. A marginal drift in transformation temperatures was observed in the weld. To understand the drift in phase transformation temperatures, finite element analysis was carried out with focus on temperature distribution and strain rate experienced during welding.

The time-dependent shape recovery of a FSW welded joint was studied using bending-recovery method. It was found that the original position was completely recovered after 27 s at a temperature of 65^{o}C. Using thermomechanical evaluation, it was found that the laser actuation technique has yielded higher displacements and actuation speeds compared to the electrical actuation. The laser based method has demonstrated impulsive actuation characteristics due to the associated higher heating rates and temperatures than the electrical actuation. The corrosion characteristics of the weld and the influence of post peening methods on the corrosion behavior of the weld have been evaluated using electrochemical corrosion testing. The weld made at 800 rpm has better corrosion resistance with the lowest corrosion rate of 3.46 $\times 10^{-4}$ mm/year. In case of peened samples, the 1 hr SMAT has exhibited better corrosion resistance with the least corrosion rate of 1.295 $\times 10^{-4}$ mm/year.

LIST OF PUBLICATIONS

International Journals

1. **S. S. Mani Prabu,** Madhu H. C., Chandra S. Perugu, Akash K., Ajay Kumar P., Satish V. Kailas, Anbarasu Manivannan, Palani I.A., "Microstructure, mechanical properties and shape memory behaviour of friction stir welded nitinol", **Materials Science Engineering A 693, 233–236, 2017.**

2. **S. S. Mani Prabu,** Madhu H.C., Chandra S. Perugu, K. Akash, Mithun R., P. Ajay Kumar, Satish V. Kailas, Manivannan Anbarasu, I.A. Palani, "Shape memory effect, temperature distribution and mechanical properties of friction stir welded nitinol", **Journal of Alloys and Compounds 776, 334-345, 2019.**

3. **S. S. Mani Prabu,** Mithun R, M. Muralidharan, Tameshwer Nath, Brolin A, K. Akash, I.A.Palani, "Thermo-mechanical behavior of shape memory alloy spring actuated using novel scanning technique powered by ytterbium doped continuous fiber laser", **Smart Materials and Structures 28, 047001, 2019.**

4. **S. S. Mani Prabu,** Chandra S. Perugu, Madhu H.C., Ashutosh Jangde, P. Ajay Kumar, Satish V. Kailas, Sohel Khan,S. Jayachandran, M. Manikandan, I.A. Palani, "Exploring the Functional and Corrosion Characteristics of Friction Stir Welded NiTi Shape Memory Alloy", **Journal of Manufacturing Processes 47, 119-128, 2019.**

5. **S. S. Mani Prabu,** Chandra S. Perugu, Ashutosh Jangde, Madhu H.C., P. Ajay Kumar, Satish V. Kailas, Manivannan Anbarasu, I.A. Palani, "Influence of Friction Stir Processing and Surface Mechanical Attrition Treatment on Corrosion Behavior of NiTi Shape Memory Alloy", (**Under Preparation).**

6. **S. S. Mani Prabu**, Chandra S. Perugu, Ashutosh Jangde, Madhu H.C., Manoj Joshi, P. Ajay Kumar, Satish V. Kailas, Santosh S Hosmani, I.A. Palani, "Influence of Surface Mechanical Attrition Treatment and Laser Shock Peening on the Corrosion Characteristics of Friction Stir Welded NiTi Shape Memory Alloy", (**Under Preparation).**

International Conferences

1. **S. S. Mani Prabu,** I. A. Palani, "Exploring the Actuation Characteristics of Friction Stir Welded NiTi Shape Memory Alloy for Functional Applications", **10th ISSS National Conference on Micro and Smart Systems, NITTE, 2019.**

2. **S. S. Mani Prabu,** Madhu H. C., Chandra S. Perugu, Akash K., Satish V. Kailas, Anbarasu Manivannan, Palani I.A., **"**Phase Transformation Behaviour and Actuation Studies of Friction Stir Welded NiTi Shape Memory Alloy", **Indo Japan Bilateral Symposium on Futuristic Materials and Manufacturing, IIT Madras-NUT Japan**, **2018.**

3. **S. S. Mani Prabu,** Mithun R., Suhel Khan, Jayachandran S., Manikandan M., Yeshwanth Sai, M. Anbarasu3, I. A. Palani, "Influence of Perturbations on Actuation Characteristics of Friction Stir Welded Shape Memory Alloy", **All India Manufacturing Technology, Design and Research Conference, CEG Guindy**, **2018.**

4. **S. S. Mani Prabu,** M. L. Jothi Saravanan, M. Anbarasu, I. A. Palani, **"**Gas Metal Arc Welding (GMAW) of Pseudoelastic Nickel-Titanium Shape Memory Alloys", **International Conference on Precision, Meso, Micro and Nano Engineering, IIT Madras**, **2017.**

5. **S. S. Mani Prabu,** Madhu H. C., Chandra S. Perugu, Akash K., Ajay Kumar P., Satish V. Kailas, Anbarasu Manivannan, Palani I.A., **"**Friction Stir Welding of Nitinol: Microstructure, Mechanical and Shape Memory Properties", **International conference on advanced materials and processes, ISRO Trivandrum**, **2017.**

TABLE OF CONTENTS

LIST OF FIGURES

LIST OF TABLES

NOMENCLATURE

Symbol	Unit	Description
σ_S	MPa	Detwinning start stress
σ_f	MPa	Detwinning finish stress
μ	-	coefficient of friction
R_s	mm	Tool shoulder radius
F_n	kN	Plunge force
A_{shl}	mm^2	Shoulder surface area
n	RPM	Tool rotational speed
$\overline{Y}$	MPa	Average shear stress of the material
R_p	mm	Pin radius
ρ	Kg/m^3	Density
C_p	J/Kg K	Specific heat
u	mm/min	Welding speed
k	W/m K	Thermal conductivity
h	W/m^2 K	Heat transfer coefficient
ϵ	-	Surface emissivity
σ	-	Stefan-Boltzmann constant
η	$kgm^{-1}s^{-1}$	Dynamic viscosity
σ_e	MPa	Flow stress
ε	s^{-1}	Strain rate

ACRONYMS

S. No	Acronym	Expansion
1	SMA	Shape memory alloys
2	OWSME	One way shape memory effect
3	TWSME	Two way shape memory effect
4	SME	Shape memory effect
5	A_s	Austenite start temperature
6	A_f	Austenite finish temperature
7	M_s	Martensite start temperature
8	M_f	Martensite finish temperature
9	GTAW	Gas tungsten arc welding
10	SMAT	Surface mechanical attrition treatment
11	LSP	Laser shock peening
12	FZ	Fusion zone
13	HAZ	Heat affected zone
14	XRD	X-ray diffraction
15	DSC	Differential scanning calorimetry
16	SEM	Scanning electron microscopy
17	FEA	Finite element analysis
18	FSW	Friction stir welding
19	OCP	Open circuit potential
20	EIS	Electrochemical impedance spectroscopy
21	TMAZ	Thermo-mechanically affected zone
22	DMA	Dynamic mechanical analysis

Chapter 1

Introduction to Shape Memory Alloys and Necessity of Welding for Smart Functional Applications

1.1 Introduction to shape memory alloys

Shape memory alloys (SMA) are smart materials having distinctive behaviour such as shape memory effect and pseudoelasticity. A reversible solid state displacive phase transformation from austenite to martensite is the reason behind the smart behaviour [1,2]. SMAs are metallic alloys and categorised as NiTi based alloys (NiTi, NiTiCu), copper based alloys (CuZnAl, CuAlNi) and iron based alloys (FeNiCoTi, FeMnSi). The SMAs exhibit high actuation energy densities and have capabilities to recover their shape under large applied loads. However, the actuation frequencies are comparably low for SMAs due to the associated thermal inertia or slow dissipation of heat from the material during cooling. SMA thin films can exhibit better actuation frequencies compared to bulk materials due to the increased surface area to volume ratio. Fig. 1.1 shows the actuation energy densities and frequencies of different smart materials.

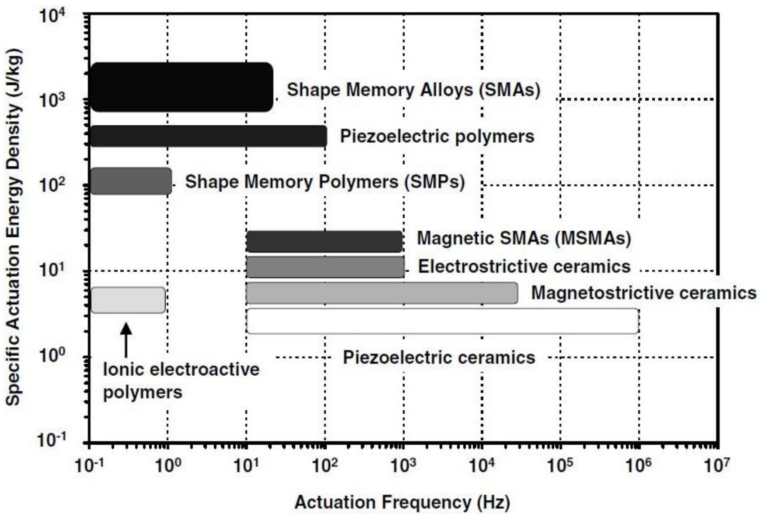

Fig. 1.1: Comparison diagram showing the actuation energy density and actuation frequency range of different smart materials [2]

SMAs can exist in two phases having three different crystal structures viz. twinned martensite, detwinned martensite and austenite. The martensite is a low temperature phase while the austenite is stable at high temperatures. The phase transformations have characteristic start and finish temperatures and gives information about the operating range of an alloy. M_s, M_f, A_s and A_f are the characteristic temperatures of the martensite and austenite transformations. Fig. 1.2 shows the stress-strain-temperature diagram of a SMA, crystal structures and the possible phase transformations. Moreover, it shows all the functional behaviour of a shape memory alloy viz. One way shape memory effect (OWSME), two way shape memory effect (TWSME) and pseudoelasticity. OWSME is widely explored and has been applied to variety of applications. However, the TWSME is less utilized for applications due to the intense training requirements and less strain recovery than OWSME [3]. The pseudoelastic behaviour of the SMA is explained in detail in section 1.3.

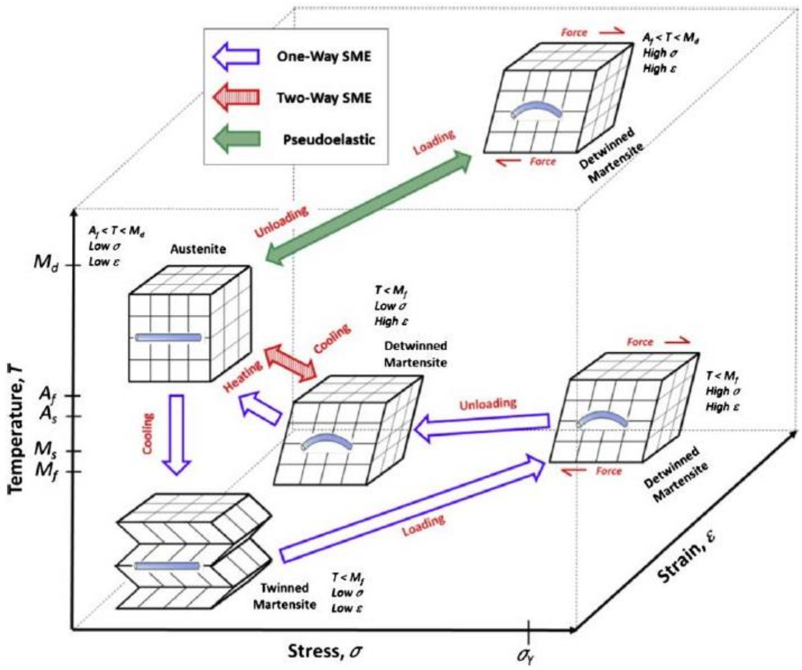

Fig. 1.2: SMA crystal structures and the resultant behaviour due to transformation [3]

1.2 One way shape memory effect

The shape memory alloys exhibits shape memory effect (SME) which is the property of remembering and recuperating their original shape upon thermal stimuli [4,5]. When a SMA is deformed at low temperature (below A_s), it can be switched to de-twinned martensite state through the application of load. The de-twinning process can be reversed by providing heat energy to the SMA. On supplying heat, the crystal arrangement of the SMA material absorbs energy and reorients itself from de-twinned martensite crystal structure to austenite crystal structure at a temperature above A_s. This change in the crystallographic plane is echoed on a macroscopic level, thus observing the shape recovery [6,7]. This phenomenon can be better explained through OWSME stress-strain-temperature diagram shown in Fig. 1.3. The diagram represents a thermomechanical loading path where σ is the stress and ε is the corresponding strain experienced by the NiTi specimen under uniaxial loading. The point A represents the parent phase austenite. At room temperature, the SMA specimen possesses twinned martensite crystal structure denoted as point B. The minimum and maximum stress required to deform the SMA is called de-twinning start stress (σ_S) and de-twinning finish stress (σ_f) respectively [2]. Due to the applied load, de-twinning of the martensite structure takes place. This de-twinning induces a deformation where the associated stress will be lesser than the plastic yield stress of martensite structure. On removal of the load, an elastic recovery happens (C-D) while retaining the detwinned martensite. Upon heating, the crystal structure begins to transform from detwinned martensite to austenite above austenite start temperature (A_s). The start and finish of this reverse transformation is denoted as E and F corresponding to temperatures A_s and A_f respectively. When the A_f is reached, the SMA will contain only the austenite phase. On cooling, the transformation from austenite to martensite happens without any shape change. This is called OWSME, because the shape change was attained only through heating. In order to get a cyclic behaviour of the SMA specimen, detwinning has to be initiated by an external mechanical load.

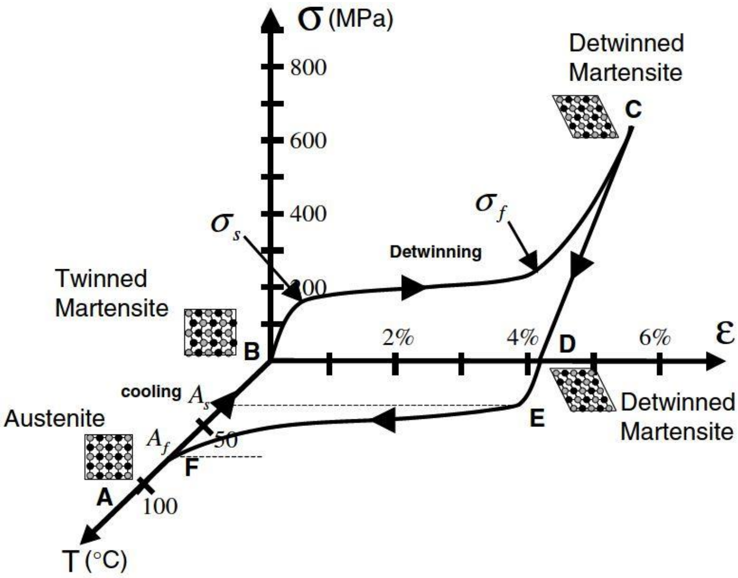

Fig. 1.3: Stress-strain-temperature diagram showing SME [2]

1.3 Pseudoelasticity

The pseudoelasticity effect or superelasticity is the strain recovery driven by stress induced martensite transformation (SIM) i.e. the SMA at temperatures above the austenite finish temperature (A_f) can recover the strain completely upon unloading [8]. At temperatures above A_f (stable austenite exists), the pseudoelastic path can initiate and develop under the application of external load which leads to formation of detwinned martensite state. On removal of load, the path reverses and stable austenite forms at no load condition or stress free state. The typical pseudoelastic behaviour of SMA is shown in Fig.1.4. On application of load, the initiation of martensite transformation happens after crossing the elastic loading (A-B). Between the onset and end of the martensite transformation, the SMA experience large inelastic strains (B-C). The completion of martensite transformation sets an elastic loading (C-D) which is nothing but the elastic deformation of detwinned martensite. When the load is removed, the austenite transformation takes place (E-F) and strain recovery happens. After crossing the austenite end stress state (σ_{Af}), the SMA will elastically deforms to the starting point A. The complete loading-unloading of a SMA will form a hysteresis curve and area of the curve represents the heat energy dissipated during the transformation.

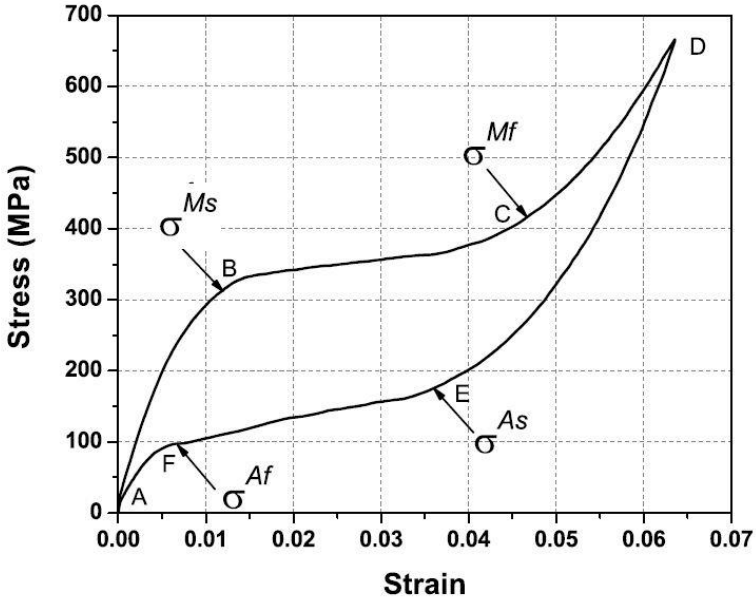

Fig. 1.4: Typical pseudoelastic behaviour attained through loading/unloading cycles [2]

1.4 Biocompatibility

The excellent combinations of pseudoelasticity and biocompatibility have attracted potential biomedical applications. Biocompatibility is the foremost requirement of biomedical grade materials. The biocompatible material should remain nontoxic for the entire functional period without causing any allergic or inflammatory reaction to the host organs or tissues of the human body. These materials have to encounter challenging corrosion environment inside the body. NiTi alloy have very good biocompatibility and the corrosion resistance is better than most alloys in biomedical industry [9,10]. The corrosive resistant titanium oxide layer forms over the NiTi alloy surface and prevents the leaching of harmful Ni ions in to the human body. The loading/unloading behaviour of a pseudoelastic NiTi alloy resembles the behaviour of bone or tissue of a human body i.e. the stress-strain behaviour of NiTi alloy is compatible with human body. Fig. 1.5 shows the stress strain behaviour of NiTi alloy in comparison with steel and bone. It shows the similarity between the bone and the NiTi alloy during loading and unloading cycles. The recoverable strain of steel is less than 0.5 % whereas the NiTi alloys have recoverable strain up to 8 %. The biocompatibility coupled with high recoverable strains, good kink resistance, steerability and torquability of NiTi SMA have made them a viable candidate for orthodontic wires, cardiovascular stents and orthopaedic implants (bone anchors, stables, spinal vertebra spacers etc.) [11,12]. Other surgical tools include biopsy forceps, basket for organ stone removal and laparoscopy tools [13].

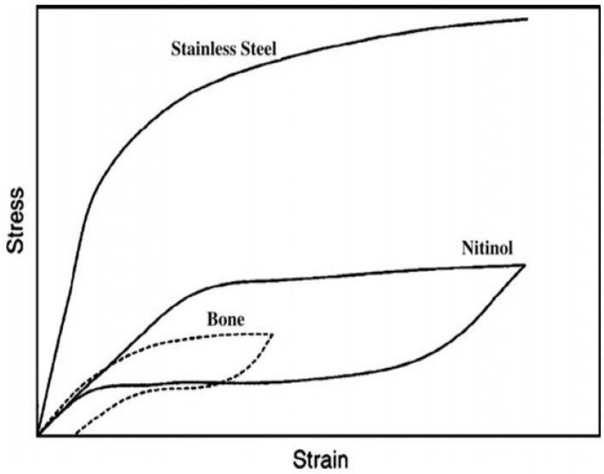

Fig. 1.5: Stress-strain behaviour of steel, bone and biocompatible NiTi alloy [10]

1.5 Nickel Titanium or NiTinol alloy

Nickel-Titanium or Nitinol alloys are widely used shape memory alloys (SMA) due to their exhibition of excellent mechanical properties, thermomechanical behaviour, pseudoelasticity and biocompatibility. They have highest work density and large deformation recovery among other SMA compositions [14]. It is the most studied SMA alloy system and has been applied in variety of commercial applications. In addition to mechanical properties, the transformation temperatures are one of the most important characteristics which decide the applicability of the SMA. The fabrication of NiTi alloy requires intense care to ensure close compositional tolerance [8]. NiTi alloys are available in standard forms of wires, sheets, tubes etc. The metallurgical process required to manufacture the NiTi alloy remains the same irrespective of the geometrical form. Due to the poor cold workability of NiTi alloy, hot working above 700ºC (forging, drawing etc.) is required to get the required dimensions. Shape memory treatment is the crucial part of the manufacturing process. There are two goals of shape memory treatment viz. to memorize the desired shape and secondly to control the transformation temperatures. Usually, the restrained NiTi alloy will be annealed in the range 300ºC to 500ºC for several minutes to hours. The steps involved during manufacturing and the process conditions significantly affect the mechanical properties and the transformation temperatures.

Equiatomic composition of NiTi can exhibit a maximum austenite finish temperature (A_f) of 120ºC. By changing the Ni composition, the transformation temperatures can be tailored based on the application. At the Ni composition of 51 %, it can exhibit a lowest A_f of -40ºC [2]. Based on the composition and the manufacturing conditions, the NiTi alloy can exhibit either shape memory effect or pseudoelasticity at room temperature.

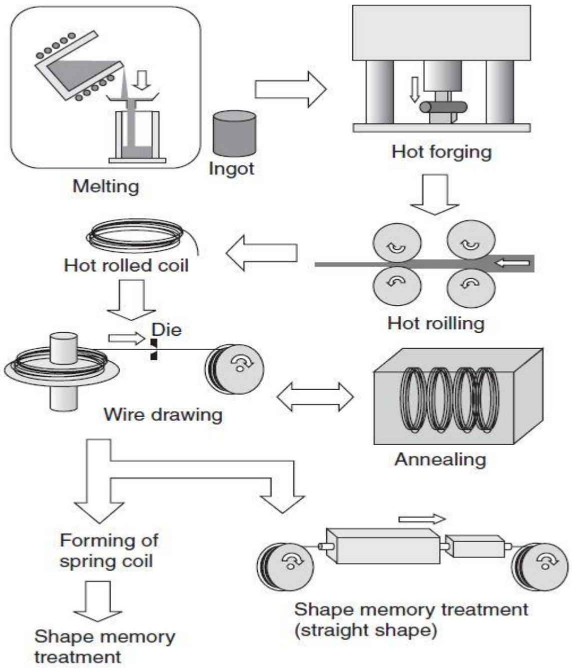

Fig. 1.6: Schematic showing the fabrication process of NiTi SMA [8]

1.6 Necessity, challenges and requirements in welding of nitinol

The applicability of these alloys are limited due to its low formability and poor machinability. Hence, the manufacturing of complex shapes tends to be difficult and expensive. Therefore, the welding becomes inevitable to fabricate NiTi SMA into different geometrical structures with adequate freedom of design. The welding of NiTi alloy is a challenging task as it requires not only the mechanical strength but also the preservation of shape memory effect in the weld. If the shape memory effect is not preserved in the weld, then the physical actuation of the welded structure becomes impossible and hampers the product application.

NiTi SMA is highly sensitive to microstructural and compositional changes. Hence, the welding of these alloys may leads to deterioration of the mechanical and shape memory properties. These changes during welding drastically alter the transformational temperatures and reduce the thermomechanical stability of the weld joint [15,16]. If the difference in transformational temperatures of the weld and the base metal is large, the welded SMA structures cannot be actuated at the same temperature and also makes the actuation control difficult. Moreover, the composition of the filler material if not correctly matched with the base metal will exponentially increase these issues. In order to overcome these challenges, a solid state welding process is on high demand which can weld NiTi alloys with minimal change in phase transformation temperatures, adequate mechanical integrity and retainment of shape memory properties in the weld.

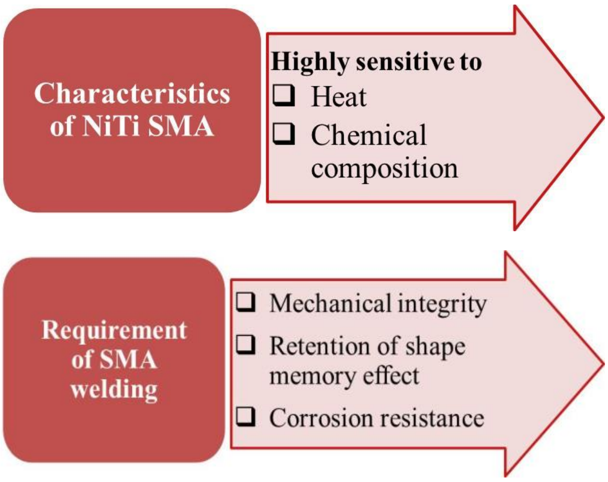

Fig. 1.7: Chart showing the characteristics of NiTi and requirements of SMA welding

1.7 Applications of the welded nitinol shape memory alloys

NiTi SMAs has been applied to various applications based on the requirement of either shape memory effect or pseudoelasticity. Some of the interesting

applications of welded structures are discussed in this section. The shape memory effect can be triggered thermally i.e. the increase in temperature will induce the shape recovery. This phenomenon of shape recovery favours the SMA to be used as actuators in automobile, aerospace and robotic applications [17,18]. Fig. 1.8 shows the SMA adaptive nozzle employed in Boeing aircraft. The SMA adaptive nozzle cannot be fabricated without the use of welding. Since, the nozzle is movable and requires more number of lifecycles, the use of rivets or fasteners cannot provide permanent close fit joints. Hence, the NiTi plate has been welded to the parent titanium structure. During take-off, the temperature from the nozzle will be high enough to actuate the NiTi alloy. The NiTi alloy pulls the entire structure downwards which acts as a protrusion and reduces the noise of the engine. After the aircraft reaches the cruise condition at high altitude, due to the change in engine and the environmental conditions the nozzle temperature drops. Then the parent titanium structure will act as the bias force and lift the structure back to its initial state [19,20]
.

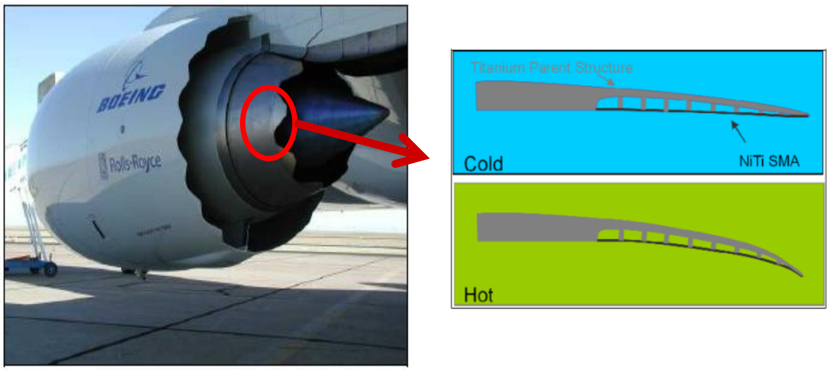

Fig. 1.8: SMA adaptive nozzle for noise abatement in Boeing aircraft [20]

Fig. 1.9 shows the conceptual design for multiway actuation of SMA structures. Here, there is a need to integrate two SMA plates with different phase transformation temperatures. Hence, the welding is the most prominent way to fabricate these multiway actuation structures. The welded structure can hold three different positions based on the temperature change. At room temperature (RT), the plates will be in straight position. When the temperature rises, then one of the plate whose austenite temperature lying in the range (40ºC to 50ºC) actuates. Upon further increase in the temperature, the other SMA plate will also actuate. The complete actuation of both sides corresponds to third position. This technology can be applied to morphing rotor blades where the each blade trained in different position can be welded to central hub. Based on the thermal and fluid flow conditions, the blade will bend accordingly and the resultant mechanical output from the rotor can be modified.

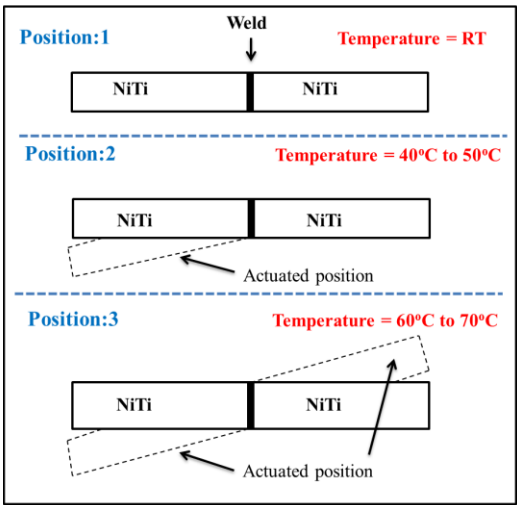

Fig. 1.9: Conceptual design for multiway actuation of SMA welded structures

The pseudoelasticity enables the SMA to be used in biomedical, impact absorption and various vibration damping applications [21]. It has been successfully applied to vibration damping of machines, buildings and bridges in the form of dampers, restrainers, bracing systems and concrete reinforcements [22,23]. Fig. 1.10 shows the SMA ring reinforced concrete blocks for seismic application. Initially, the SMA bar of diameter 3 mm and length 446 mm was strained up to 7 %. Then the strained SMA bar was bent in to circle and the edges were welded using gas tungsten arc welding (GTAW) process. Similar rings were connected over one another with a gap in between to form a ribbed cylinder. Then the concrete cylinders (Diameter-15 cm, Height- 30 cm) reinforced with SMA welded rings were made. The SMA ring reinforced in to concrete cylinders has shown better peak strength and failure strain compared to the plain concrete cylinders [24].

Fig. 1.10: Fabrication and testing of SMA reinforced concrete blocks for seismic applications [24]

Tatyane Ribeiro Mesquita et al. used resistance spot welding to weld rectangular NiTi wire with a round one [25]. Fig. 1.11a-b shows the welded stops in an orthodontic NiTi wire. Fig. 1.11c shows the patient teeth attached with NiTi wire having welded loops. Fig. 1.11d shows the teeth of the same patient after 30 days of fixing. To improve the product design of orthodontic wires used for tooth correction, it was proposed that small pieces of NiTi wires can be welded to levelling wire. These small pieces would act as hooks for binding elastics, omega loops or stops to assist the physician in tooth correction. The welding is the cost effective and faster way to fabricate rings of different dimensions and permanent attachments of loops to wire as shown in Fig. 1.10-1.11

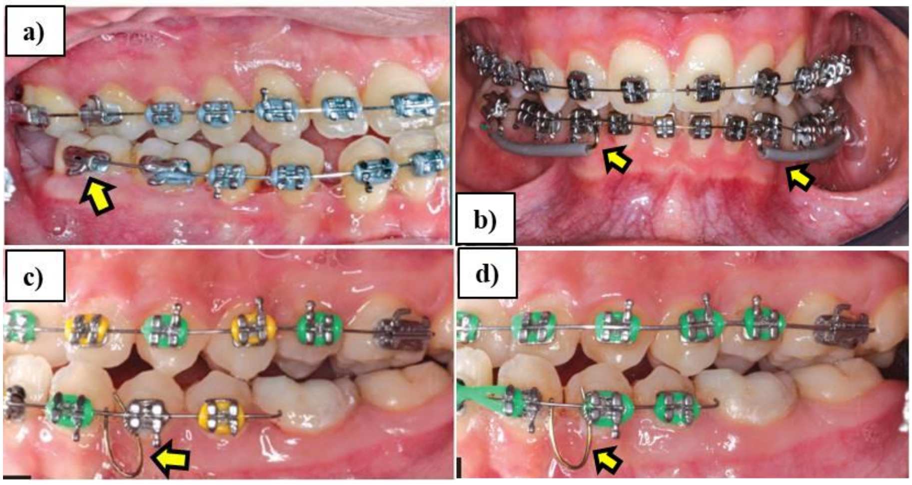

Fig. 1.11: Electric resistance spot welded NiTi orthodontic wires [25]

1.8 Motivation of the study

In fusion welding, due to melting and rapid cooling, dendrite columnar microstructure is formed along with brittle intermetallics [26]. These undesirable microstructural and compositional changes may degrade the properties of the weld. To address the mentioned challenges (section 1.6), few researchers have explored the possibility of utilizing solid state welding techniques to weld NiTi alloy. Due to the avoidance of molten state, the inclusion of brittle intermetallic compounds deteriorating the weld quality can be prevented. However, solid state welding processes such as explosive welding, ultrasonic welding and diffusion bonding are more suitable for lap joints. This restriction in joint design may limit the freedom of design in the fabrication of complex structures. Most of the literature on welding of NiTi alloy focuses on the parametric investigations of the welding process and its influence on metallurgical and mechanical properties. However, the thermo-mechanical actuation behaviour of the welded structure has not been reported elsewhere. Further, welding significantly affects the corrosion resistance of a material due to the changes in microstructure, distribution of inclusions, residual stress etc. Therefore, it is extremely important to evaluate the corrosion behaviour of the welded NiTi to ensure stability and longevity of the structure. Despite the fact, the corrosion characteristics of the solid state welded NiTi was not explored yet. So, there exists an indispensable requirement for a solid state welding process fulfilling the crucial welding requirements of NiTi alloy.

In this research work, an attempt has been made for the first time to weld NiTi alloy using friction stir welding (FSW). Both experimental and numerical investigations have been carried out to systematically understand the influence of process parameters on the weld properties. Most importantly, substantial efforts have been taken to evaluate the suitability of the welded NiTi alloy in real time applications through understanding the smart functional capabilities and corrosion behaviour after welding. Usually different peening methods will be used as a post processing tool to improve the mechanical and fatigue properties of the welded structure. In this regard, the corrosion behaviour of the weld post processed with peening methods such as surface mechanical attrition treatment (SMAT) and laser shock peening (LSP) has been evaluated.

1.9 Objectives of the thesis

The thesis work aims to employ the versatile friction stir welding process to weld NiTi alloy by ensuring adequate mechanical strength along with the retention of shape memory effect in the weld. Friction stir welding uses the synergic combination of temperature and plastic deformation to weld the materials without melting. Due to the associated low temperature and non-usage of filler material during FSW process, the issue of compositional compatibility of the weld with the base metal can be achieved. The primary objectives of the thesis are (i) To select the FSW process parameters and investigations of the metallurgical, mechanical and corrosion characteristics, (ii) To evaluate the temperature distribution and the strain rate experienced during welding, (iii) Exploration of actuation behaviour using different actuation strategies to ensure the thermomechanical stability of the welded structure and (iv) To investigate the influence of different peening methods such as surface mechanical attrition treatment and laser shock peening on the corrosion behaviour of the weld. This work comprehensively provides enough insights into the welding process parameters along with studies supporting the application perspectives of the welded structure.

1.10 Outline of the thesis

Chapter 1: Introduction to shape memory alloys and necessity of welding for smart functional applications

Chapter 2: Overview on the welding of NiTi shape memory alloy and its characteristics

Chapter 3: Experimental investigations on friction stir welding of NiTi shape memory alloy

Chapter 4: Elucidation on temperature distribution and strain rate during friction stir welding of NiTi using finite element analysis

Chapter 5: Evaluation of smart functional capabilities and thermomechanical behaviour of the friction stir welded NiTi alloy

Chapter 6: Investigation on corrosion characteristics of friction stir welded NiTi SMA using electrochemical corrosion testing

Chapter 7: Influence of surface mechanical attrition treatment and laser shock peening on corrosion behaviour of friction stir welded NiTi alloy

Chapter 8: Conclusions and scope for future work

Chapter 2

Overview on the Welding of Nitinol Shape Memory Alloys and its Characteristics

2.1 Status on Fusion welding of NiTi SMA

2.1.1 Laser welding

Laser welding is the most employed welding process for joining NiTi alloys [27–33]. The high energy density beam favours low heat input, small interaction area and narrow fusion zone (FZ)/heat affected zone (HAZ). Selection of laser type affects the weld properties. CO_2, Nd:YAG and fibre lasers are used to weld NiTi alloys. However, Nd:YAG (wavelength-1064 nm) and fibre lasers (wavelength-1091 nm) are preferred due to their shorter wavelengths which enables better absorption and requires less energy for welding. Laser power and scanning speed are the important parameters affecting the quality of the weld. Fig. 2.1 shows the cross section morphology of laser welded NiTi alloy. With increase in laser power, the change in morphology was clearly evident. The weld was asymmetric and the geometry changes from T shape to X shape at higher power 1.9 kW. At higher power, the input energy will be very high to cause more melting and thereby full penetration will be achieved i.e. increase in depth and width of the weld seam leading to formation of X shape.

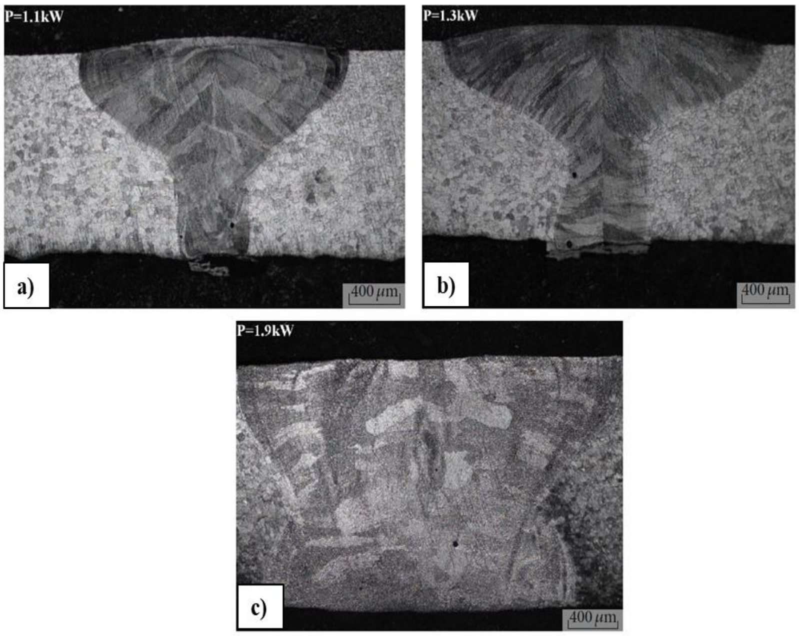

Fig. 2.1: Cross section morphology of Nd:YAG laser welded 2 mm thick NiTi alloy sheets at input power a) 1.1 kW, b) 1.3 kW and c) 1.9 kW [34]

B. Tam et al. have welded 0.4 mm diameter pseudoelastic wires using laser welding [35]. They have placed the wires one over the other in crossed configuration and the beam was focused in the intercept of the crossed wires. Fig. 2.2 shows the top and bottom side of the welded wires. Lower powers below 0.7 kW has yielded poor weld strength. To attain full penetration, minimum 0.8 kW was required and welds made in the range 0.85 kW to 1.7 kW have shown good weld strength.

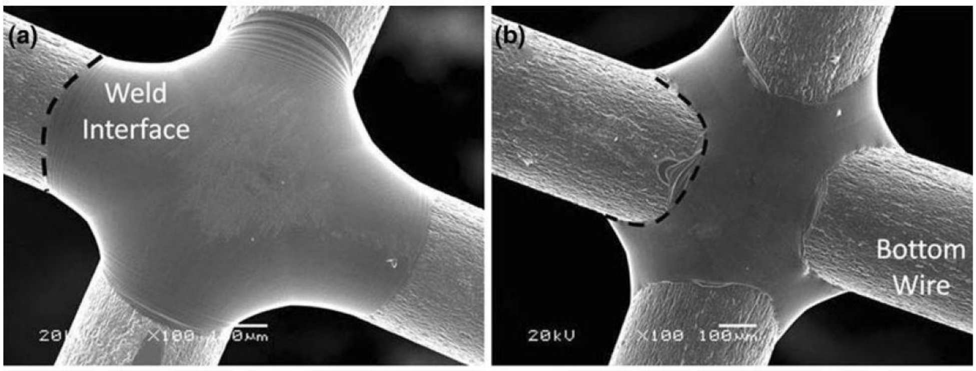

Fig. 2.2: Laser welding of NiTi wires at 0.8 kW a) Top side and b) Bottom side of the weld [35]

The solidification microstructure of the laser welded NiTi alloy is shown in Fig.2.3. The solidification of the weld region happens immediately through nucleation of partially melted grains of the base metal. The fusion zone experiences a transition from planar to cellular and cellular to dendrite structure near the centreline due to the increase in cooling rate [36]. The interface zone will be greatly affected by the base metal and the welding conditions.

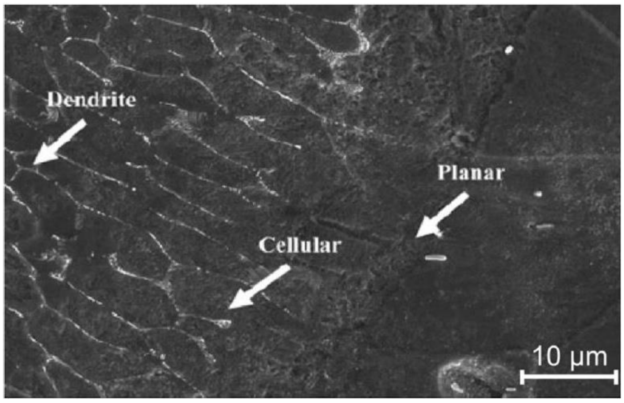

Fig. 2.3: Morphology transition due to laser welding [36]

Recently, Mehrshad et al. has used diode laser (wavelength 940 nm ± 10 nm) to weld NiTi alloy sheets of 0.5 mm thickness [37]. Fig. 2.4 shows the appearance of the weld. The weld produced at laser powers 350 W and 450 W was found to be uniform and homogenous. At 300 W, the heat input was lesser to enable proper fluidity of alloy in order to attain proper welding. At higher power 500 W, the excessive interaction of laser leads to over melting and partial evaporation of the alloy.

Fig. 2.4: Appearance of diode laser welded NiTi alloy [37]

The disadvantages of the laser welding process are high equipment-running cost and volatilization of Ni changing the functional properties of the weld. Precipitation is an important problem which affects the local composition of the matrix leading to Ti or Ni depletion region based on the formation of Ti or Ni rich precipitates.

2.1.2 Electron beam welding

Laser welding has a problem of lower depth to width ratio and some researchers have reported poor mechanical properties and shape memory behaviour due to the inclusion of O, H and N elements during laser welding. The electron beam welding favours higher depth to width ratio up to 25:1. In keyhole welding mode, the electron beam welding process can weld plates of thickness ranging from 0.025 mm to 300 mm [38]. D. Yang et al. has employed the vacuum electron beam welding to weld NiTi alloys [39]. They have welded 4 mm NiTi sheets using parameters viz. acceleration voltage-60 KV, beam current-24 mA, focussing current-2325 mA and welding speed-1000 mm/min. The welding has achieved defect free welds (free from voids, cracks and O, H and N elements) with good mechanical properties. Fig. 2.5 shows the XRD curve before and after welding. Initially, the base metal has B2 austenite phase only but after welding, B19' was also present. These changes along with the loss of alloying element Ni have affected the phase transformation behaviour of the weld as shown in Fig. 2.6. The difference between the phase transformation behaviour of base metal and centre region of the weld was clearly visible. The phase transformation temperatures after welding were higher than the base metal and especially the A_f has increased up to 30ºC after welding. The difference in phase transformation behaviour between the base metal and the weld is not desirable for practical applications. Moreover, the vacuum Ebeam process is expensive among all the welding processes employed for welding NiTi alloys.

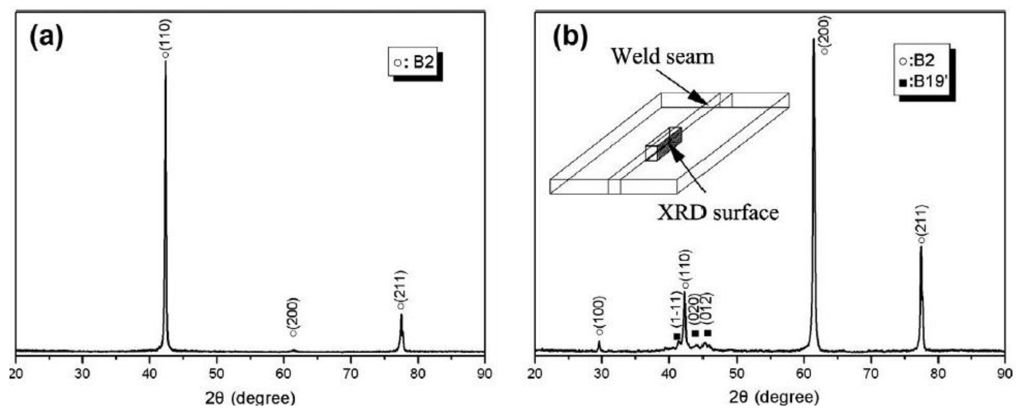

Fig. 2.5: XRD patterns of a) Base metal and b) Ebeam welded NiTi alloy [39]

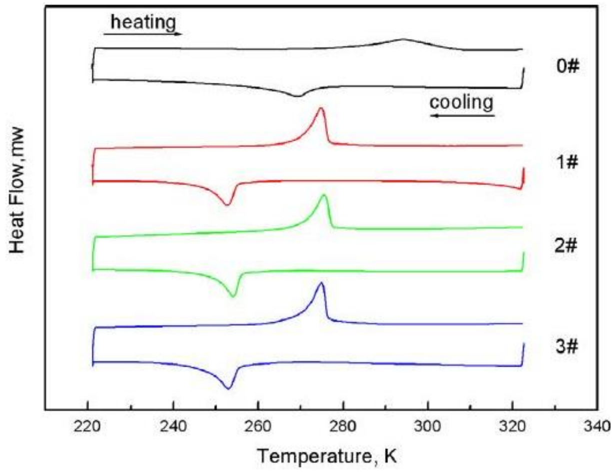

Fig. 2.6: Phase transformation behaviour of Ebeam welded NiTi alloy where 0# is the weld, 1# and 2# are regions next to the weld and 3# is the base metal [39]

2.1.3 Arc welding

Arc based welding processes are cheaper than other fusion or solid based welding processes. Gas tungsten arc welding is the widely used arc based process for welding NiTi alloy. Ikai et al. explored the possibility to weld NiTi in the form of wires and sheets as well [40]. They have reported approximately 50 % joint efficiency for the GTAW based NiTi weld joints. Recently, Oliveira et al. has welded 1.5 mm thick NiTi sheets using GTAW process [41]. The weld has shown good ultimate tensile strength of 700 MPa along with the elongation up to 20 %. Eijk et al. has tried plasma arc welding of NiTi alloy [42]. Fig. 2.7 shows the tensile properties of the plasma welded NiTi alloy. The joint strength was very poor due to the formation of undesirable brittle phases in the weld.

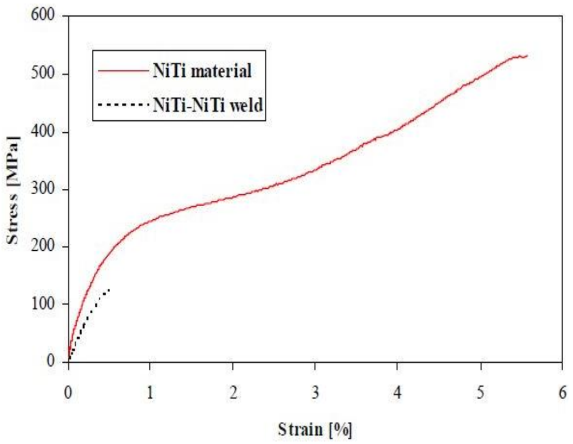

Fig. 2.7: Stress-strain curves of plasma arc welded NiTi alloy showing poor mechanical properties [42]

2.1.4 Resistance welding

Resistance welding has been used to weld wires or tubes of NiTi alloy [43,44]. Billy Tam et al. have done a detailed investigation for welding two 0.4 mm diameter NiTi wires at right angles to each other [45]. The welding time was kept constant at 10 ms and the current range of 120 A to 295 A was used for welding. The maximum joint breaking force of 18 N was attained for the sample welded at 195 A. Lower currents between 115 A and 145 A has yielded poor bonding strength. The fracture modes were interfacial, partial-interfacial and HAZ failure for lower currents, intermittent currents and higher currents respectively. Fig. 2.8 shows the SEM micrograph of the partial failure of the resistance welded NiTi wires at 245 A. The tensile test was halted after the crack initiated in the notch tip and propagated in to the week HAZ zone.

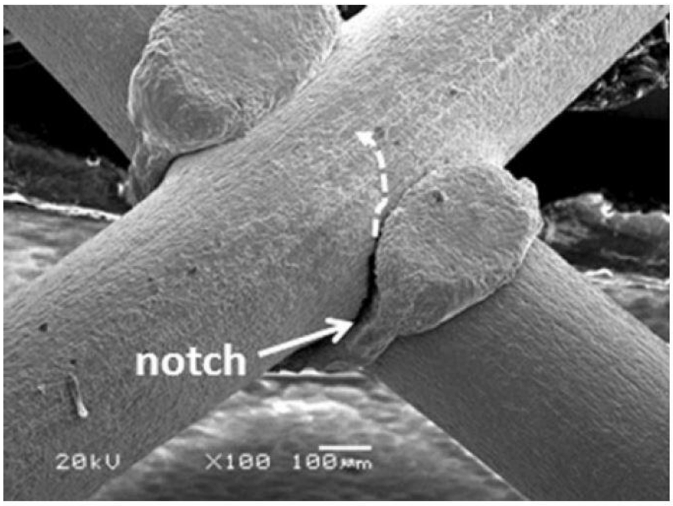

Fig. 2.8: Failure of the weld in HAZ region [42]

2.2 Status on Solid State Welding of NiTi SMA

Compared to fusion welding, the solid state welding of NiTi alloys were not extensively explored. Solid state welding processes does not require filler metal and hence the compositional compatibility of the weld with the base metal can be achieved. During solid state welding, a combination of pressure and temperature governs the welding of materials without melting. Due to the avoidance of solid-liquid-solid phase transformations, the inclusion of brittle intermetallic compounds deteriorating the weld quality can be prevented. Furthermore, the weld produced by solid state techniques possesses better dimensional accuracy with less distortion and residual stresses than fusion welding.

2.2.1 Friction stir welding process

Friction stir welding was invented in the year 1991 by The Welding Institute (TWI) of UK. It is a green technology with better energy efficiency and environment friendliness (no usage of cover gases or flux). FSW falls under the category of solid state welding processes where a synergic combination of pressure and temperature is used to weld the materials together (Fig. 2.9). Welding without melting of the workpiece material is highly significant due to the prevention of solidification related porosities, cracks etc. The FSW process does not require filler material and thus ensures the compositional compatibility between the weld and the base metal by preventing the formation of undesirable phases in the weld microstructure. Due to the avoidance of molten state, the process offers advantages such as no loss of alloying elements, better dimensional accuracy with less distortion and residual stresses than fusion welding processes [46].

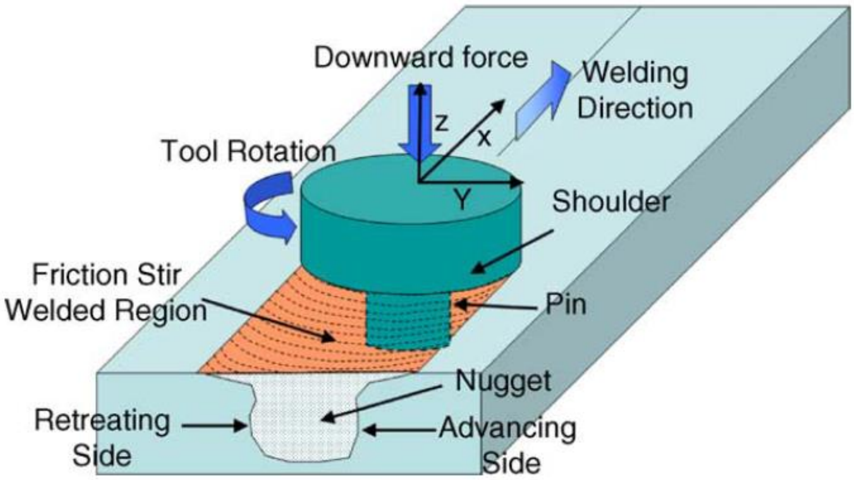

Fig. 2.9: Schematic of the friction stir welding process [47]

FSW uses a non-consumable tool having a profiled pin and cylindrical shoulder to facilitate the welding of the materials. The tool pin penetrates in to the material whereas the shoulder slides over the surface. The shoulder serves the purpose of “lid of the pot” as it prevents the escape of the softened material away from the welding zone and forces the material downwards to form a joint. The rotation of the tool generates higher temperature due to frictional heat whereas the traversing movement consolidate the material and aids in welding the plates together. The tool material along with the desired geometry has to be selected appropriately based on the material to be welded, material dimensions and the joint configuration [48]. The solid state welding process like ultrasonic welding, diffusion bonding etc. are more suitable for lap joints. However, the FSW process can fabricate structures with many joint configurations viz. square butt, edge butt, T butt joint, lap joint, multiple lap joint, T lap joint and fillet joint. The tools with threaded pins are required to weld plates of higher thicknesses. Using specially designed tools named Whorl™ developed by TWI, a 75 mm thick 6082Al-T6 plate was welded from both top and bottom sides (38 mm penetration from each side) [47].

The FSW technology is widespread especially in the transport industries such as automotive, aerospace, shipbuilding, rail etc. Some of the interesting examples are large tanks for satellite launch vehicles, light weight airframe structures, light alloy wheels, ship and oil rig panels for decks and bulk heads etc. Generally, it is used to weld high strength aerospace aluminium alloys which are difficult to weld using conventional welding processes. Other materials such as copper alloys, titanium alloys, steels, magnesium alloys have been welded using FSW [49–52].

In 2006, Blair D. London et al. has published a patent proposing the utilization of friction stir welding and friction stir processing (FSP) for NiTi alloys [53]. They have proposed this technology as the alternative to fusion welding process especially for the manufacture of biomedical components. FSP is a related technology which is used for surface modification of materials where as FSW is used for joining the materials. Blair D. London et al. and A. Barcellona et al. have investigated the influence of FSP on the microstructure and mechanical properties of the NiTi alloy [54,55]. There is no literature on FSW of NiTi alloys.

The characteristics of the FSW process is meeting the requirements of welding of NiTi alloy. FSW process produces autogenous weld and the issue of compositional compatibility of filler material with base metal can be ignored. Due to the lower welding temperature, the formation of intermetallics will be minimal. Due to solid state conditions, the distortion and residual stresses will also be minimal compared to fusion welding processes.

2.2.2 Friction welding

The friction welding process is a similar process as that of FSW which also utilizes frictional heat for welding. In case of friction welding, the relative motion between faces of the welding parts will enable welding of the parts together. However, the FSW utilizes the frictional heat energy caused due to relative motion between the non-consumable tool and plates for welding.

T. Shinoda et al. has used rotary friction welding to weld 6 mm diameter NiTi bars together. They have used a constant friction speed of 2910 rpm and studied the effect of different upsetting pressure on the microstructure and mechanical properties of the weld [56,57]. Fig. 2.10 shows the weld formed at different upsetting pressure. Due to the upsetting pressure, the oxide and work hardened layer in the face pierced out as a flash. The amount of flash increased with the increase of upsetting pressure. The mechanical strength of the weld was very good due to the heavy hot working during friction welding.

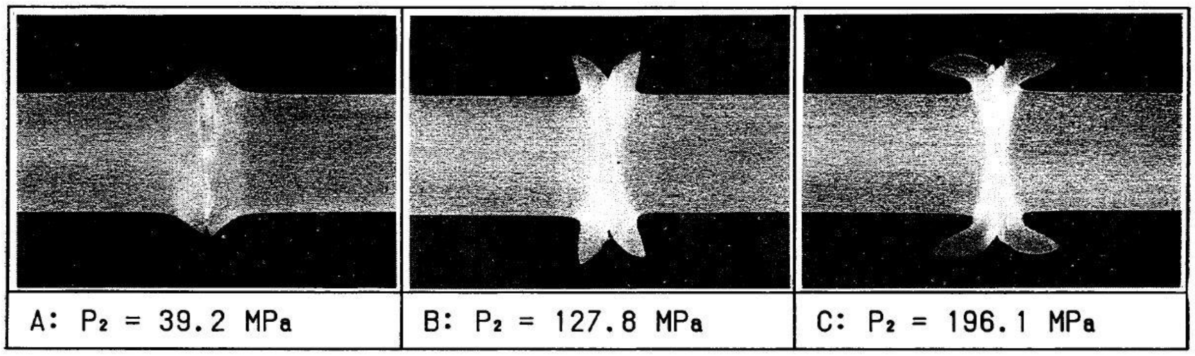

Fig. 2.10: Macrograph of the rotary friction welded NiTi bars [57]

2.2.3 Ultrasonic welding

W. Zhang et al. has welded 100 µm thick NiTi sheets using ultrasonic welding with the energies varying from 500 J to 2000 J [58]. The tensile shear test has revealed the lower failure load for welded samples due to the partially bonded weld interface. The weld at 2000 J has shown a maximum failure load of 557 N which is approximately 50% of the base metal. Fig. 2.10 shows the ultrasonic welded NiTi alloy. In addition, they have welded 150 µm thick sheets along with a copper interlayer of 20 µm between them [59]. The use of copper interlayer has improved the mechanical strength and a maximum failure load of 520 N was achieved (approximately 64 % of the base metal).

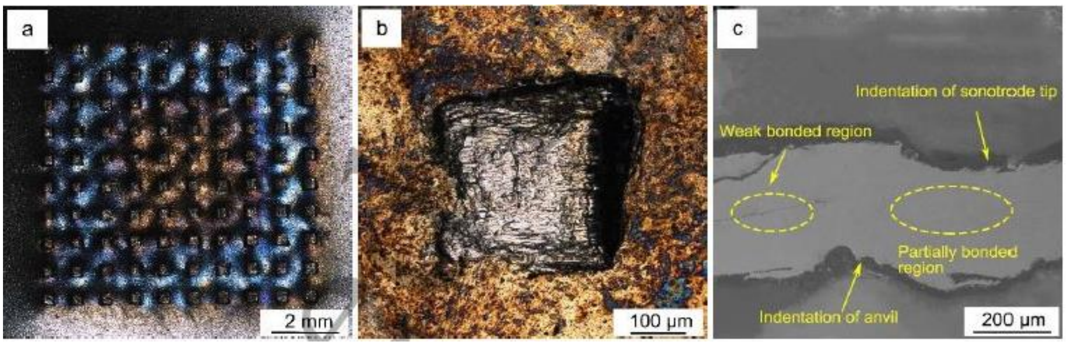

Fig. 2.11: a) Morphology of the weld produced at 500 J, b) Magnification of a spot in the weld and c) Cross section of the weld [58]

2.2.4 Explosive welding

Explosive welding of NiTi alloys was employed for joining thin sheets and their phase transformation and damping capabilities were reported [60–65]. Interestingly, S. Belyaev et al. have welded the NiTi plates viz. $Ti_{50}Ni_{50}$ plate (shape memory alloy layer) and $Ti_{49.3}Ni_{50.7}$ plate (pseudoelastic layer) together using explosive welding to maximize the recoverable strain of the bimetal composite for thermal actuator applications [66]. Fig. 2.12 shows the cross section of the bimetal composite produced by explosive welding. In the interface, the wavy shaped joint was clearly visible. Few melting zones (1-3) have been noticed in the weld region. The recoverable strain of the composite was affected by the residual strain and heat treatment after welding. A maximum strain recovery of 0.9 % was attained for the composite annealed at 450ºC for 2 hours.

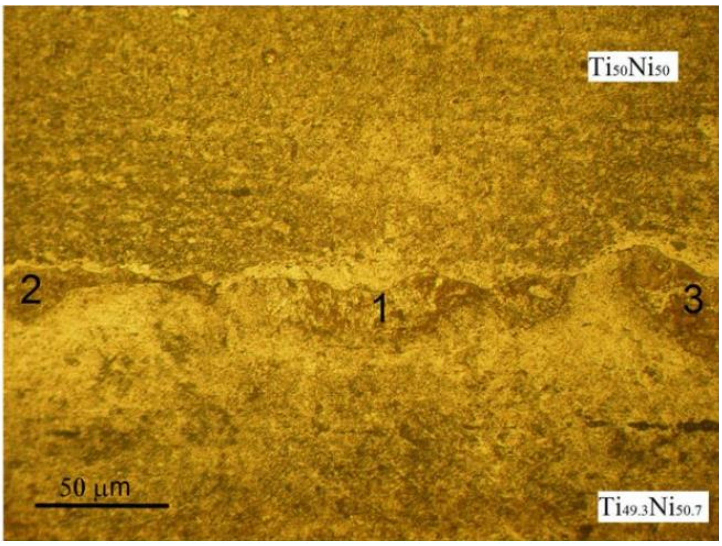

Fig. 2.12: Cross section of the bimetal composite welded by explosive welding [66]

2.2.5 Diffusion bonding

Senkevich et al. have investigated the diffusion bonding of NiTi and concluded that the higher temperature for a long duration is required to create high quality joints. For diffusion welding of 2 mm thick NiTi sheets having a bonding area of 50 mm^2, the high temperature of 1100ºC, pressure of 20 MPa and bonding time of 1 hour was required [67,68]. Haluk Kejanli et al. have tried to weld NiTiCu powder metallurgy manufactured compacts with Cu interlayer [69]. The optical micrograph of the bonded samples at 850ºC and 970ºC for 60 minute duration is given in Fig. 2.13a-b respectively. The sample produced at 850ºC has improper bonding with voids. The sample bonded at 970ºC had proper diffusion free from voids due to the availability of sufficient liquid phase in the interface. Due to better diffusion, the weld at 970 ºC has yielded the highest shear strength of 193 MPa.

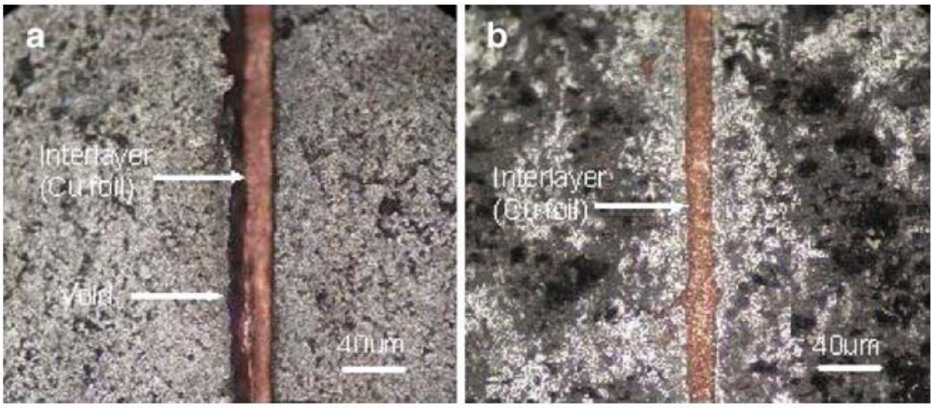

Fig. 2.13: Diffusion bonded NiTiCu components with Cu interlayer [69]

2.3 NiTi phase diagram and the influence of compositional change in the transformation temperatures

One of the key requirements in welding of NiTi alloy is the preservation or retainment of shape memory effect in the weld. The weld joint should not contain any undesirable brittle intermetallic phases (Ti_3Ni_4, Ti_2Ni_3, Ti_2Ni) or O, H and N elements. Due to these inclusions, the composition of the region alters drastically and also there exists a possibility for the weld to turn brittle. In such cases, the physical actuation cannot be attained across the welded structure. Fig. 2.14 shows the phase diagram of NiTi alloy. The boundary of TiNi is almost vertical along the Ti rich side whereas it decreases with decreasing temperature and the solubility drops to negligible at 500ºC. The diffusion controlled transformations and the formation of phases such as Ti_3Ni_4, Ti_2Ni_3 and $TiNi_3$ defines the solubility limit. The percentage of alloy elements, the temperature and the time led to diffusional transformations. The following is the order of diffusional transformations with respect to increase in temperature.

$$Ti_3Ni_4 \longrightarrow Ti_2Ni_3 \longrightarrow TiNi_3$$

The TiNi phase holds a B2 (CsCl) structure (austenite, the high temperature phase) at room temperature which can exist only in a specific compositional range. B2 will transform to BCC at 1090ºC which can be retained through quenching or furnace cooling to room temperature. Martensite is the low temperature phase with monoclinic structure represented as B19'. The metastable phase diagram between TiNi and Ti_3Ni_4 is depicted as an inset in Fig.2.13. This diagram will be helpful for tuning the phase transformation temperatures and defining the heat treatments for the betterment of the shape memory characteristics.

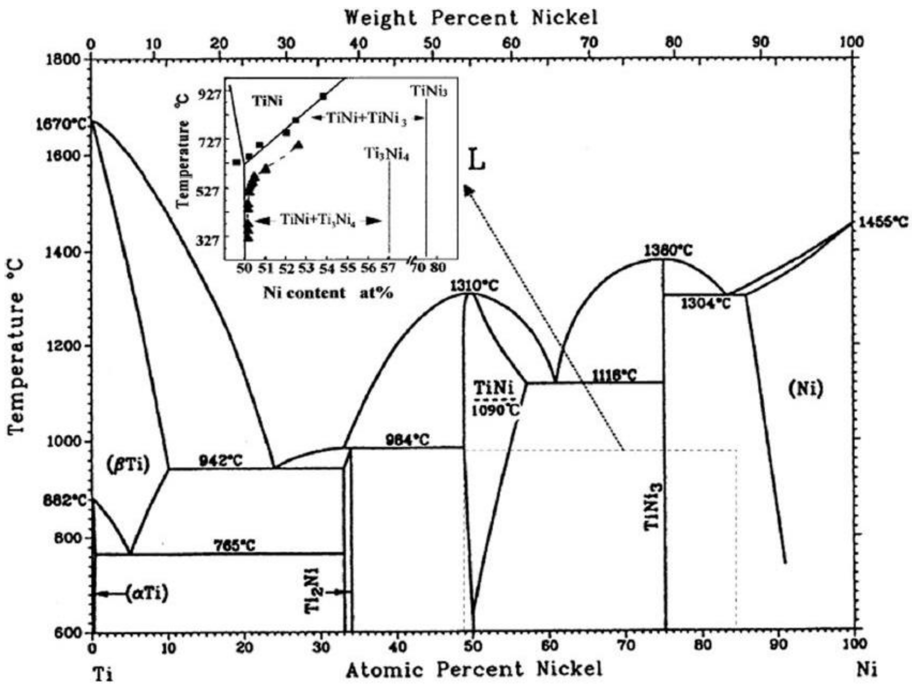

Fig. 2.14: Phase diagram of NiTi alloy [70]

The phase transformation of the NiTi alloy is highly sensitive to compositional change. J. Frenzel et al. has done a detailed study on the influence of Ni composition on the martensitic transformation of NiTi alloy [71,72]. Fig. 2.15 shows the influence of Ni composition on the martensite start temperature. At Ni composition of 50.0 at. %, the M_s was recorded to be 333 K. There existed a decreasing trend in transformation temperature with increase in Ni composition.

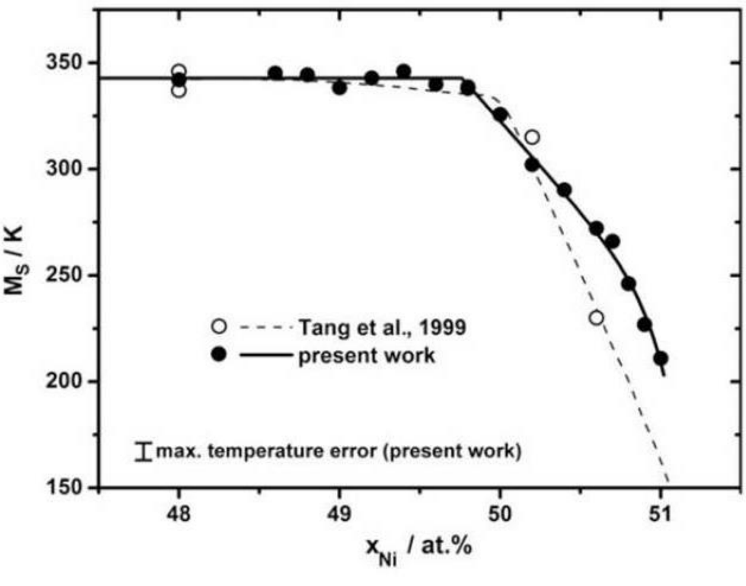

Fig. 2.15: Influence of Ni composition on martensite start temperature [72]

2.4 Functional capabilities of welded NiTi SMA

The evaluation of function properties is essential to ensure the suitability of the welded structure for applications requiring physical actuation or pseudoelasticity. Few researchers have studied the tensile loading/unloading behaviour of laser welded NiTi alloy [30,33,73]. Notably, Oliveira et al. has studied the tensile cycling of NiTi alloy welded using GTAW process [74]. They have performed the tensile cycling at 4, 8 and 12 % of strains and tested up to 600 cycles. Fig. 2.16 shows the tensile cycling of GTAW samples up to 12 % of strain. Usually the grain size and other changes induced by welding will influence the cyclic behaviour. The onset of stress plateau decreases with the increase in number of cycles due to the development of dislocations or formation of martensite during loading/unloading cycles. Hence, the increase in number of cycles lowers the overall stress and increases the irrecoverable strain. Due to this, a reduction in mechanical hysteresis occurs with increase in cycles.

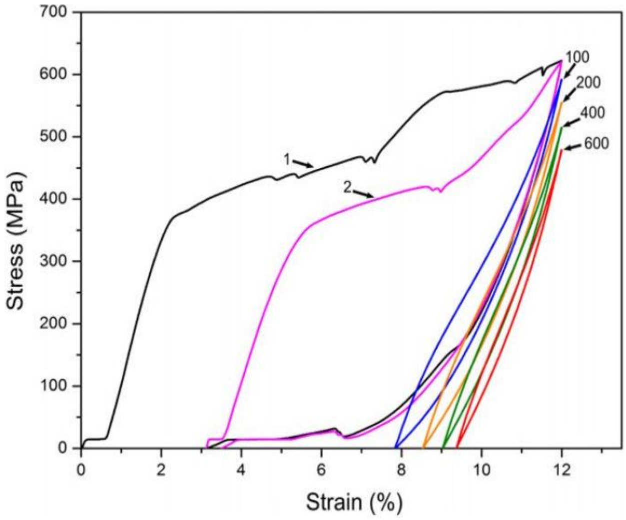

Fig. 2.16: Tensile cycling curves of GTAW welded NiTi alloy [74]

Except Oliveira et al., no one have studied the shape memory effect of the welded structure using bending-recovery method [75]. Fig. 2.17 shows the bending device and steps in bending-recovery analysis of the laser welded samples. They have bent the welded samples (weld being in the centre of the sample) to 180º using the custom made bending device. The bending was done after dipping the sample inside the liquid nitrogen to ensure that the sample remains in martensite state during bending. Then, the sample was released to recover freely at room temperature. All the samples have recovered to the initial straight position.

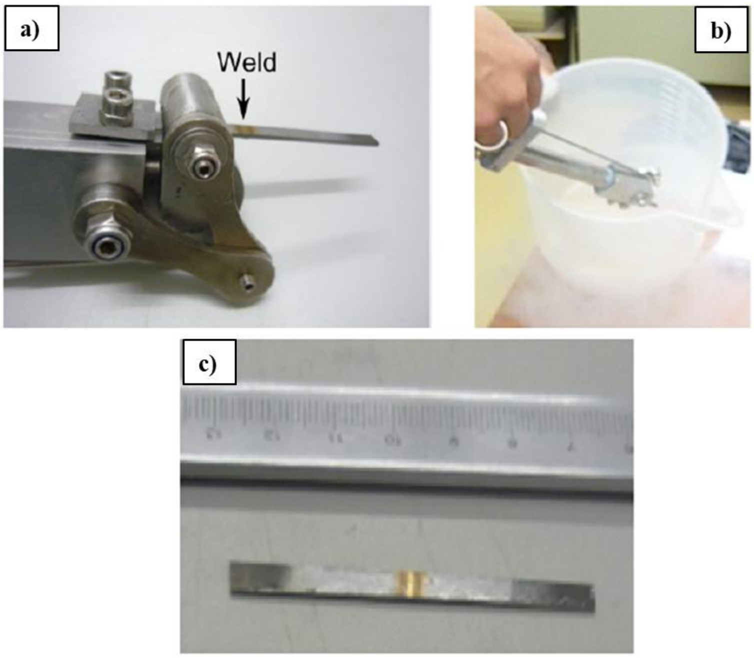

Fig. 2.17: Bending-recovery method to evaluate SME a) Before bending, b) Bending by dipping inside the liquid nitrogen, c) Recovered shape at room temperature [75]

Shape memory alloys are being used as dampers for civil structures and machine tools. So, few literatures have reported the damping properties of explosively welded NiTi shape memory alloys [62,65]. They have evaluated the damping capabilities at different forced oscillation frequencies. Moreover, the effect of aging temperature and time on the damping behaviour has been reported.

2.5 Numerical simulation for temperature generation and strain rate during FSW

The FSW process parameters and the material properties affect the temperature profiles, strain rate and cooling rate of the sample. The temperature profile and strain rate significantly influence the microstructure and properties of the weld. Experimentally, thermal cycles can be measured using thermocouples or sometimes using in-situ neutron diffraction where the lattice distortion will be correlated to temperature change. Usually, material flow behaviour and the strain rate will be found using tracers or markers of different materials. After welding, based on the initial and final position of the tracer, the flow velocity and the strain rates can be estimated [76,77]. Recently, Rahul Kumar et al. have used a better method called particle image velocimetry to find the strain rate and flow velocity of the material flow during FSW [78]. In case of experimental data unavailability, a computational model will be used to evaluate the temperature profiles and strain rates. Many literatures are available on the numerical simulation of temperature and strain rates during FSW [79–84]. Finite element analysis (FEA) packages such as Comsol Multiphysics, Ansys, Abaqus and Weldsim have been used widely for the simulation. Modelling of the FSW process was based on methods viz. analytical thermal models, FEA based solid thermal models, thermo-mechanical models, computational fluid dynamic models (CFD) etc. Based on the method used, the accuracy and the computational time required for solving the model differ. M.Z.H Khandkar et al. have made an important contribution by introducing a torque based model as an alternative to frictional heating based models [85]. Here, the input torque measured during FSW has been correlated with the heat produced at the workpiece-tool interfaces. But the major limitation of this model is the requirement to fit thermal contact conductance in the bottom surfaces. These values have to be found experimentally to make the model more reliable. Though the results are in good agreement with the experimental values, this torque based model requires very large computational time.

2.6 Preliminary investigations on laser actuation of NiTi SMA

There is no detailed literature available for laser actuation of shape memory alloys. In order to understand the laser actuation of SMA element, initially experiments has been performed with SMA springs [86]. Few literatures are available for laser actuation of SMA, where they have used the constant exposure of laser irradiation in a particular spot or irradiating the entire SMA surface with suitable lens arrangement [87–91]. The method of irradiating the entire surface can be used only when the surface area of the SMA components is small (few millimetres to tens of millimetres). This method of constant irradiation suffers a major disadvantage, because the prolonged exposure to laser beam may result in localized failure or damage due to laser-induced melting or ablation. In order to avoid these problems, we have proposed the method of scanning the required area using a laser beam i.e. the laser beam of particular spot size can be scanned throughout the length of the SMA component to attain required actuation. Fig. 2.18 shows the different types of actuation methodologies available for SMA. Continuous laser from the fibre laser source doped with Yb active gain medium of 1064 nm wavelength was used for irradiating the SMA spring. To move the laser beam along the length of the spring, a dynamic reflecting mirrors or simply galvo mirrors are used. Laser guided through the optical fiber cable is made to fall on the galvo mirrors. These mirrors reflect the line beam of width 0.2 mm over the spring surface at a scanning speed of 30 mm/s. The SMA spring in a closed coil configuration is fixed at one end and a deforming load is hung at the other end. The laser power in the range of 15 W to 50 W was used for the investigation of the thermo-mechanical behavior of the SMA spring under varying bias loads (1.5N, 2.5N and 3.5N). The extension of the spring due to different bias loads will be different and the higher load extends the spring to a greater length. To cover the whole length of the spring, the laser scanning distance will be increased accordingly.

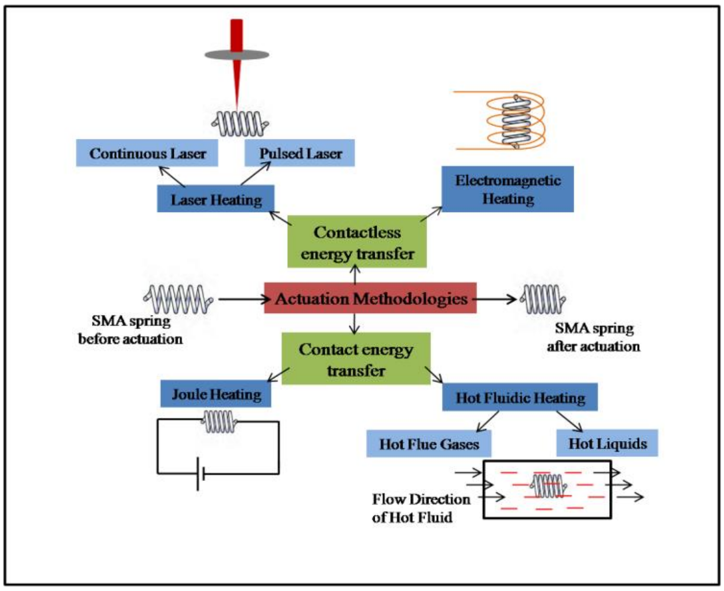

Fig. 2.18: Different actuation methodologies applicable for an SMA element

Once the deformation due to the load terminates, the laser is switched on. The irradiation from the laser causes a light-matter interaction, eventually due to energy absorption convert the light energy into heat. Fig. 2.19 shows the detailed schematic of the heat transfer across the SMA spring during laser irradiation. The laser irradiation of the spring via scanning technique enables heat distribution throughout the length of the spring. During scanning, the top surface of every coil of the SMA spring will be impinged with laser beam. This laser scanning from one end and returning to the same end after travelling throughout the spring is called a pass.

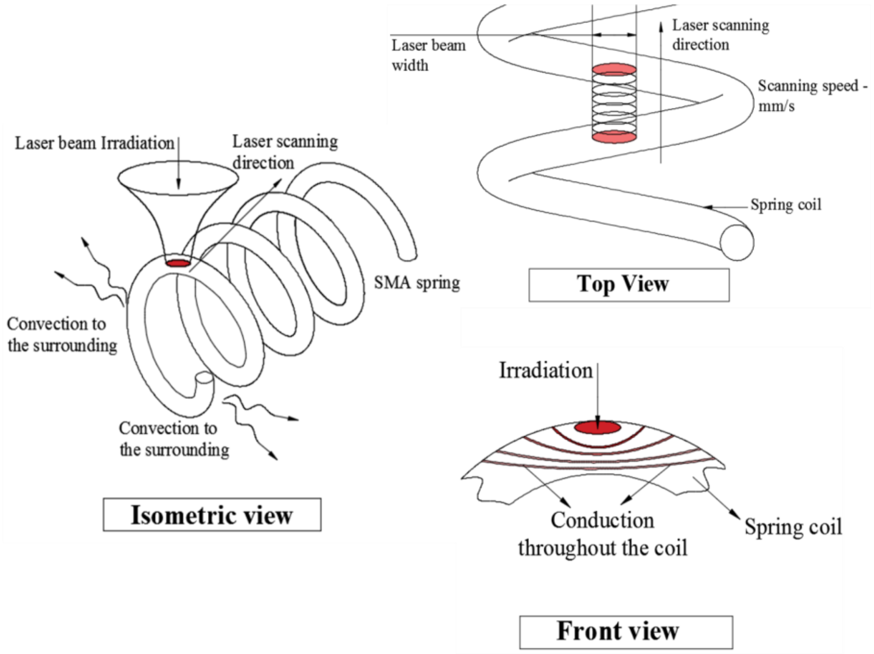

Fig. 2.19: Detailed schematic of the heat transfer in the SMA spring due to laser irradiation

The displacement vs. time curve for 15 W, number of passes required for actuation and maximum displacement at different laser power is given in Fig.2.20. It was observed that the increase in laser power decreases the number of passes and in turn the heating time required for the actuation. The actuation against the higher bias load has taken more number of passes due to the associated higher displacements. A maximum of 8 passes was required for complete actuation of the spring at 15 W against the bias load of 2.5 N and 3.5 N. However, the laser powers above 35 W required only one pass irrespective of the bias loads. The higher temperature reached at higher powers drives the spring to exert more pulling force and reduces the inter-coil gap. This reduction of inter-coil gap has reflected as an increase in displacement. This is clearly evident in 2.5 N load, where above 30 W, the displacement was saturated at 17.1 mm due to the nullification of the inter-coil gap. A minimum displacement of 10.1 mm was obtained for a bias load of 1.5 N at 20 W. However, for the bias load of 3.5 N throughout the increase in power, no saturation was observed and a maximum displacement of 28.9 mm was observed at 50 W. Based on these experiments, laser actuation of friction welded strips has been performed (Chapter 5).

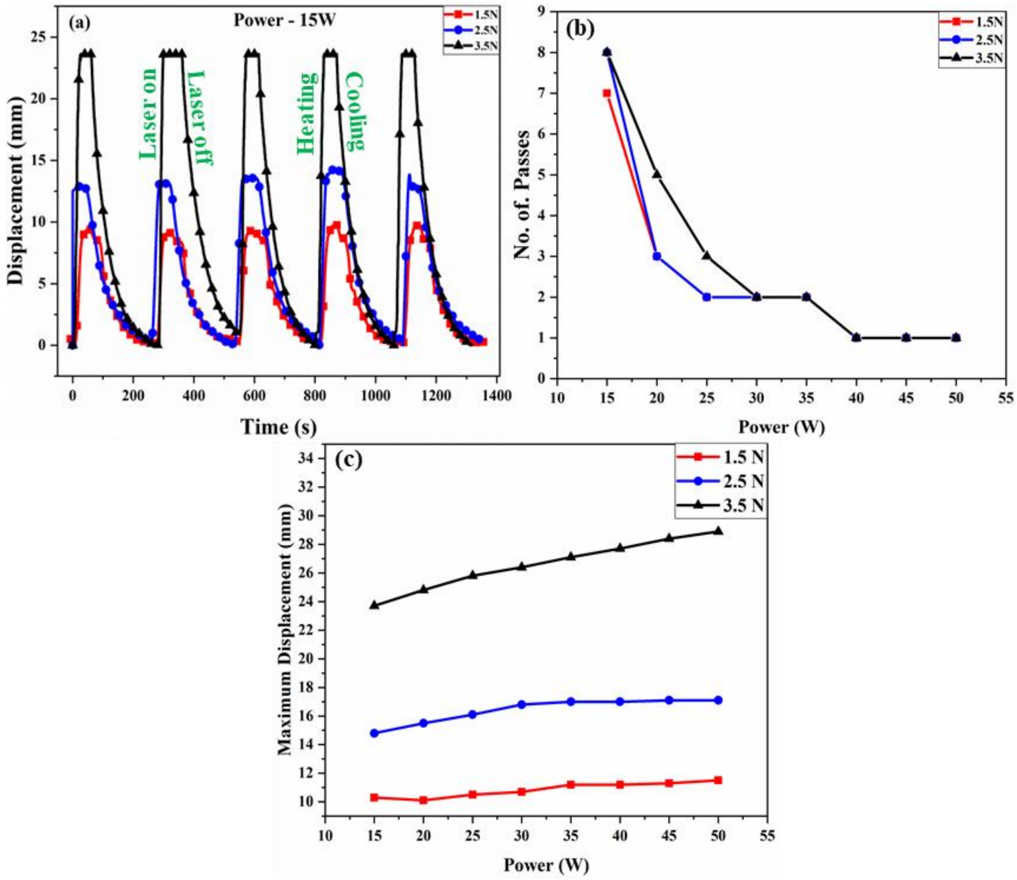

Fig. 2.20: Heating/cooling curves at laser power of 15 W, b) Number of passes required for actuation and c) Maximum displacement at different laser powers

2.7 Corrosion behaviour of welded NiTi SMA

Based on the fusion or solid state process, the material will experience high temperatures and pressure during welding. Every welding process will induce microstructural changes and residual stresses in to the weld. Moreover, the formation of precipitates would change the composition of the weld. The corrosion is a surface phenomenon which depends on the type of material, microstructure, presence of precipitates etc. In general, the corrosion resistance of the weld will be lower than the base material before welding. Corrosion behaviour of laser welded NiTi alloy has been explored using electrochemical method [92–96]. Peng Dong et al. have studied the corrosion behaviour of laser welded NiTi alloy where the 0.9 % NaCl solution and Hank’s solution was used as the electrolyte [97]. Fig. 2.20 shows the welded NiTi wires after corrosion testing. The HAZ was affected more compared to the FZ and the base metal in both solutions. The NiTi alloy was more susceptible to corrosion in NaCl solution than the Hank’s solution.

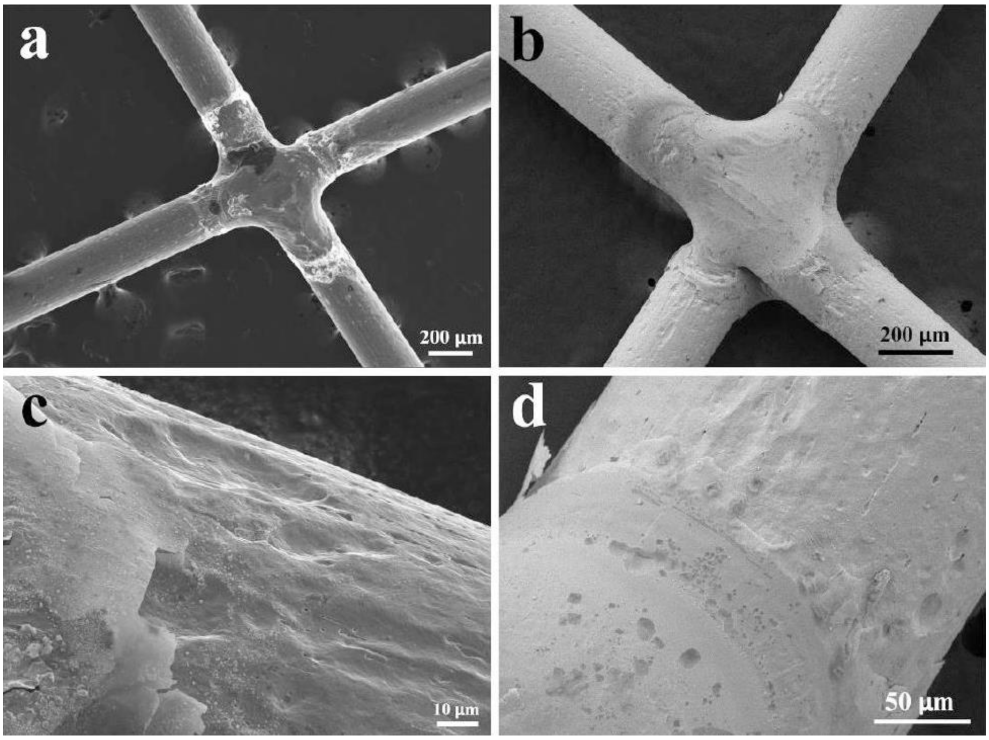

Fig. 2.21: SEM images showing the laser welded NiTi wires after corrosion testing a), c) in 0.9 % NaCl solution and b), d) Hank's solution

Susmita Datta et al. have studied the corrosion behaviour of laser welding NiTi alloy in simulated body fluid (SBF) [98]. They have reported that the weld made at 800 W power and 4000 mm/min welding speed has shown better corrosion resistance than the parent metal as signified by the lowest corrosion current and highest polarization resistance. The welding has increased the Ti/Ni ratio in the surface which in turn improved the stability of the corrosion resistant layer (TiO_2) and reduced the corrosion rate.

2.8 Post processing peening treatments on NiTi SMA

During FSW, the rotating tool plunges and traverses along the abutting edges of the plates. This heating cycle and the rigid clamping arrangement of the workpiece will lead to generation of residual stresses in the vicinity of the weld. These residual stresses will significantly degrade the structural integrity and fatigue properties of the weld. Peening methods such as surface mechanical attrition treatment and laser shock peening can be employed in the surface of the weld to mitigate the tensile residual stresses formed during welding. There are few literatures available on the LSP of NiTi shape memory alloy where they have used the nanosecond Nd:YAG laser having 1064 nm wavelength to peen the surface [99–101]. In 2019, Hao Wang et al. have reported the LSP of NiTi alloy using femtosecond laser having wavelength of 800 nm and pulse width of 35 fs [102]. T. Hu et al. has explored the influence of SMAT on the microstructure, phase transformation behaviour, wear resistance and corrosion behaviour of NiTi SMA [103–107]. However, no reports are available on the application of SMAT or LSP on the surface of the welded NiTi alloy.

2.9 Summary

The fusion welding of NiTi SMA has been reported widely compared to solid state welding processes. Most of the fusion welding processes suffer from the problems viz. inclusion of undesirable hard intermetallics, drastic change in phase transformation temperatures, brittle nature of the weld etc. Solid state welding of NiTi alloy was not well explored as of fusion welding. Especially, the smart functional capabilities and corrosion behaviour have not been explored for solid state welded NiTi alloy. Moreover, we have proposed a novel scanning method for laser actuation of SMA. From the literature, it was ascertained that peening has not been applied to the welds of NiTi alloy.

Chapter 3

Experimental Investigations on Friction Stir Welding of NiTi Shape Memory Alloy

3.1 Introduction

The friction stir welding has been employed to weld the NiTi shape memory alloy. In this chapter, the requirement of a FSW machine, selection of tool material, tool geometry and the process parameters are discussed. The NiTi alloy sheets are expensive and in order to minimise the trail experiments, knowledge base from literature and simulation have been utilized. As tool rotational speed is the major parameter, an attempt has been made to weld NiTi shape memory alloy at three different rotational speeds. The effect of tool rotational speeds on the microstructure, phases and mechanical properties of the NiTi alloy has been studied. The phase transformation behaviour with respect to the rotational speeds and in different weld regions has been explored. In addition, the influence of the FSW process on the composition of the NiTi alloy and details on tool failure has been discussed.

3.2 Details about the welding facility used for welding

The FSW machine used for welding was designed and developed by Bangalore Integrated System Solutions (BISS) in collaboration with Prof. Satish V. Kailas laboratory from Indian Institute of Science (IISc) Bangalore, India. The machine have 2370MS controllers delivering high speed closed loop control and enables the setup, tuning and calibration can be performed through the host computer. Fig. 3.1 shows the photograph of the machine. Unlike normal FSW machines, this custom built machine possesses multi-axial load frames with high stiffness and natural frequency. It has two translational axes (X and Y) and a mutually perpendicular spindle (Z axis). The X and Y axes enable the movement of welding table in XY plane whereas the Z axis controls the plunging/retraction of tool. Two electric motors enables the tilting of the spindle in both X and Y planes. The three axes movement is controlled by linear hydraulic actuators. A rotary hydraulic actuator capable of generating high steering torque powers the spindle. Overall, the FSW machine has higher vertical load capacity and thus it is suitable to weld thicker plates and higher melting point materials such as titanium alloys, steels, etc. The detailed specification of the machine can be found in the Table 3.1.

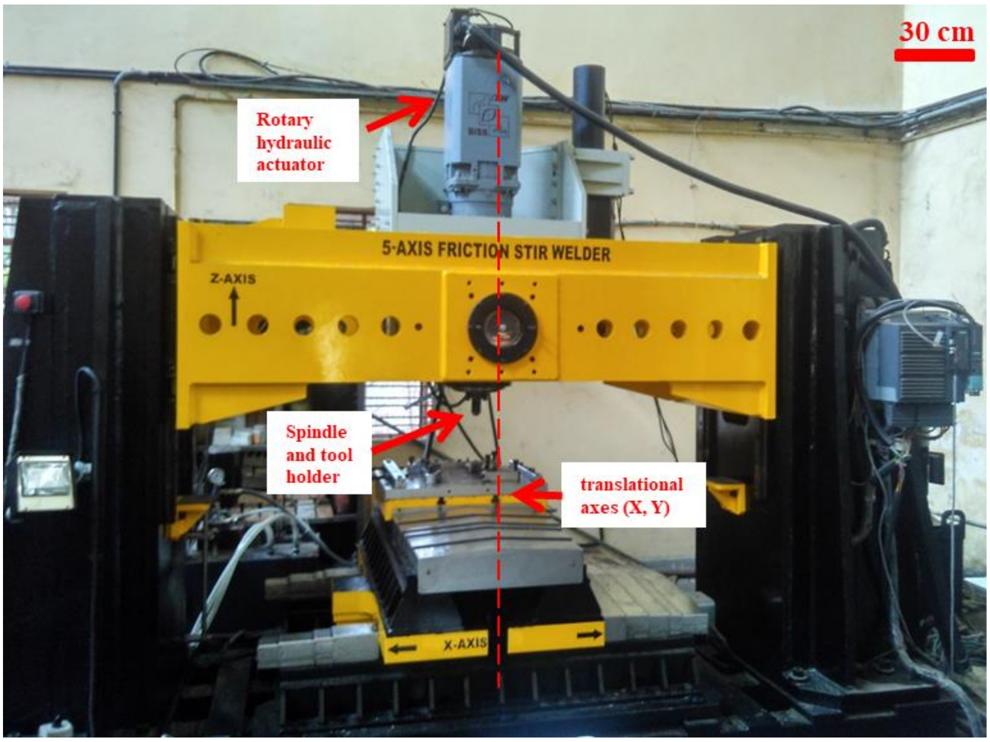

Fig. 3.1: Five axis FSW machine used for welding NiTi alloy (IISc Bangalore)

Table 3.1 Specifications of the FSW machine

S No	System	Specification
1	Specimen mounting area	500 mm × 500 mm
2	Axial load capacity	50 kN
3	Rotational speed	100 to 3000 RPM
4	Table speed	1 to 250 mm/min
5	Tool Tilt	-6 to +6 degrees in both X and y plane
6	Weldable plate thickness	0.5 mm to 65 mm
7	Position resolution	5 µm
8	Cooling system	Water cooled

3.3Experimental

3.3.1 Selection of tool material and geometry

Friction stir welding is a contact based process where the tool and work material will be interacting with each other during welding. So, the initial step is to select an appropriate tool material suitable for welding the particular material. The tool should have adequate hardness and yield strength at high temperatures to counter severe temperature (frictional heat) and stresses (material flow) caused by the tool rotation-traverse movement. The thermal conductivity and coefficient of thermal expansion of the tool material also plays a role in heat dissipation and thermal stress experienced by the tool. Overall, the tool material should possess characteristics such as high hardness, low reactivity to oxygen and high temperature strength.

Tungsten based tool materials possess desired properties to weld hard materials and proved to be effective in welding titanium alloys, steels etc. Densimet tool material (an alloy of tungsten) was selected for welding. The properties of the tool material Densimet D2M can be found in the Table 3.2.

Table. 3.2: Properties of the tool material Densimet D2M

Composition	Modulus of elasticity (GPa)	Hardness (HRC)	Thermal conductivity at 500^{o}C (W/m.K)	Yield strength at 20^{o}C (MPa)	Coefficient of thermal expansion (10^{-6} K^{-1})
W-90 % along with Mo, Ni and Fe	360	Maximum 31	65	700	5.3

Defining the tool geometry is very critical as it governs the rate of heat generation, traverse force, torque and plastic deformation during welding. Important factors are pin shape-size, shoulder diameter etc. During welding, the pin plunges in to the welding material and the shoulder slides over the surface. The pin size (height and diameter) and shape (tapered or cylindrical) affects the stirring-mixing of the work material and eventually the proper consolidation of the weld joint without defects. The shoulder-workpiece interface is the major heat generating component. Since, the sheet thickness (1.2 mm) is small; a cylindrical tool with non-threaded pin was selected. A pin height of 0.9 mm was also selected based on the thickness of the sheet. Since, the melting point of the work material is higher; a dwell time of 30 s was selected for welding. During start of the welding (dwelling stage), the tool rotates in the same position without traverse, thereby supplies adequate heat energy to plasticize the material and initiate the material flow around the pin. Fig. 3.2 shows the desired tool geometry for welding NiTi alloy sheets.

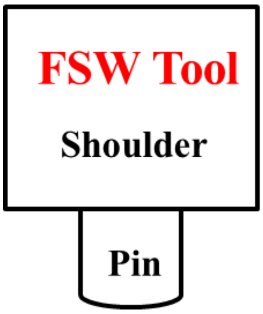

Fig. 3.2: Tool geometry for welding thin sheets of NiTi alloy using FSW process

3.3.2 Numerical simulation to predict the process parameters range

The NiTi sheet of 1.2 mm thickness with Ni 50.75 at.% (SE508-NDC) was used for welding. NiTi (SE508 grade) is a hard material (>250 HV) having a high melting point of 1310^{o}C. In FSW process, the tool rotational speed is the most influential parameter affecting the frictional temperature and plastic deformation [47,108]. There are many reports signifying the influence of the tool rotational speed on the welding properties. Recently, the influence of tool rotational speed on microstructure and mechanical properties has been reported for materials such as Al-Li alloy and steel [109,110]. As the tool rotation speed increases, the heat induced due to friction between the tool-workpiece interface and the plastic strain energy from intense deformation of workpiece increases. Hence, the tool rotating at higher speed will generate more heat and hence reach higher peak temperature during welding. In addition to the effect on peak temperature, the tool rotational speeds also have impact on strain and strain rate generated in the welding zone.

Welding temperature during FSW always lies in the range 55% to 85% of the melting point of the material to be welded [108,111]. Using the mentioned temperature range as the thumb rule, the FSW of NiTi alloy was simulated based on finite element analysis in Comsol Multiphysics. More details about the simulation can be found in the Chapter 4. From the simulation, the maximum temperature during FSW of NiTi alloy has been predicted. Fig. 3.3 shows the maximum temperature as a function of tool rotational speed. In the graph, three colour zones viz. yellow, green and red can be seen. The yellow zone (< 55% of the melting point) depicts the tool rotational speed generating the temperature below the FSW operating temperature range. The rotational speeds in this zone are not sufficient enough to plasticize the material to enable welding. The red zone shows the rotational speeds which could generate higher temperature above the FSW desired range (> 85% of the melting point). The tool rotational speeds in the red zone may lead to melting of the materials and catastrophic tool failure (the tool may plunge into the back plate in the fixture). The green zone in the middle reveals the suitable tool rotational speed range within which the FSW of NiTi would be possible. The tool rotational speed lying in the range 700 rpm to 1300 rpm has been found suitable as per the simulation. Based on the simulation and literature, the trail experiments were conducted to arrive at the suitable process parameter set for FSW of NiTi alloy.

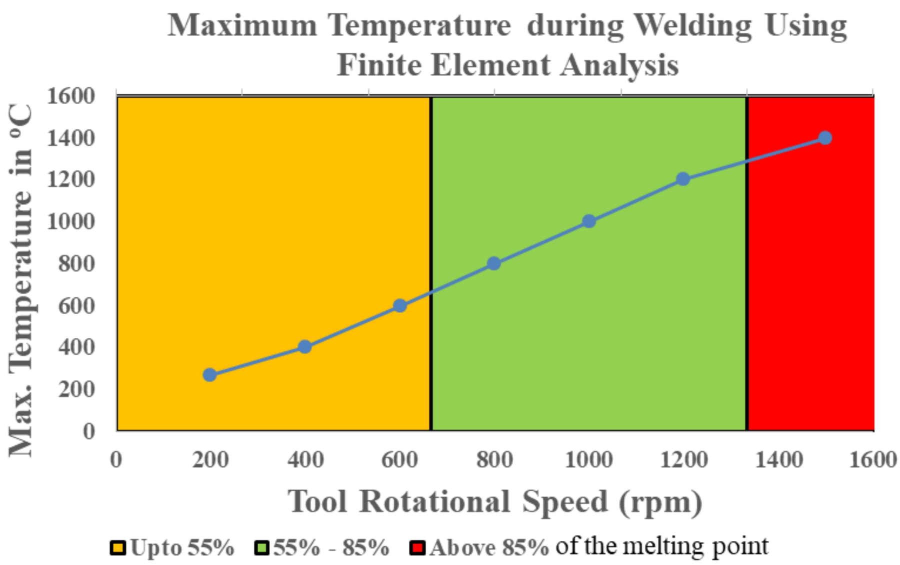

Fig. 3.3: Simulation based on FEA to predict the FSW process parameters

3.3.3 Trail experiments to select the process parameters

The sheets to be welded were cut using wire electro discharge machine (WEDM). Before welding, the surface of the sheets was mechanically cleaned with SiC abrasive papers to remove the surface irregularities, contamination and oxide layer. Then, the sheets having a dimension of 100 mm × 50 mm × 1.2 mm were abutted and fixed intact in a custom made fixture for holding thin sheets. The fixture had undercuts which would arrest all the degrees of freedom of the sheets and aids in proper welding. The welding was carried out in closed square butt configuration. The fixture used for holding the sheets and the closer view of the machine is shown in Fig.3.4 and 3.5 respectively.

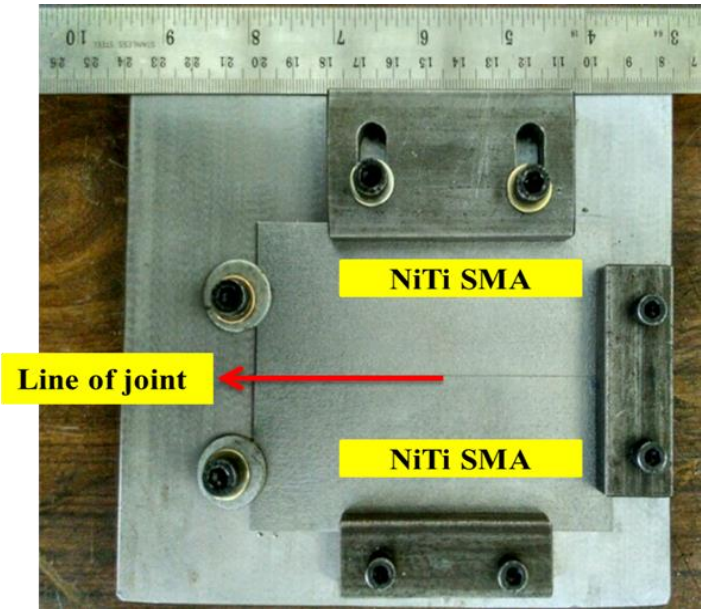

Fig. 3.4: Specially designed fixture with undercuts to hold the thin sheets during welding

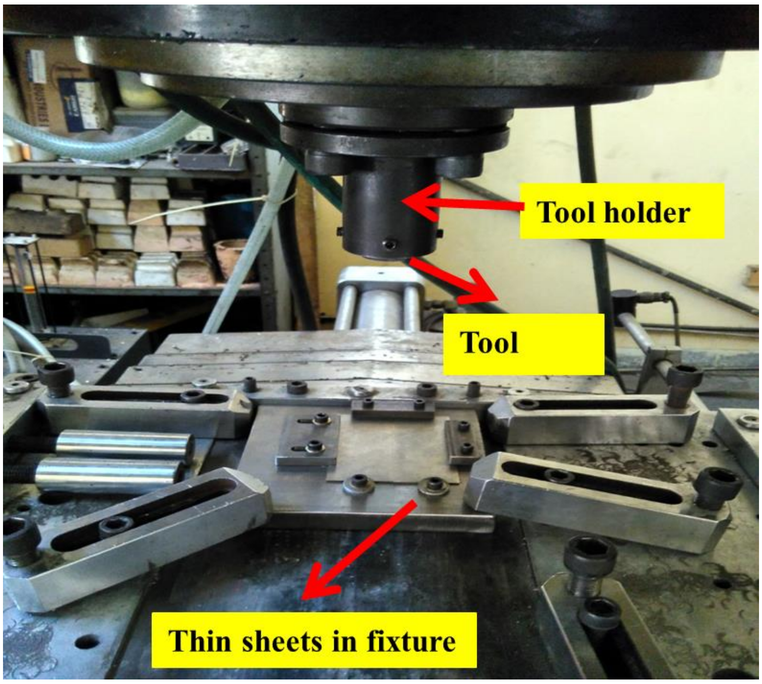

Fig. 3.5: Closer view of the machine and the sheets fastened in a fixture

Fig. 3.7 depicts the surface appearance of weld joints at different process conditions. The tool geometry and process parameters used for trail experiments are listed in Table 3.3. Initially, the condition A was tried. But the heat generated was insufficient to plasticize the material enough for joining and the tool pin was chipped off. In condition B, the tool dimensions were increased and traverse speed was reduced to 25 mm/min in order to generate sufficient heat for welding. During welding, the workpieces were severely distorted due to higher heat input and the edges did not consolidate to proper weld. It is to be noted that the weld produced at condition B and C had same shoulder diameter of 20 mm. However, the weld track produced at condition B (1500 rpm) had higher width than the weld track produced using condition C (1000 rpm). This is due to the fact that at 1500 rpm, the temperature was extremely high and the NiTi alloy was plasticized more and forged out of the shoulder zone. So, in condition C, the same tool was used with changes in tool rotation and traverse speed to lower the heat input. Though the distortion was reduced, the inadequate filling similar to previous weld was observed. The lack of filling (improper consolidation of the joint) is due to the larger pin diameter. Based on this, the tool pin diameter was reduced from 7 mm to 5 mm and used for the subsequent experiments (Section 3.3.4). From the trail experiments, it was concluded that the condition C with modified pin diameter may yield defect free weld in FSW of NiTi alloy.

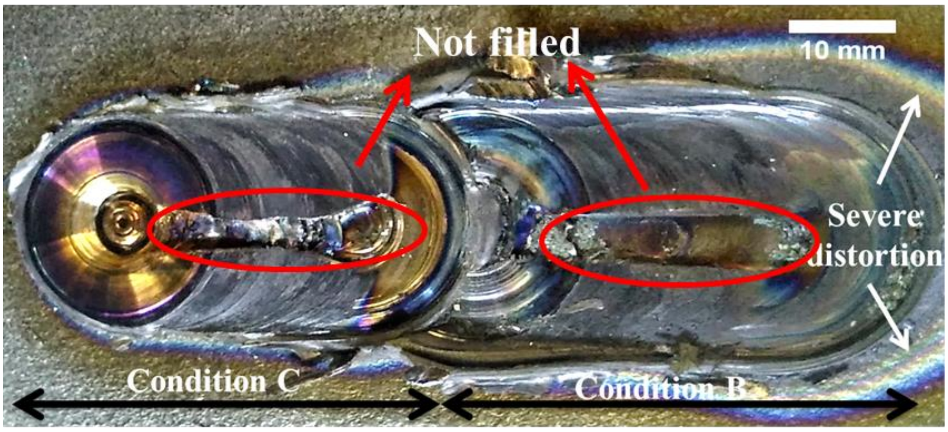

Fig. 3.6: Weld surface with defects due to improper tool geometry and process conditions

Table. 3.3: Process conditions showing different tool geometry and parameters used for welding

Condition	Tool geometry (mm)	Tool rotation (rpm)	Dwell time (s)	Traverse Speed (mm/min)	Plunge depth (mm)	Tool tilt (^{o})
A	Shoulder ⌀ -10 Pin ⌀-3, length-0.9	1500	30	50	0.3	2
B	Shoulder ⌀ -20 Pin ⌀-7, length-0.9	1500	30	25	0.2	2
C		1000	30	50	0.2	2

3.3.4 Actual experiments at different tool rotational speeds

Experiments were conducted at three rotational speeds (800 rpm, 1000 rpm and 1200 rpm) with constant traverse speed of 50 mm/min in the ambient environment without any cooling medium or shielding gas. Fig. 3.7 shows the photograph of the densimet tool used for welding. The tool tilt of 2^o has been selected which would assist in better material flow from front to the back of the tool pin. The process parameters and the tool geometry used for welding are given in Fig. 3.8.

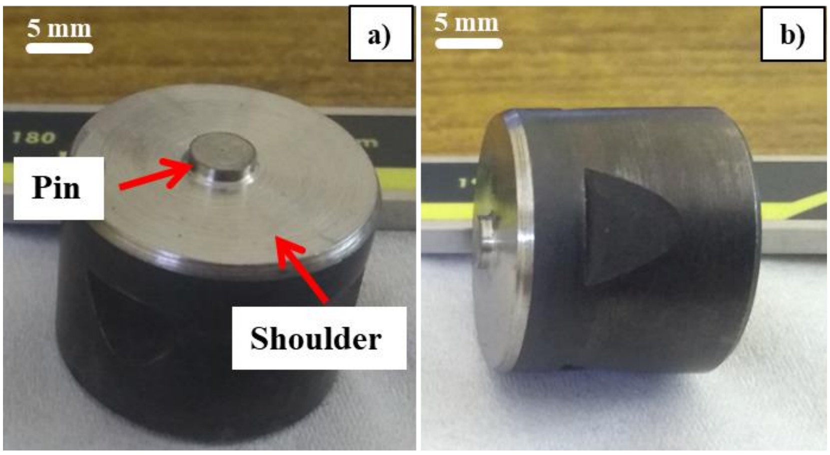

Fig. 3.7: Densimet tool with desired geometry to weld 1.2 mm thick NiTi sheet (Pin-0.9 mm height, 5 mm in diameter and shoulder 22 mm in diameter)

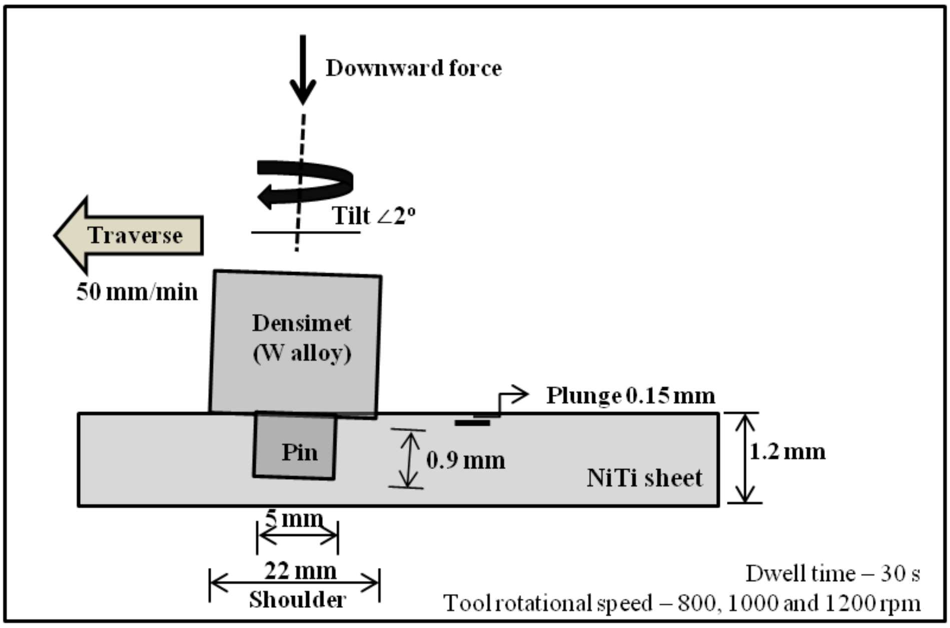

Fig. 3.8: Process parameters and tool geometry used for welding NiTi alloy

Fig. 3.9 shows the photograph taken during welding which depicts the NiTi sheets fastened in a fixture, rotating tool holder and the welding zone.

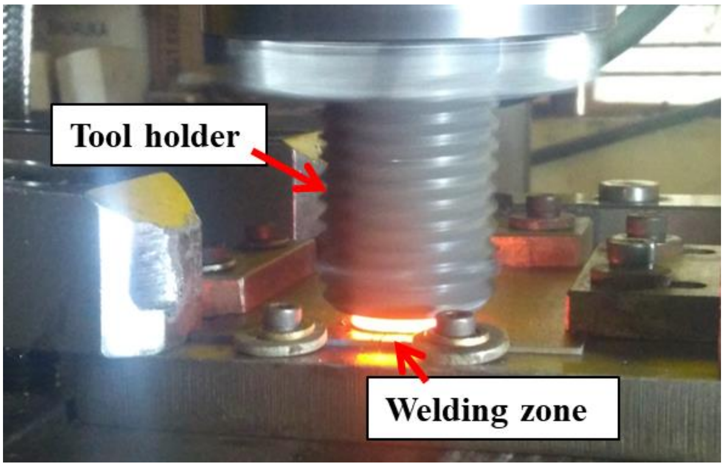

Fig. 3.9: Photograph taken during welding of NiTi alloy

Fig. 3.10a shows the top and bottom surface of the welded region. It depicts the plunging-dwell zone, welding stage and the clearly evident exit hole due to final tool retraction from work material. Initially, the rotating tool plunges in to the material and dwells in the same place for 30 s to plasticize the material in the vicinity of the tool pin region in order to initiate the welding process. After the dwelling stage, the welding takes place where the rotating tool traverses along the line of joint. After covering the specified welding length, the tool retracts from the welding material and leaves a characteristic exit hole in the workpiece. The axial load exerted during the interaction between the tool and workpiece is shown in Fig.3.10b. Since, NiTi alloy is a hard material, a maximum load of 11.5 kN was recorded for 800 rpm. The increase in tool rotational speed increases the welding temperature which eventually decreases the axial load required for welding. As seen from Fig. 3.10c, the higher tool rotational speed has encountered comparably lesser axial load. The maximum axial load at 1000 rpm and 1200 rpm were 10.7 kN and 9.3 kN respectively.

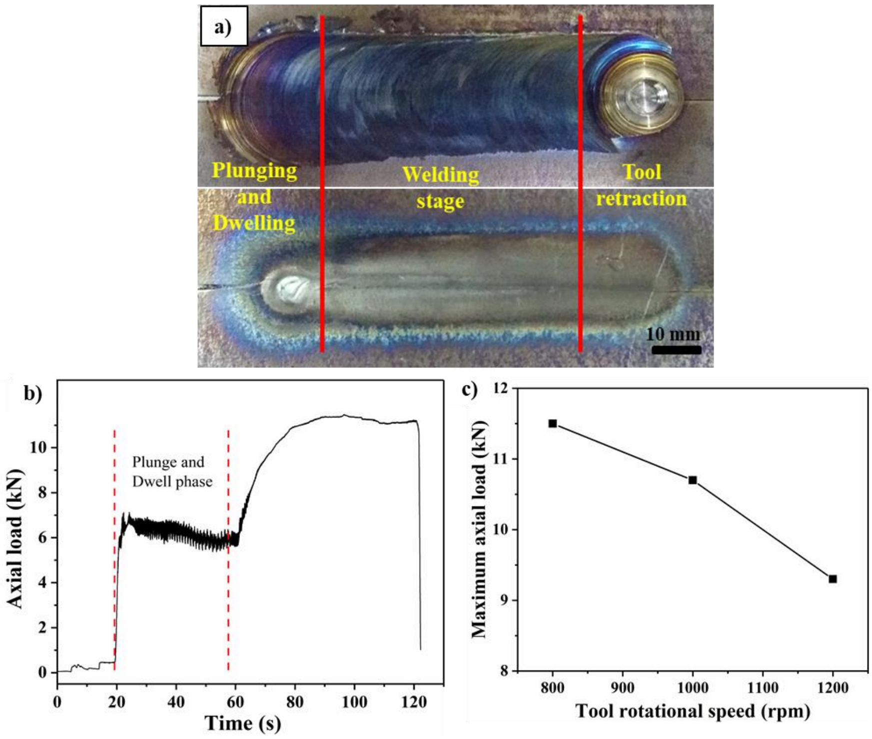

Fig. 3.10: a) Top and bottom surface of the FSW NiTi at 800 rpm, b) Axial force exerted on the tool at 800 rpm and c) Effect of tool rotational speed on the axial load

The macroscopic images of the welds produced at 800, 1000 and 1200 rpm are shown in Fig. 3.11a-c. All the welds had proper consolidation of the joint without any surface defects (cracks, lack of fill etc.). The macrostructure of the weld cross section is shown in Fig. 3.11d. The zone A-B represents the transition zone from shoulder region to base metal on advancing side and retreating side of the weld respectively.

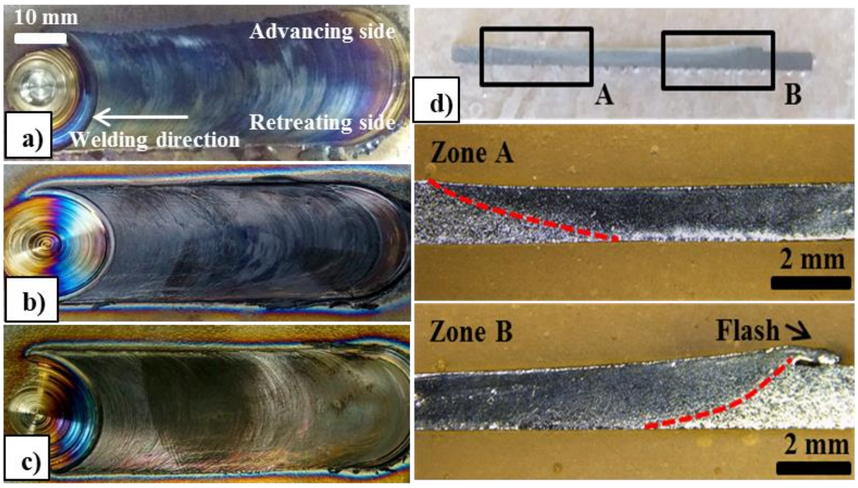

Fig. 3.11: Defect free friction stir welds at a) 800 rpm and b) 1000 rpm c) 1200 rpm and d) Macrostructure of the weld cross section at 1000 rpm

3.4 Microstructural and phase analysis

The samples for microstructural analysis were polished using various grits of SiC paper, then using alumina powder and finally etched using 50 mL H_2O + 40 mL HNO_3 + 10 mL HF solution. The microstructures were recorded using *Carl Zeiss* inverted optical microscope. The phase analysis was carried out by X-ray diffraction (XRD) technique using *X-Pert PRO PANalytical*. The characterization techniques to evaluate the microstructures, phases, hardness and stress-strain behaviour were performed at room temperature.

The microstructures of the base metal and the weld are shown in Fig. 3.12 and 3.13. The base metal has equiaxed coarse grains with grain size of 55 µm. The microstructure of the weld region for all the tool rotational speeds has fine recrystallized grains. The recrystallized grains were found throughout the weld and there was no clear distinction between nugget (stir zone), thermo-mechanically affected zone (TMAZ) and heat affected zone (HAZ).

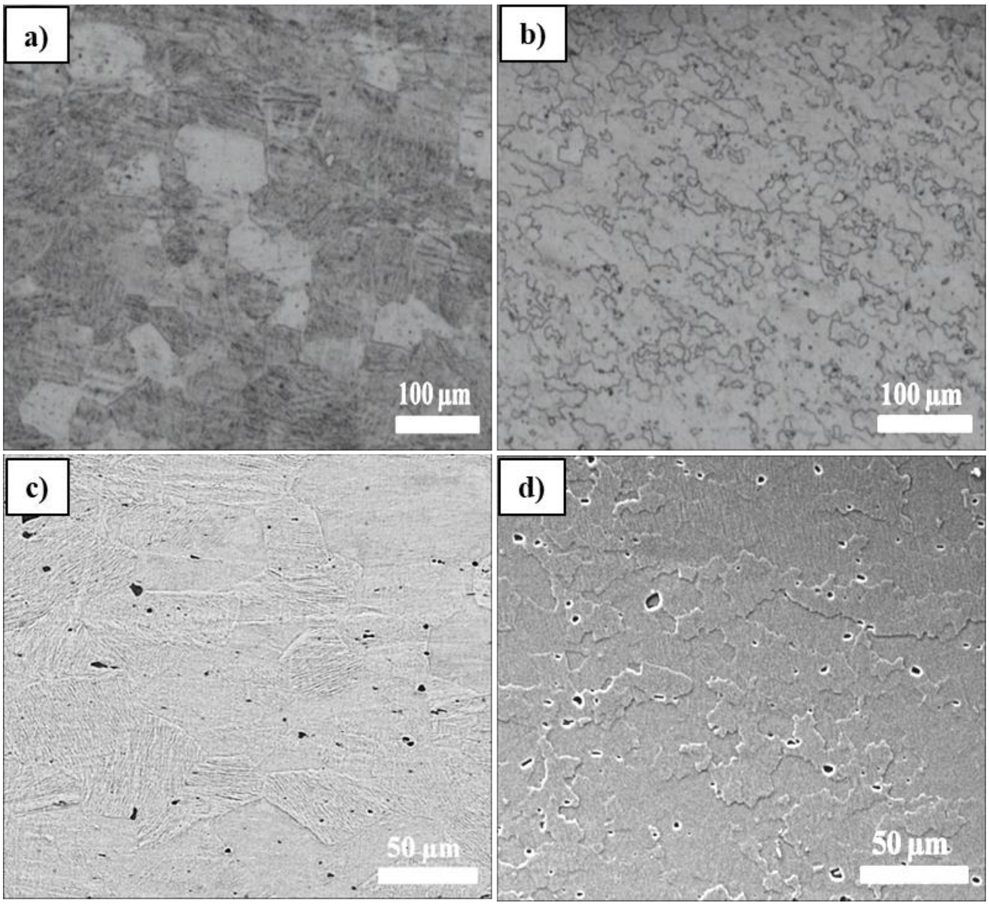

Fig. 3.12: Optical images of the a) Base metal, b) weld at 1000 rpm; SEM images of the c) Base metal and d) weld at 1000 rpm

Generally, the dynamic recrystallization takes place in the metals when subjected to hot working and it depends upon the peak temperature, plastic strain, strain rate and stacking energy of the materials [112]. In metals with high stacking fault energy like NiTi, the continuous dynamic recrystallization occurs when the temperature is greater than 50% of the melting point [113,114]. During hot compression tests of NiTi alloy, Shu-yong Jiang et al. have observed dynamic recrystallization for all strain rates for temperatures above 700^{o}C [115]. The recrystallization temperature range of hot compression test is in the same range of operating temperature of FSW, which is between 0.75-0.8 times the melting point of the material [116]. Hence, the continuous dynamic recrystallization accompanied with dynamic recovery has resulted in the formation of refined elongated grains during FSW of NiTi alloy [108]. It is noteworthy to observe that the grain size increases with the increase in tool rotational speed. Among the three tool rotational speeds, the weld at 800 rpm (Fig. 3.13a) has very fine grains and the 1200 rpm (Fig.

3.13c) weld displayed comparably larger grains. The grain sizes of the weld were 22 μm, 30 μm and 38 μm for 800, 1000 and 1200 rpm respectively. This is due to the fact that increase in tool rotational speed, increases the peak temperature which favours the grain growth [47]. In the weld at particular tool rotational speed, the temperature and plastic deformation in the adjacent regions to the nugget are lower than the nugget zone. Due to this, the recrystallization does not take place outside the nugget for most of the materials. However, in NiTi alloy, even at lower strain and higher temperature recrystallization will occur [117]. This has resulted in the formation of recrystallized grains in TMAZ and HAZ and all the regions exhibited homogeneous microstructure. Hence, the nugget, TMAZ and HAZ were not distinguishable in FSW of NiTi alloy.

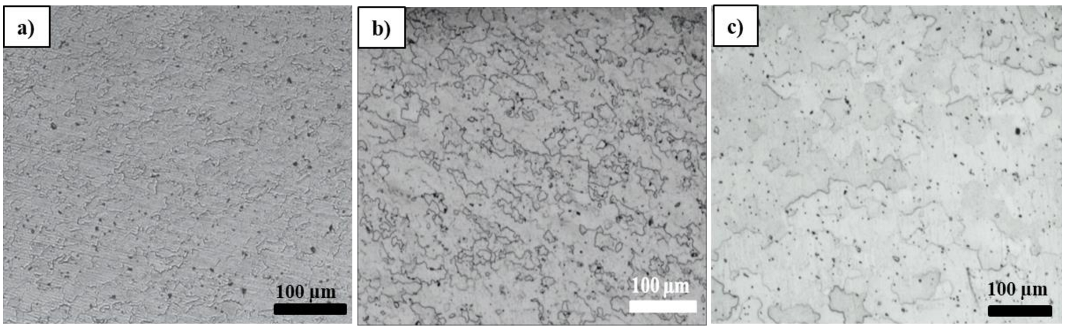

Fig. 3.13: Variation of grain sizes at different tool rotational speeds a) 800 rpm, b) 1000 rpm and c) 1200 rpm

The X-ray diffraction (XRD) analysis was carried out to evaluate the effect of FSW on the phases of NiTi. The XRD patterns of the base metal and weld regions at different rotational speeds are shown in Fig. 3.14. The indexed pattern of the BM and the weld showed that both are similar and consist of B2 cubic austenite phase with traces of B19' monoclinic martensitic phase. Intermetallic compounds ($NiTi_2$ and $TiNi_3$) commonly observed in fusion welding of NiTi and are detrimental to shape memory behaviour were absent. Further, interestingly phases of the base metal have been retained even after welding. However, in case of electron beam and laser beam welding, transformation between the martensite and austenite phases after welding was generally observed [32,118].

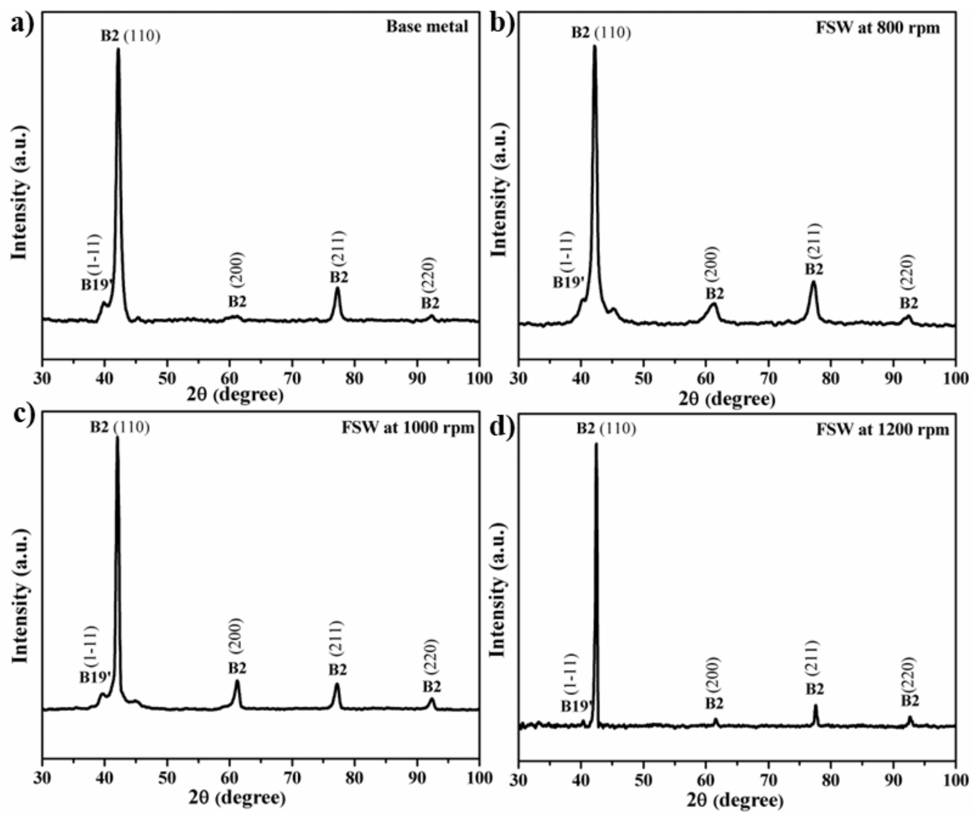

Fig. 3.14: XRD patterns of NiTi alloy before and after welding a) Base metal, b) FSW at 800 rpm, c) FSW at 1000 rpm and d) FSW at 1200 rpm

With an increase in the tool rotational speed, the coarsening of grain size and reduction of dislocation density happen and eventually decreases the spectral width of the peak [119]. Broadening of the X-ray diffraction peaks in materials mainly attributed to the following factors: Crystallite Size broadening and Strain broadening. Crystallite size is a measure of the size of coherently diffracting domains. Lattice strain is a measure of the distribution of lattice constants arising from crystal imperfections, such as lattice dislocations, twinning, grain boundary triple junction, internal stresses, stacking faults and coherency stresses. The results of XRD are in agreement with weld microstructures (Fig. 3.13) which shows coarsening of grain size at higher tool rotational speeds.

3.5 Mechanical properties of the weld

Tensile test was carried out on Instron-5967 machine at a strain rate of 10^{-3} s^{-1}. The sample cross section of 1.2 mm × 4 mm with a gauge length of 40 mm was used. The weld was present in the centre of the sample. These samples have been cut from the welding zone leaving the initial plunging and final retraction zone as shown in Fig. 3.10a. Fig. 3.15 shows the engineering stress-strain curve of the base metal and the welds. The weld produced at 800 rpm has displayed an ultimate tensile strength of 492 MPa and yield strength of 453 MPa. Interestingly, the weld produced at 1000 rpm had ultimate tensile strength of 638 MPa (66 % of the BM) and yield strength of 602 MPa which is 17 % higher than the base metal. The weld at 1000 rpm has a crucial superelastic plateau near 600 MPa until 7.25 % strain while the weld at 800 rpm showed close to 460 MPa until 5 % strain. Ultimate strength of the weld at 1200 rpm was 345 MPa which was lower among the welds produced due to the presence of hard tool fragments. The cross section of the weld (Fig. 3.15c) shows cracks close to the tool fragments which could be attributed to inhomogeneous material flow and mismatch in thermal expansion between the tool fragments and the NiTi.

In case of welding of shape memory alloys, the retainment of crucial superelastic plateau (functional property), yield strength and ultimate tensile strength are the factors defining the quality of the weld. The FSW of nitinol has shown better yield strength (due to grain refinement) than base metal at 1000 rpm and the welds at 800 and 1000 rpm has shown the crucial superelastic plateau. It is important that the FSW has shown higher yield strength (compared to base metal) than most of the reported welding techniques such as electron beam welding, laser welding, tungsten arc welding [27,39,41,120]. On the other hand, the ultimate tensile strength depends on the bonding of the weld joint and the weak point across the weld structure acts as the nucleating point for fracture. In FSW of nitinol, the interface between the base metal and the weld region (transition zone from refined grains of weld to coarse grains of base metal) acts as weak point for the fracture. All the welded samples have broken at heat affected zone i.e. the week interface zone. So, the joint efficiency can be improved by further detailed optimization on tool selection, tool geometry design and process parameters to enhance the plasticization of material across the weld zones.

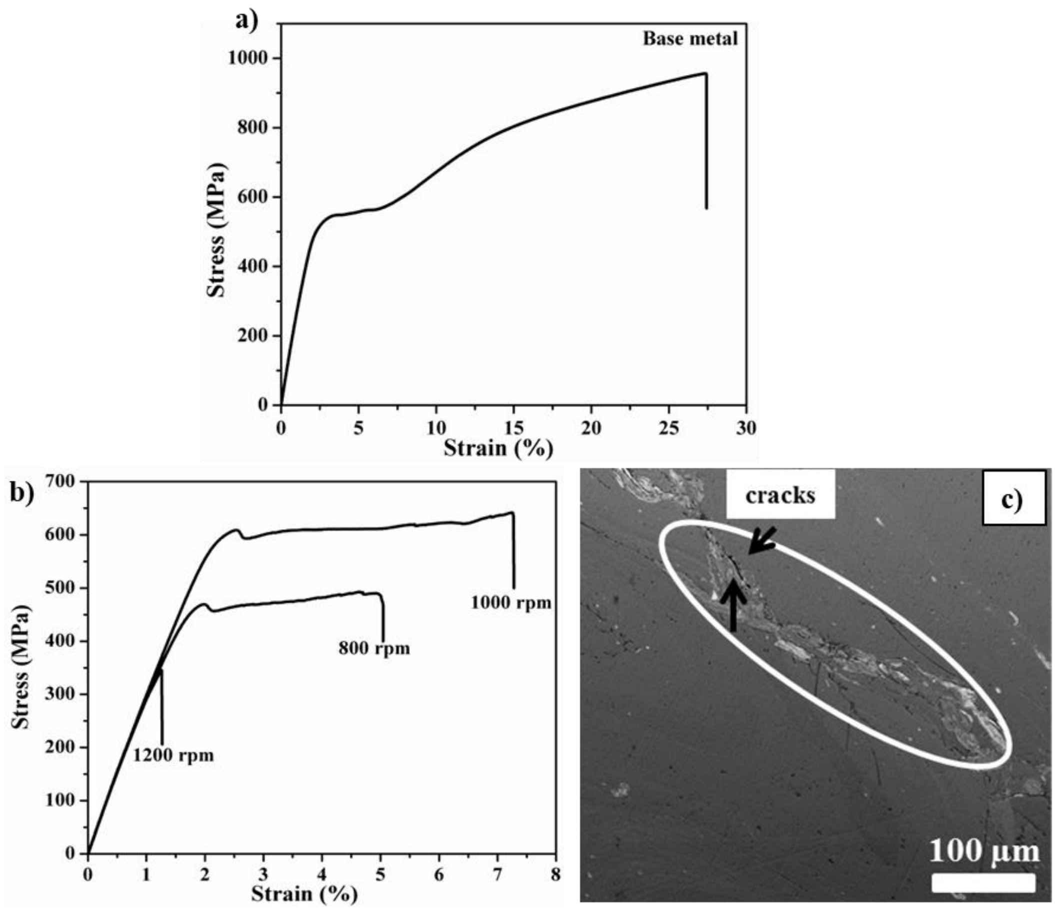

Fig. 3.15: Engineering stress-strain plot of the base metal, b) Engineering stress-strain plot for the welds produced at different tool rotational speeds and c) Cross sectional SEM images of the weld at 1200 rpm showing cracks

The fracture surfaces of the weld and the BM observed using scanning electron microscope are shown in Fig. 3.16. The fracture surface of the BM and the welds except at 1200 rpm showed dimples indicating ductile fracture. The fracture surface of the weld at 1200 rpm show smooth surface indicative of brittle fracture. Further, the micro cracks which could have been originated at the tool fragments are seen in Fig. 3.15d.

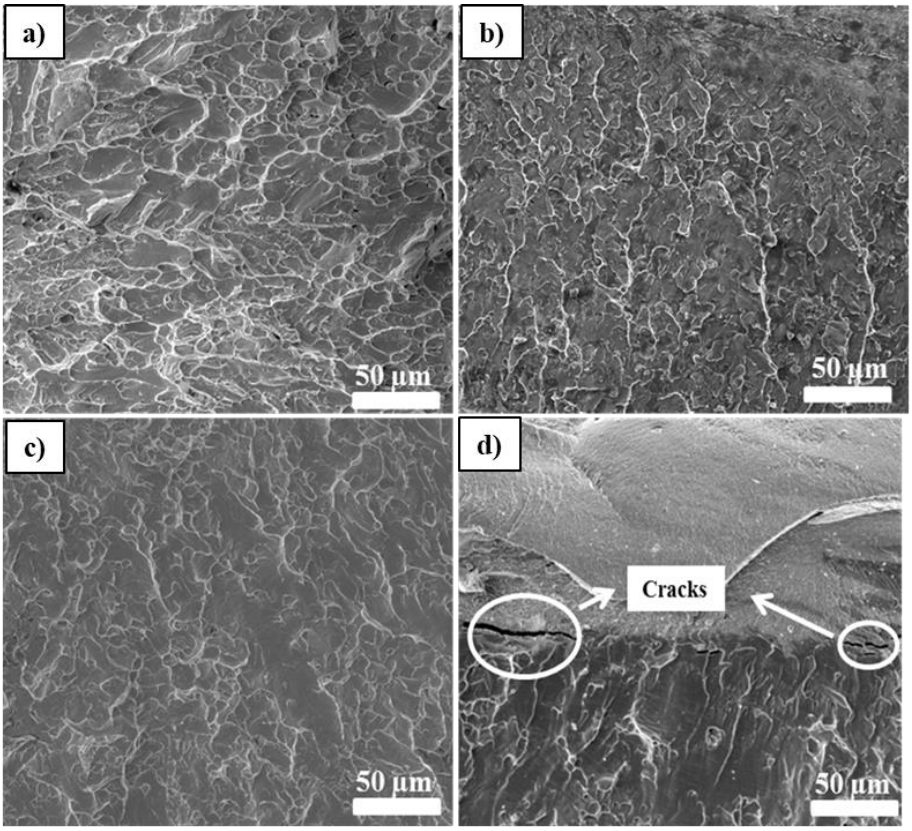

Fig. 3.16: Fracture surfaces of the tensile specimen a) Base metal, b) weld at 800 rpm, c) weld at 1000 rpm and d) weld at 1200 rpm

Vickers microhardness measurements were taken along the cross section of the weld using the FM-800 Future Tech Corp at 500gf load for 15 seconds. Micro hardness of the weld cross section and scanning electron microscope (SEM) images of the weld at 1200 rpm is shown in Fig. 3.17 and 3.18 respectively. The average hardness of the weld at 800 rpm, 1000 rpm and 1200 rpm were 275 HV, 262 HV and 284 HV respectively. Few high hardness values were noticed in 1200 rpm weld due to tool fragments included and distributed across the weld region. The distribution of tool fragments across the weld could be attributed to the severe plastic deformation and high temperature experienced at 1200 rpm than the other rotational speeds. The weld at 800 rpm and 1000 rpm has showed marginally lower hardness than the base metal (BM).

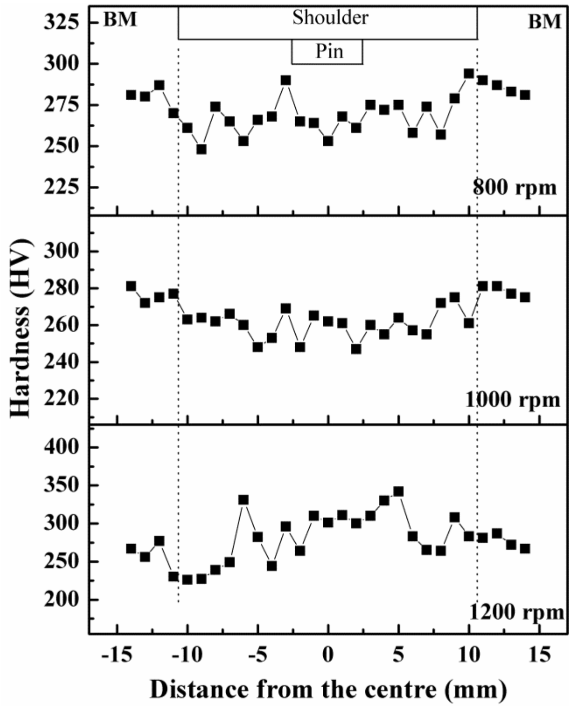

Fig. 3.17: Microhardness of the weld cross section at different tool rotational speeds

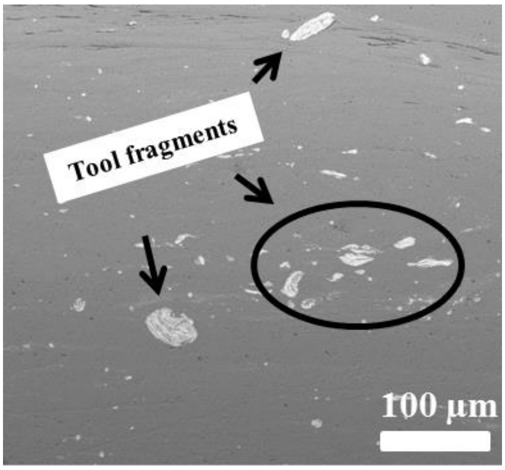

Fig. 3.18: Cross sectional SEM image of the weld at 1200 rpm showing tool fragments

3.6 Composition analysis

The welds produced at all the tool rotational speeds have tool fragments included during the FSW process. The tool fragments are found in the nugget region especially in and around the weld centre. The composition analysis in the cross section of the weld produced at 1000 rpm is shown in Fig. 3.19. The weld region away from the weld centre has material composition close to equiatomic as seen from Fig. 3.20a. The centre of the weld has shown a deviation from the actual alloy composition due to the presence of tungsten inclusions (Fig. 3.20b). Fig. 3.20c shows the EDS analysis of the tool fragment which confirms the presence of tungsten inclusions. The fragmented tool particles during welding would have stirred in the flow and gets included in the nugget zone. It clearly shows the close composition of the weld as of the base material except the weld centre.

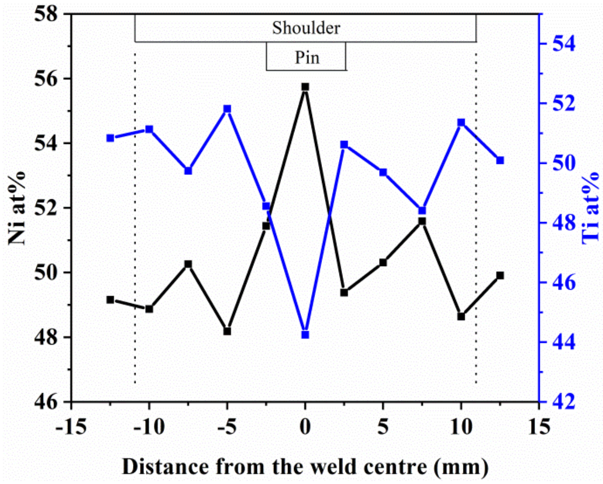

Fig. 3.19: Composition analysis in the cross section of the welded sample using EDS

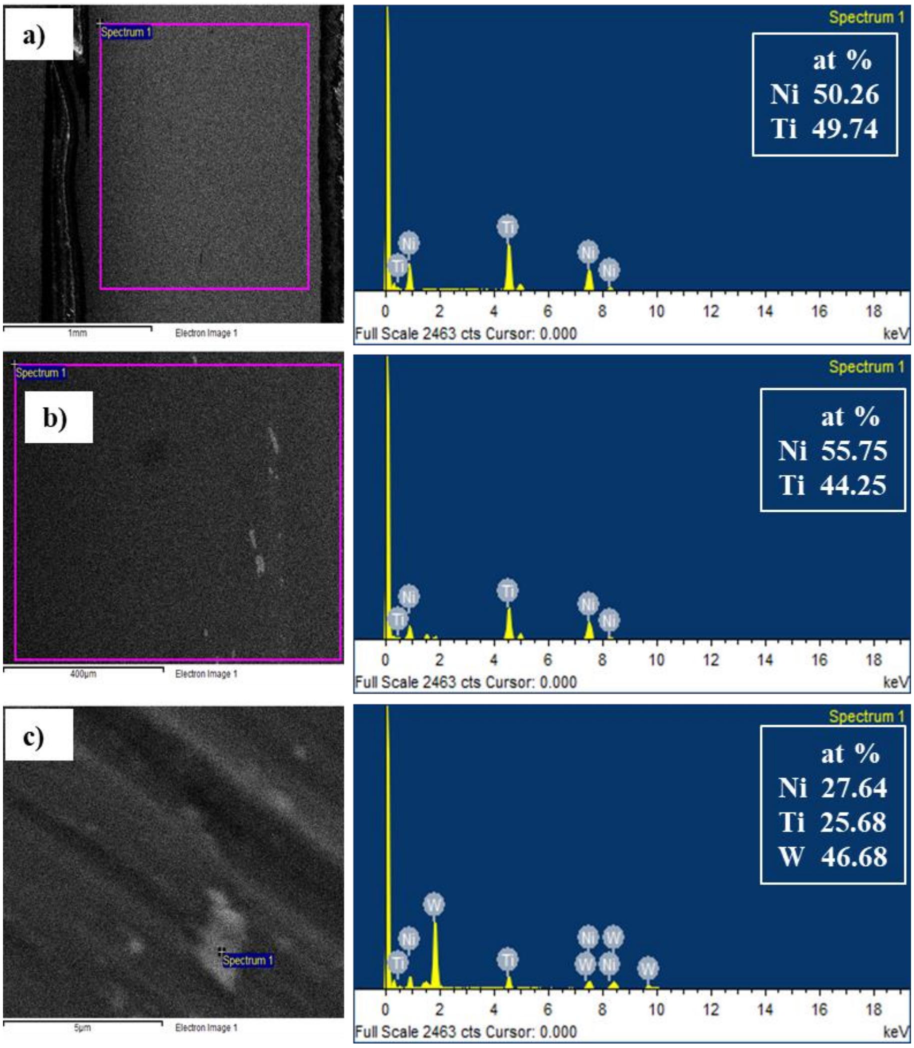

Fig. 3.20: Composition analysis in the cross section of the welded sample using EDS a) Away from the weld centre, b) Centre of the weld and c) Tool fragments included in the weld centre

3.7 Tool damage and inclusions in the weld

As mentioned earlier, NiTi (SE508 grade) is a hard material (>250 HV) having a high melting point of 1310ºC. In FSW technology, these alloys fall under the category of high softening temperature (HST) materials along with steel, stainless steels and Ti alloys. During FSW of HST materials, the tool encounters extreme adverse conditions of high temperature and flow stresses which eventually leads to tool wear [121,122]. The FSW of NiTi at the tool rotational speed of 1000 rpm generated high temperatures up to 922ºC in the stir zone [123]. Fig. 3.21 shows the densimet tool after a welding length of 70 mm. A change in tool configuration with reduced pin height and adhesion of NiTi material to the shoulder region was clearly evident. The tool pin is structurally weaker than shoulder due to the characteristic slender shape and its complete immersion in the workpiece during welding. The pin experiences substantial wear and deformation due to the severe bending and torsional stresses resisting the stirring and translational motion of the tool [124]. The tool degradation or wear usually starts in the initial plunging and dwelling phase itself. During plunging, the tool pin experiences a sudden increase in axial force and transverse shear stresses. A very high axial force of around 12 KN was recorded during welding of NiTi. Due to the small pin diameter of 5 mm, the stress would have developed beyond yield strength leading to severe plastic deformation of the pin.

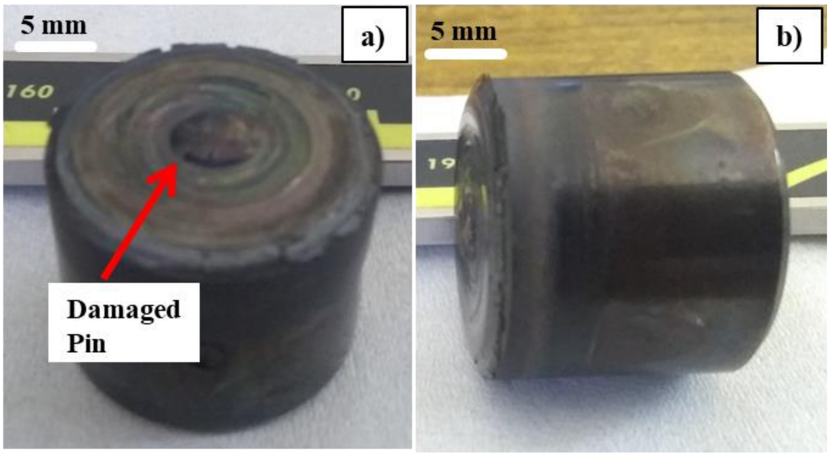

Fig. 3.21: Densimet tool with damaged pin after welding

3.8 Phase transformation behaviour of the weld

Differential scanning calorimetry (DSC) is a thermal analysis technique which gives information on the change of heat capacity with respect to temperature. The heat flow to the sample of known mass will be compared with a standard sample at the specified heating/cooling rate. The change in heat flow will give information on melting, glass transition, phase transformation, curing etc. It's a popular characterization technique used in sectors such as pharmaceuticals, food, paper, agriculture, and electronics. Since, the NiTi alloy undergoes solid state phase transformation; DSC can be used to find the phase transformation temperatures.

Samples were cut from nugget, retreating side and advancing side of the weld joint (Fig. 3.22) for studying the phase transformation behaviour using DSC. The phase transformation behavior was studied using *Netzsch-DSC214 Polyma* DSC machine at a heating/cooling rate of 10^{o}C/min with a constant flow of nitrogen.

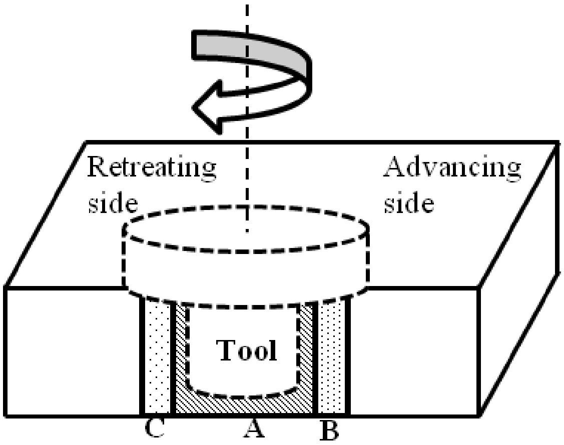

Fig. 3.22: Schematic of the DSC sample regions (A-Nugget, B-Advancing side and C-Retreating side)

The DSC curves of the base metal and the weld nuggets at different tool rotational speed are shown in Fig. 3.23. A_s, A_f, M_s and M_f are the austenite-martensite start and finish transformation temperatures. These transformation temperatures are given as an inset in Fig. 3.23. The DSC curves of base metal and weld nuggets at 800 and 1000 rpm depict the exothermic peaks during the forward transition from austenite to martensite (B2→R→B19'or B2→B19') on cooling. Further, they depict the endothermic peaks during the reverse transition from martensite to austenite (B19'→B2) on heating. Fig. 3.21d shows the DSC curve of the weld nugget at 1200 rpm during heating and cooling cycles. The transformational temperatures of the base metal and weld nugget of 800 rpm were very close to each other. However, the martensite transformation temperatures (M_s and M_f) of weld nuggets of 1000 have increased after welding. Fig. 3.24 and 3.25 shows the DSC curves of advancing and retreating side of the weld at different tool rotational speeds. The phase transformation temperatures of both sides of weld at 800 rpm were close to the base metal. But the martensite transformation of both sides of the weld at 1000 rpm has shown a drift towards the positive direction. In case of the weld at 1200 rpm, the transformations are different and unusual from the base metal and the other welds. So, these transformations are represented as T_s and T_f during heating and cooling cycles respectively. This unusual pattern could plausibly due to microstructural heterogeneities and tool inclusions across the weld regions.

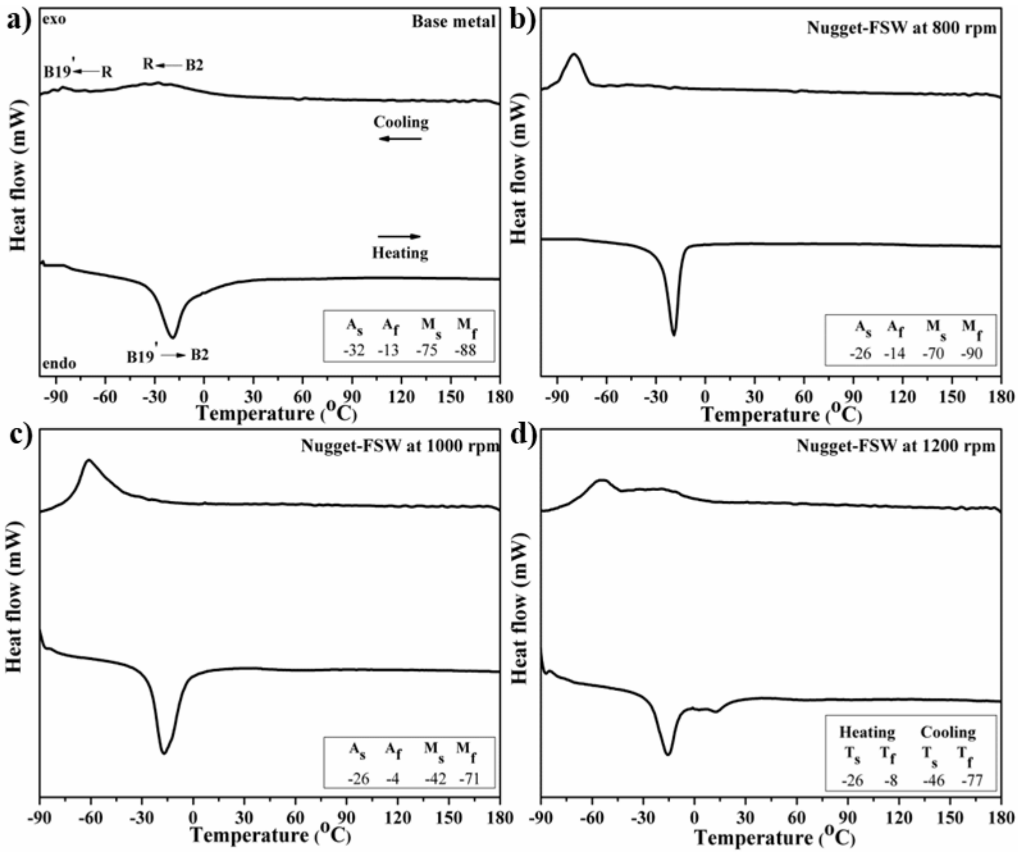

Fig. 3.23: DSC curves of NiTi alloy before and after welding a) Base metal, b) Nugget of the weld at 800 rpm, c) Nugget of the weld at 1000 rpm and d) Nugget of the weld at 1200 rpm

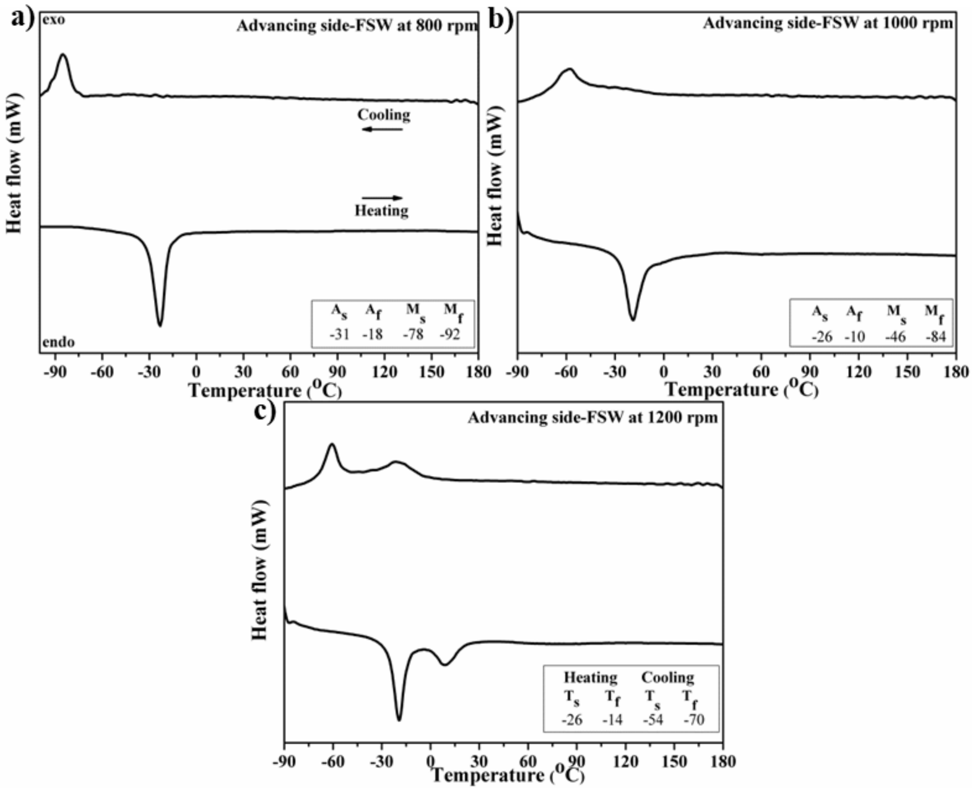

Fig. 3.24: DSC curves of advancing side of friction stir welded NiTi alloy a) FSW at 800 rpm, b) FSW at 1000 rpm and c) FSW at 1200 rpm

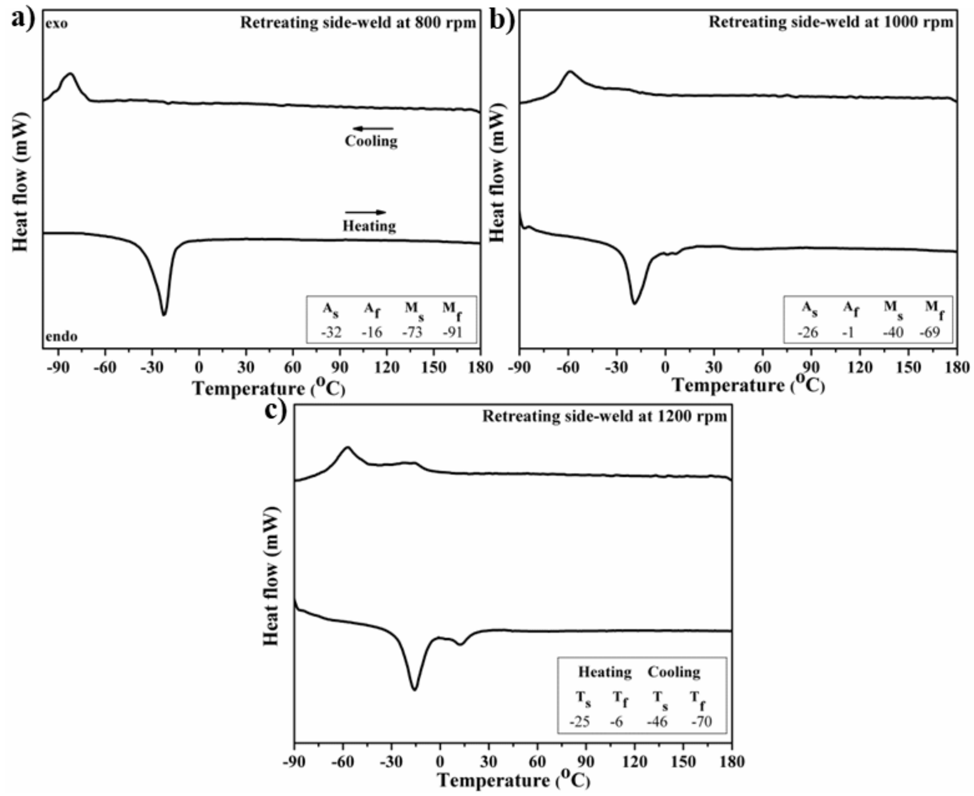

Fig. 3.25: DSC curves of retreating side of friction stir welded NiTi alloy a) FSW at 800 rpm, b) FSW at 1000 rpm and c) FSW at 1200 rpm

The hysteresis due to dissipative work is the interval between heating and cooling transformations i.e. $|As - Mf|$ and $|Ms - Af|$ [125–127]. The hysteresis for the base metal and the weld at different rotational speed is given in Table 1. The hysteresis (A_s – M_f) has reduced for weld at 1000 whereas increased for the weld produced at 800 rpm.

Table 3.4 Hysteresis of the phase transformation behaviour at different weld regions

Weld region	Process conditions	$\|As - Mf\|$ (°C)
	Base metal	56
Nugget	800 rpm	64
	1000 rpm	46
	1200 rpm	-
Advancing side	800 rpm	61
	1000 rpm	58
	1200 rpm	-
Retreating side	800 rpm	59
	1000 rpm	43
	1200 rpm	-

3.9 Summary

The friction stir welding of NiTi alloy was successfully carried out with high capacity machine. The selection of tool material and the geometry has been discussed. The complete process parameters required to weld NiTi alloy using FSW was explored. The dynamic crystallization has happened in the weld and which has enabled better yield strength for the weld at 1000 rpm. Detailed investigations have been performed for analysing the phase transformation behaviour across the welds. Interestingly, the composition analysis revealed close composition compatibility with the base metal. Tool wear seems to be the important problem which has to be addressed to further explore the possibilities in FSW of NiTi alloys.

Chapter 4

Elucidation on Temperature Distribution and Strain Rate during Friction Stir Welding of NiTi using Finite Element Analysis

4.1 Introduction

As we know, FSW is a thermomechanical process where frictional heat and plastic deformation acts simultaneously to weld the work material together. During welding, the plastic flow of the material around the tool is affected by the strain rate (rate of plastic deformation) and flow stress of the material. The peak temperature, temperature distribution and strain rate are significantly influenced by the tool rotational speed. So, it is important to understand the conditions of temperature and strain rate during welding in order to corroborate the changes with the weld properties. Usually, temperature during FSW will be measured by embedding thermocouples into the region near to the weld. Since, the NiTi alloy is very hard, drilling holes for thermocouples was not compatible. In case of thermocouple method, only the maximum welding temperature can be found and the temperature gradients existing across the weld region cannot be ascertained. Hence, the finite element analysis is used to predict the peak temperature and temperature distribution across the weld region. Furthermore, the velocity fields and strain rate signifying the material flow have been evaluated. The FSW of NiTi alloy was simulated using Comsol Multiphysics 5.3a based on finite element method.

4.2 Finite element analysis for maximum temperature and temperature distribution during welding

4.2.1 Modelling and analysis set up

During FSW, the heat is generated due to interaction between the shoulder/workpiece and pin/workpiece interfaces. The tool pin may contribute up to 20 % of the total heat generated during welding [47,48]. However, in most of the models, the heat generation due to tool pin/workpiece was neglected [79,85,128]. Here, the model used for the study was based on the work done by Song et.al [129]. In this model, the heat input from both the tool pin and shoulder was considered. Based on the same model, the temperature distribution during FSW of stainless steel and aluminium was reported [128,130].

The dimension used for simulation was 100 mm × 40 mm × 1.2 mm with infinite domains along the X-axis. The welding process parameters and the material properties of tool and work piece have been used for simulation. The governing equation of heat generation in pin-workpiece (Q_{pin}) considering the evolution of heat due to shearing of the workpiece and friction is given by,

$$Q_{pin} = \frac{2\pi n\mu}{\sqrt{3(1+\mu^2)}}\bar{Y}\,\mathrm{R_p} \tag{4.1}$$

The heat generation at the shoulder-workpiece ($Q_{shoulder}$) interface is given by,

$$Q_{shoulder} = 2\pi\mu\frac{F_n}{A_{shl}}\mathrm{R_s}n \tag{4.2}$$

Where μ-coefficient of friction, R_s-shoulder radius (mm), F_n-plunge force (kN), A_{shl}-surface area (mm^2), n-tool rotational speed (RPM), $\bar{Y}$-average shear stress of the material (MPa) and R_p-pin radius (mm).

Upon heat generation due to the rotation of the tool, the heat will transfer from the vicinity of the weld to the surrounding via both convective and radiative mode of heat transfer. The governing heat transfer equations for conductive heat transfer in the material (Q) and convective-radiative heat transfer from the workpiece is given by the following equations.

$$\rho C_p u.\,\nabla T = \nabla.\,(k\nabla T) + Q \tag{4.3}$$

$$Q = hA(T_0 - T) \tag{4.4}$$

$$Q = \varepsilon\sigma(T_0^4 - T^4) \tag{4.5}$$

Where ρ-density (Kg/m^3), C_p-specific heat (J/Kg K), u-welding speed (mm/min), k-thermal conductivity (W/m K), h- heat transfer coefficient (W/m^2 K), A-surface area of exposed surface (mm^2), ϵ-surface emissivity, σ-Stefan-Boltzmann constant and T_0-ambient temperature. At the tool shoulder and tool pin, the heat flux boundary condition with the workpiece interface is given by the equation 4.1 and equation 4.2 respectively. The boundary surfaces exposed to the surrounding atmosphere is subjected to convective and radiative heat transfer as given by the equation 4.4 and 4.5. The symmetry boundary condition is assumed at the contact between the two plates. At the initial time t=0, the temperature of the plate is equal to the ambient temperature.

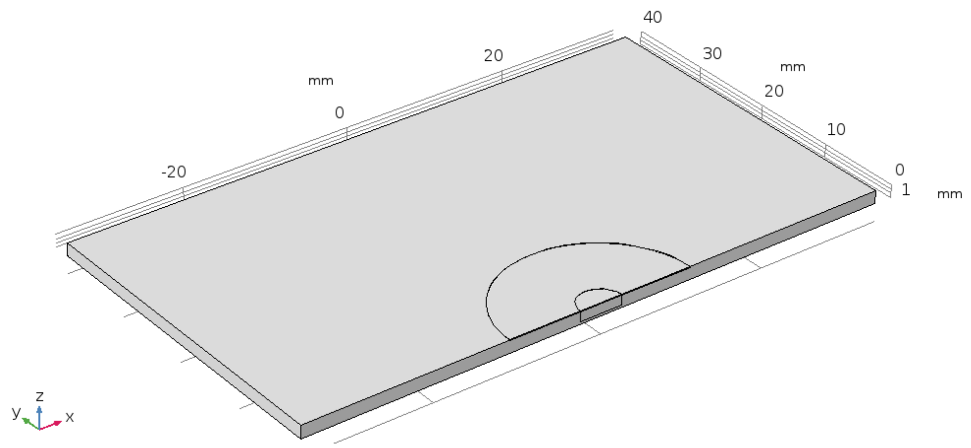

Fig. 4.1: Material geometry with tool in the middle of the section

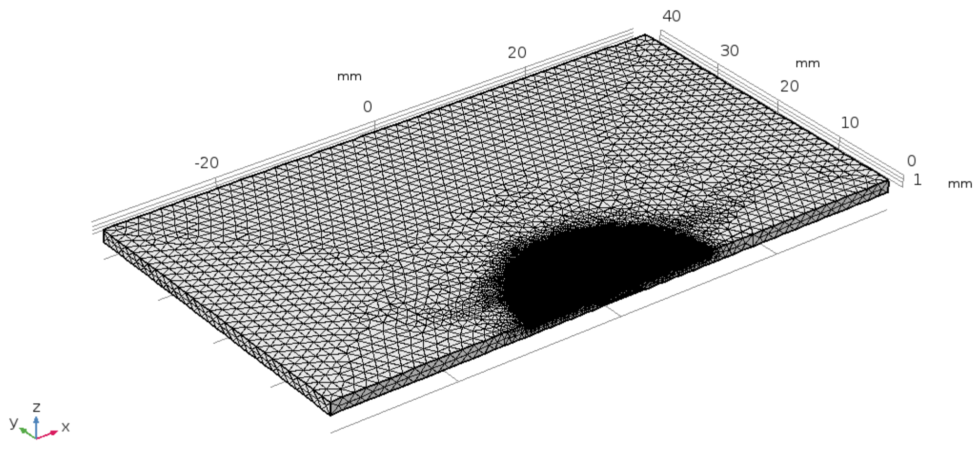

Fig. 4.2: Finite element mesh for FSW of NiTi alloy

4.2.2 Temperature distribution at different tool rotational speed

The temperature distribution at different tool rotational speed is shown in Fig. 4.3a-c. The increase in tool rotation speed has increased the maximum temperature during welding. This is due to the fact that higher rotational speeds generates more heat due to friction and leads to intense stirring and mixing of the material in the weld zone. The FSW at 1200 rpm has shown a highest temperature of 1094°C. The maximum temperature was recorded in the edge of the pin on the advancing side. In the advancing side, the tangential velocity vector and the forward velocity vector acts along the same direction. Hence, the advancing side has shown higher temperature than the retreating side for all the tool rotational speeds.

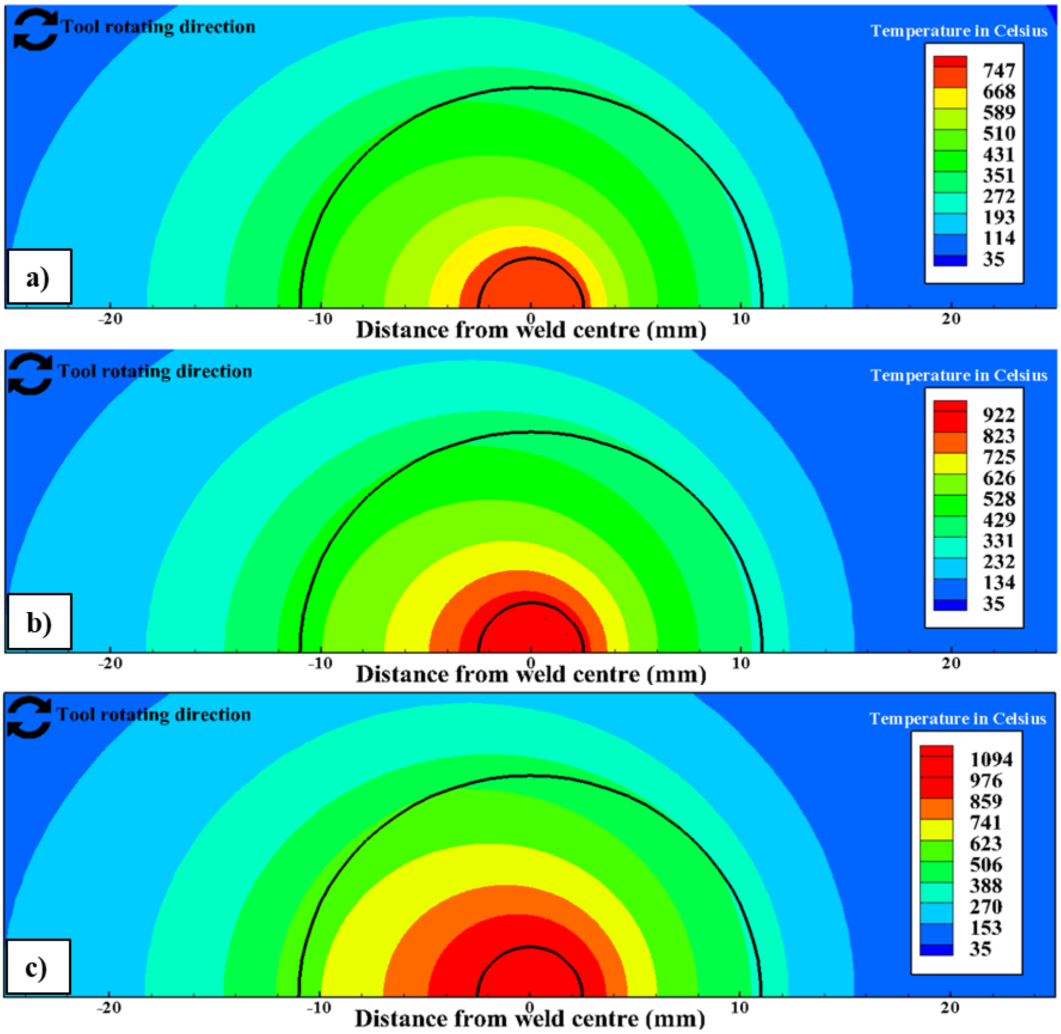

Fig. 4.3: Temperature distribution during FSW of Nitinol a) Weld at 800 rpm b) Weld at 800 rpm and c) Weld at 800 rpm

The schematic of the temperature probe across the weld region is shown in Fig. 4.4. The temperature of the weld at different points across the weld viz. nugget centre (NC), peak temperature (PT), advancing side (AS) and retreating side (RS) is shown in Fig.4.5.

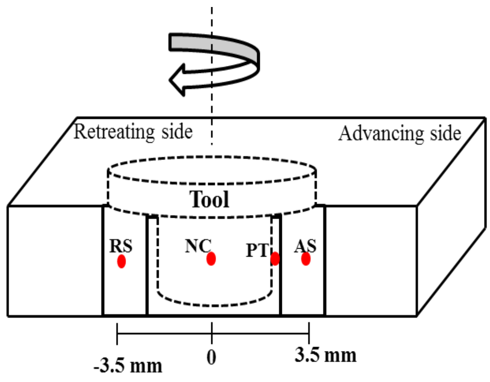

Fig. 4.4: Schematic of temperature probe at different locations across the weld region-nugget centre (NC), peak temperature (PT), advancing side (AS) and retreating side (RS)

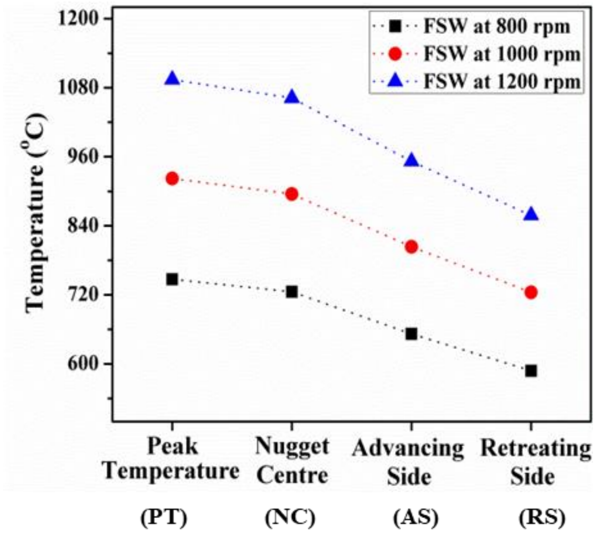

Fig. 4.5: Comparison plot showing temperature at different locations of the weld

The simulation has been validated based on the temperature recorded during welding using a non-contact infrared thermometer. High temperature infrared thermometer (Testo-835-T2) having a capability to measure temperature up to 1500ºC was used for the temperature measurements. During measurements, the region in the welding zone close to the rotating pin was focused (emissivity-0.9). The maximum temperature was measured for the rotational speeds viz. 800 rpm, 1000 rpm and 1200 rpm. From the measurement, it was found that the real time temperature measurement values had slight variation and a difference of (±30ºC) existed between the simulation and the infrared thermometer measurements. This deviation could be attributed to the heat loses and other discrepancies during experiments.

4.3 Finite element analysis for strain rate during welding

The model used for simulation is based on the work done by Saha et al. [131]. The 3D model was created in a cartesian coordinate system which consists of NiTi sheet of dimension 100 mm × 40 mm × 1.2 mm. In the middle of the 3D model, the densimet tool was configured with the material properties. For the modelling, the temperature dependant properties and contact condition between the tool and the work material has been utilized. In order to simplify the process modelling and to avoid unnecessary complications, the weld material was assumed to be moving in backward direction (In actual process, the tool moves in forward direction). Fig. 4.6 and 4.7 shows the 3D model and meshed geometry respectively.

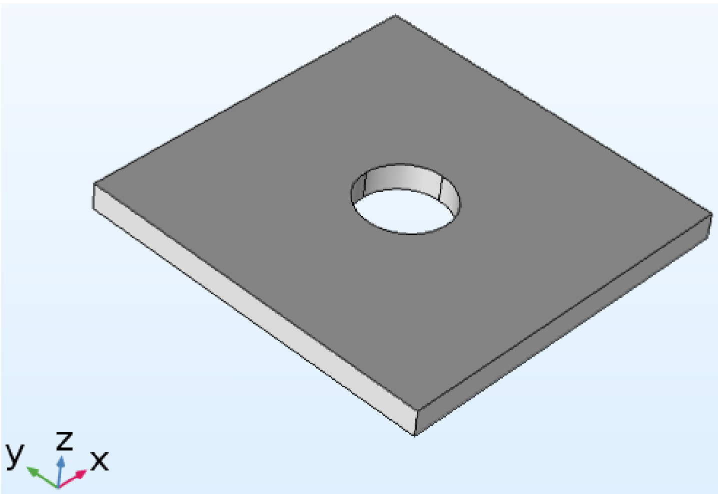

Fig. 4.6: 3D model used for simulation of strain rate with tool in the centre of the section

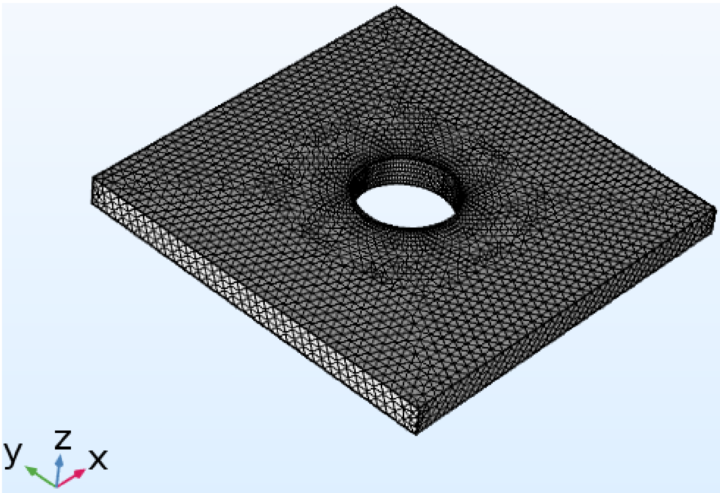

Fig. 4.7: Meshed geometry of the 3D model

The work-piece material is idealized as a fluid. The Navier-Strokes application for an incompressible fluid flow is followed to do the flow modelling. It is defined for a variable viscosity and constant density. The momentum balance equations is

$$\frac{\partial u}{\partial t} - \nabla\eta(\nabla \mathrm{u} + (\nabla \mathrm{u})^T) + \rho(u.\nabla)\mathrm{\mu} + \nabla \mathrm{p} = \mathrm{F} \tag{4.6}$$

Where η is the dynamic viscosity, u is the velocity vector, ρ is the density, p is the pressure and F is the body force term.

The continuity equation for incompressible fluids is

$$\nabla.\mathrm{u} = 0 \tag{4.7}$$

The modelling of the rotation of tool is done by following rotational velocity in x and y axis. These equations are applied to boundaries between the tool face and the work piece.

$$u_{rot} = -u * y \tag{4.8}$$

$$v_{rot} = -u * x \tag{4.9}$$

The x and y velocity vectors are generated at every point by these equations on the boundary which depends on the distance from the tool centre. This rotation spreads throughout the plate. Therefore, under a given viscosity, combining the effects of transverse speed and rotational speed, an internal velocity is generated.

The material property correlating the flow stress and the strain rate is viscosity which is defined as:

$$\mu = \frac{\sigma_e}{3\varepsilon} \tag{4.10}$$

where $\sigma_e$is the effective stress or the flow stress as defined as

$$\sigma_e = \frac{1}{\alpha} sinh^{-1}\left[\left(\frac{Z}{A}\right)^{\frac{1}{n}}\right] \tag{4.11}$$

And ε is the effective strain rate, defined as

$$\varepsilon = A(sin\alpha\sigma)^n \exp\left(\frac{-Q}{RT}\right) \tag{4.12}$$

Where Z is the Zener-Holloman temperature, Q is the temperature independent activation energy, R is the gas constant, α, A and n are model constants.

In the present model, the Carreau viscosity phenomenon is used as an alternative way to implement the non-linear viscosity behaviour of the material.

$$\eta = \eta_\infty + (\eta_0 - \eta_\infty)\left[1 + \left(\gamma\lambda \exp\left(\frac{T_0}{T}\right)\right)^2\right]^{\frac{(m-1)}{2}} \tag{4.13}$$

Where η_∞ is the infinite shear viscosity, η_0 is the zero shear viscosity, γ is the shear strain rate, λ is the time constant, T_0 is the reference temperature, m is the power law index for non-Newtonian fluid.

The material flow due to tool movement can be analysed by understanding the velocity fields and the strain rates during welding. Fig. 4.8 shows the velocity fields around the tool pin at different tool rotational speeds. Due to the increase in tangential velocity vector at higher rotational speeds, the velocity fields of the material flow increases. It can be clearly seen that the maximum values of the velocity flow has increased at increasing tool rotational speeds. The velocity fields at 800 rpm, 1000 rpm and 1200 rpm were 14.2 mm/s, 14.6 mm/s and 15.1 mm/s respectively.

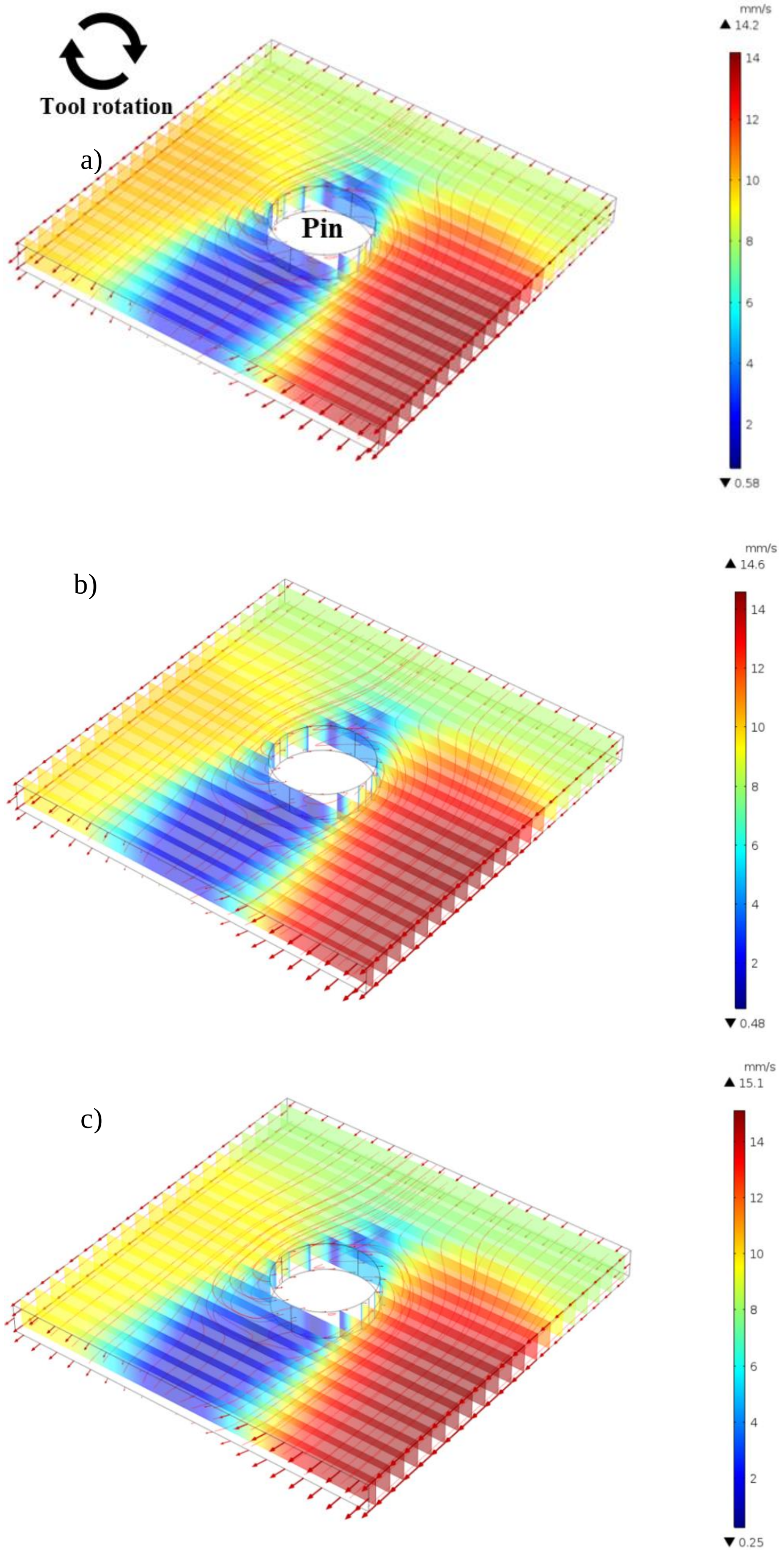

Fig. 4.8: Evolution of velocity fields around the tool pin at different tool rotational speeds a) 800 rpm, b) 1000 rpm and c) 1200 rpm

Fig. 4.9 shows the strain rates at different tool rotational speeds. It is observed that the middle section lying close to the pin region has maximum strain rates and the strain rate reduces away from the pin. Along the pin edges, the strain rates were higher because the material flow close to the pin region will be significantly influenced by the tool rotation. The influence of tool rotational speed on strain rate is represented in Fig. 4.10. The strain rate increases linearly with the tool rotational speed. At higher tool rotational speeds, the temperature and velocity increases which eventually increases the strain rates.

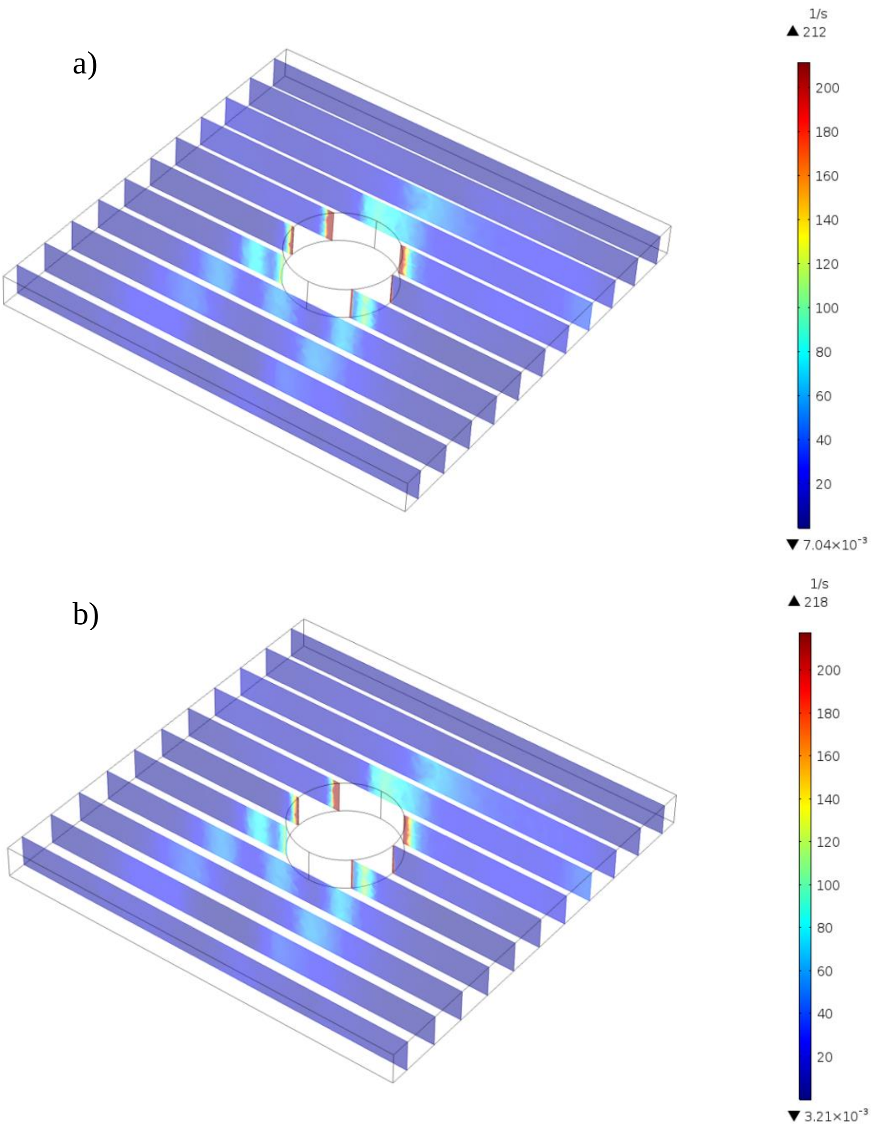

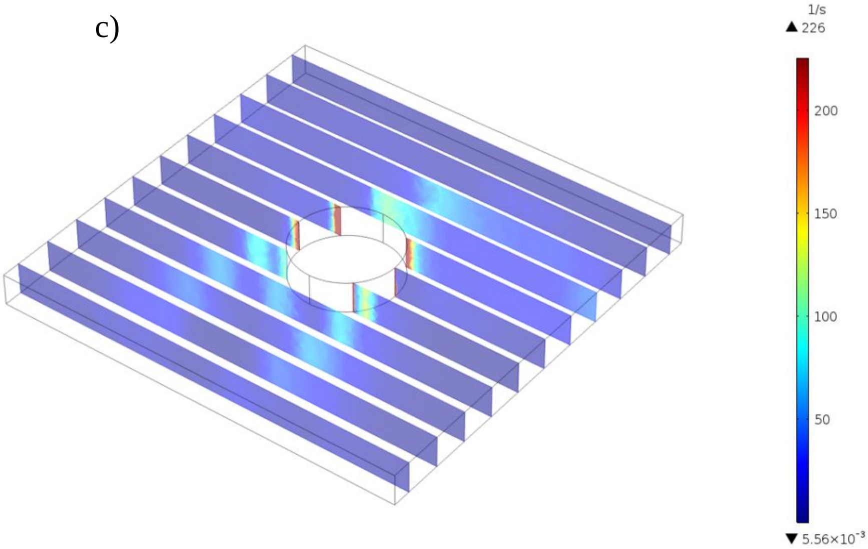

Fig. 4.9: Strain rate distribution during welding at different tool rotational speeds a) 800 rpm, b) 1000 rpm and c) 1200 rpm

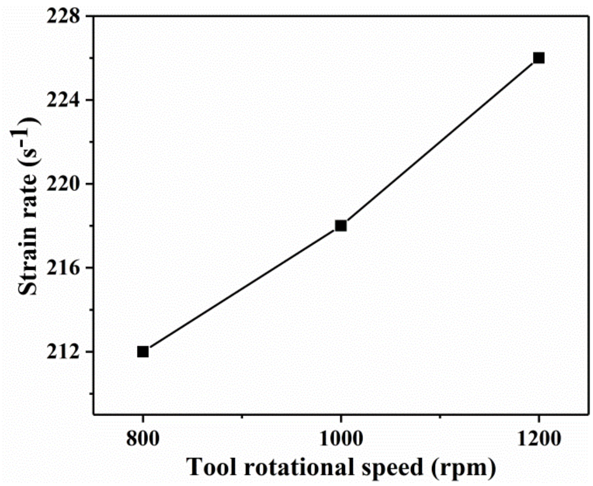

Fig. 4.10: Variation of strain rate with respect to tool rotational speed

4.4 Influence of welding temperature and strain rate on weld properties

The temperature data from the simulation further corroborates the DSC results and microstructural results i.e. with increasing rotational speed the material is subjected to higher temperatures results in coarsening of grains leading to greater drift in transformational temperatures. Further, drift in transformational temperatures within a weld can be attributed to variation in temperature and strain rates experienced by each region. As it was seen from the microstructures (Fig. 3.14) of welds at different tool rotational speeds, grain size of the weld varied considerably. Further, it can be assumed that the dislocation density and the residual stress of the weld at a particular tool rotational speed will be different. As phase transformational behaviour is sensitive to dislocation density, grain size and residual stress, the friction stir welded NiTi has exhibited a drift in phase transformational temperatures [2]. Due to high plastic deformation in the nugget zone, the temperature rise is comparably higher than the advancing and retreating sides [47,108]. However, the zones next to the stir zone i.e. both TMAZ and HAZ experiences low to negligible plastic deformation and lower temperatures than the stir zone. Hence during FSW, an inherent asymmetry in temperature and strain rate exits across the weld. Typically, the advancing side encounters higher temperature and strain rates than the retreating side [132]. This asymmetry in the temperature and plastic deformation across the weld regions may cause difference in dislocation density and residual stress which has led to change in phase transformation temperatures in different weld regions [117].

4.5 Summary

The peak temperature and temperature gradient existing across the weld regions have been evaluated using FEA. Since, the material flow plays the important role in FSW, the strain rate controlling the flow has been evaluated for different tool rotational speeds. The information on the temperature distribution and strain rate has given better insight in to the FSW of NiTi alloy. At the tool rotational speed of 1200 rpm, the highest peak temperature was predicted which accounts to around 83.5 % of the melting point of the NiTi alloy. Similarly, the higher strain rate of 226 s^{-1} was observed for the welding at 1200 rpm.

Chapter 5

Evaluation of smart functional Capabilities and Thermomechanical Behaviour of the Friction Stir Welded NiTi alloy

5.1 Introduction

The welding will induce changes and alter the properties in the welded region. These changes in the weld properties may affect the performance of the structures during deployment in applications. The material characterization techniques may provide information about the influence of welding on microstructure, phase transformation behaviour, mechanical properties etc. However, with respect to application perspective, it is important to evaluate the functional capabilities of the welded structure. In this chapter, functional properties such as tensile cyclic behaviour, thermomechanical actuation behaviour and damping characteristics have been investigated. The thermomechanical behaviour has been studied using two different actuation methods namely electrical and laser actuation. In addition, the influence of environmental perturbations on the thermomechanical behaviour of the welded strip has also been studied.

5.2 Sample preparation for the analysis

Since, the friction stir weld made at 1000 rpm has yielded better mechanical properties; it has been used to study the smart capabilities. The welded samples were annealed at 475^{o}C for 1 hour and then furnace cooled to room temperature. Annealing has converted the welded NiTi from superelastic state to shape memory state i.e. from austenite to martensite at room temperature. Fig. 5.1 shows the phase transformation behaviour of the welded NiTi alloy after annealing. The austenite transformation has moved above room temperature after annealing. The austenite start (A_s) and finish (A_f) phase transformation temperatures were 37ºC and 60ºC respectively.

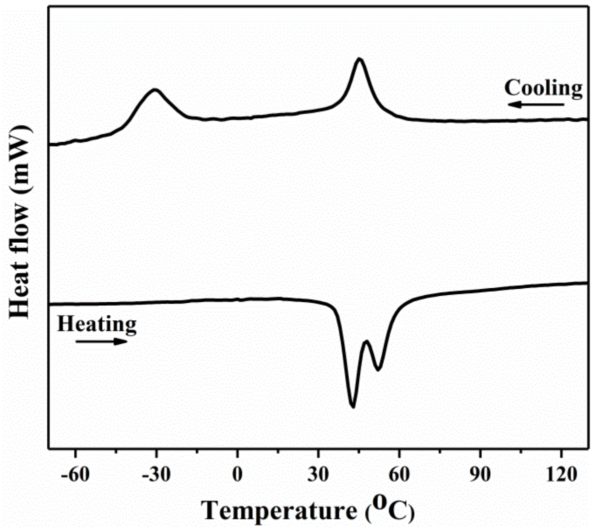

Fig. 5.1: Phase transformation behaviour of the welded NiTi after annealing

5.3 Tensile loading/unloading of the weld

Both tensile test until fracture and cycling tests were performed using the Instron-5967 at a strain rate of 10^{-3} s^{-1}. The sample of dimension 65 mm × 4 mm × 1.2 mm having weld in the centre was used for the tensile test. Fig. 5.2 shows the tensile testing plot of the weld till fracture. Average tensile strength and elongation to fracture of the weld was found to be 605 MPa and 7 % respectively. Fig. 5.3a shows the tensile cycling at 2.5 % strain. The maximum stress was around 320 MPa and the residual strain increased with number of cycles. Fig. 5.3b shows the cyclic behaviour at different strain percentages. The maximum stress was 495 MPa and 590 MPa for 3.5 % and 4.5% strain respectively. At 2.5 % strain, the weld lasted up to 7 cycles. However, the weld has failed during the second cycle for higher strain percentages.

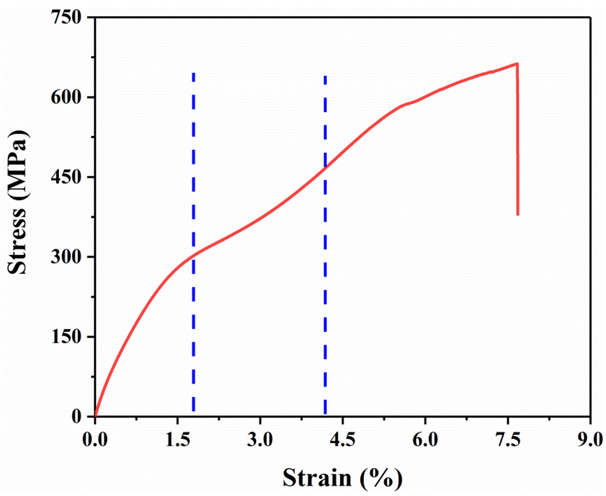

Fig. 5.2: Engineering stress-strain curve of the welded NiTi alloy

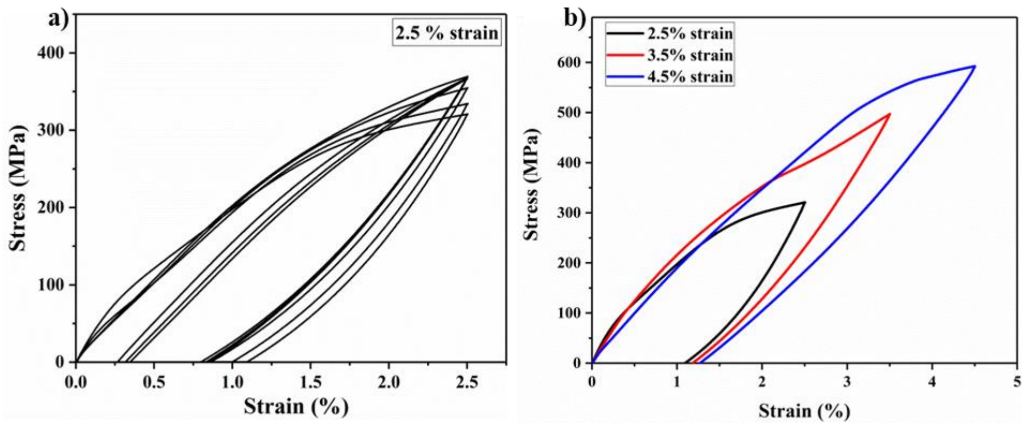

Fig. 5.3: a) Tensile cyclic test at 2.5 % strain and b) Tensile cyclic test for different strain percentages

5.4 Dynamic mechanical analysis of welded samples

The dynamic mechanical behaviour of materials can be explained easily with the theory of bouncing balls. The bouncing behaviour of balls is greatly influenced by the viscoelastic properties of the ball material. Fig. 5.4a shows the bouncing of two balls. The red ball bounces up to 80% of the dropping height. However, the black ball has lifted only up to 20% of the dropping height. The red ball possesses good elasticity and has capability to absorb kinetic energy in the form of deformation energy and gives back during bouncing. In case of black ball, the deformation energy will be liberated as heat energy [133]. Since, energy has been lost in form of heat, the black balls lacks energy to bounce back and recorded a much lower height than the red ball. The material property responsible for this type of behaviour is the modulus of elasticity or Young's modulus. It has two components viz. storage modulus describing the energy storage capacity and loss modulus relating to dissipative heat energy. The ratio between the loss modulus and the storage modulus is called loss factor (tan δ). The concept of dynamic mechanical analysis (DMA) is shown in Fig.5.4b. A sinusoidal oscillatory deformation will be applied (stress or strain) to the sample. Then the material response will be measured (strain or stress). The phase shift (δ) between the deformation and response will be used to calculate the storage and loss modulus.

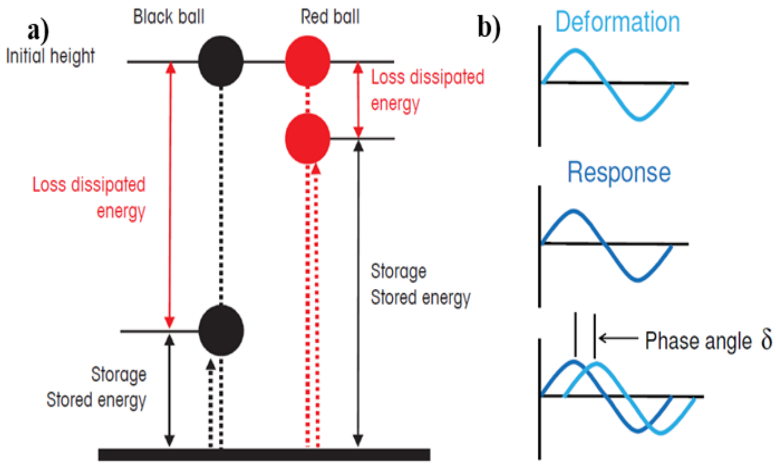

Fig. 5.4: a) Concept of loss and storage modulus and b) Dynamic mechanical analysis

The sample for DMA was cut from the centre of the weld (red colour) as shown in Fig. 5.5. The sample covers the complete FSW zone in the centre. The dimensions of the sample are 40 mm × 10 mm × 1.2 mm. The DMA analysis was performed in a 3 point bending mode using Perkin Elmer 8000 machine. The testing was done from room temperature 32ºC to 120ºC at three different frequencies 1 Hz, 10 Hz and 20 Hz. The stress amplitude was 1.5 N with a strain of 0.05 mm. The experiments were carried out in temperature sweep mode while keeping the frequency and the amplitude of deformation as constant.

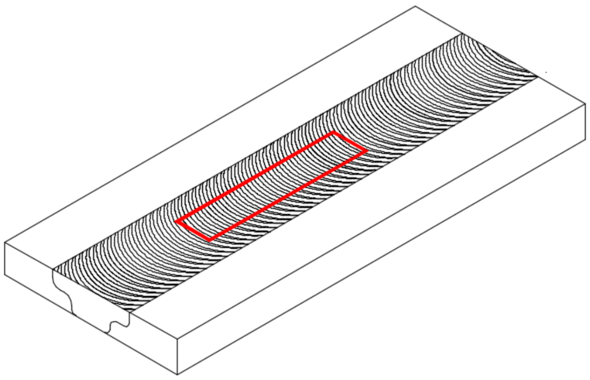

Fig. 5.5: Schematic showing sample location from the weld

The DMA of the welded sample has been compared with the base metal. The DMA of sample at 10 Hz is shown in Fig. 5.6. Before the evolution of peak, stable martensite will be present. The increase in temperature initiates the evolution of peak due to the transformation of martensite to austenite. At the highest point in peak, the combination of two phases will be present. After reaching the A_f temperature, the peak completes and beyond which complete austenite will be present. This peak represents the loss of energy in the form of heat. The sample after welding has showed damping ability as clearly seen from the Fig. 5.6b. However, the hysteresis of the peak has been reduced after welding. The hysteresis of the storage modulus and tan δ lies in the temperature range as depicted in the DSC curve Fig. 5.1. The sample has demonstrated damping capabilities at all the tested frequencies as shown in Fig. 5.7 and 5.8. The storage modulus and the damping capacity at room temperature have been plotted as the function of frequency in Fig.5.9. The storage modulus decreases while the damping capability increases with the increase in frequency. Irrespective of the frequency, the damping ability of the weld at room temperature was lesser than the base metal. The reduced damping ability of the weld could be attributed to changes in micro defect density, dislocation density etc. after welding [134–137].

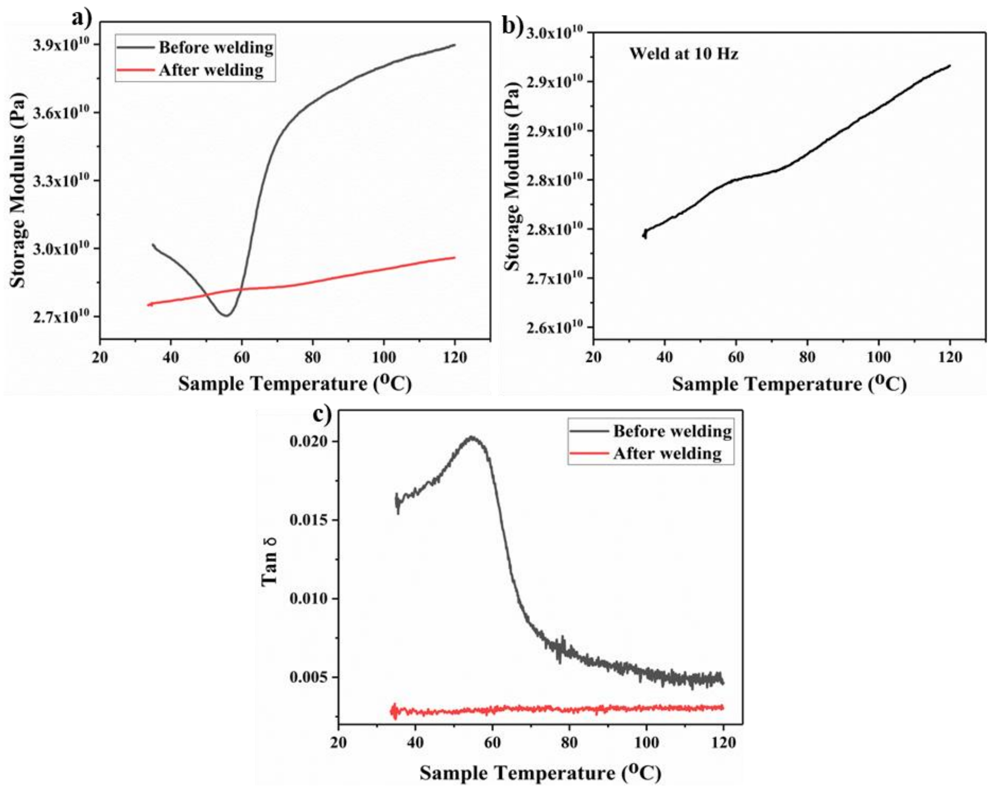

Fig. 5.6: a) Storage modulus at 10 Hz, b) Storage modulus of the weld and c) Damping capacity at 10 Hz

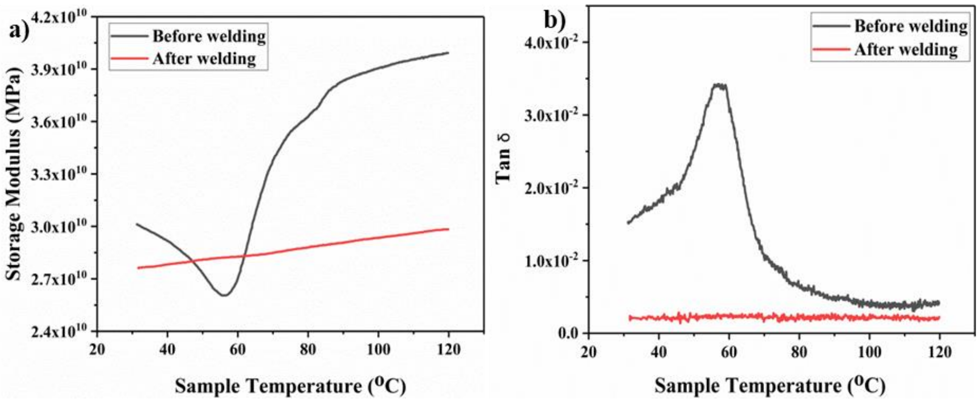

Fig. 5.7: a) Storage modulus and b) Damping capacity at 1 Hz

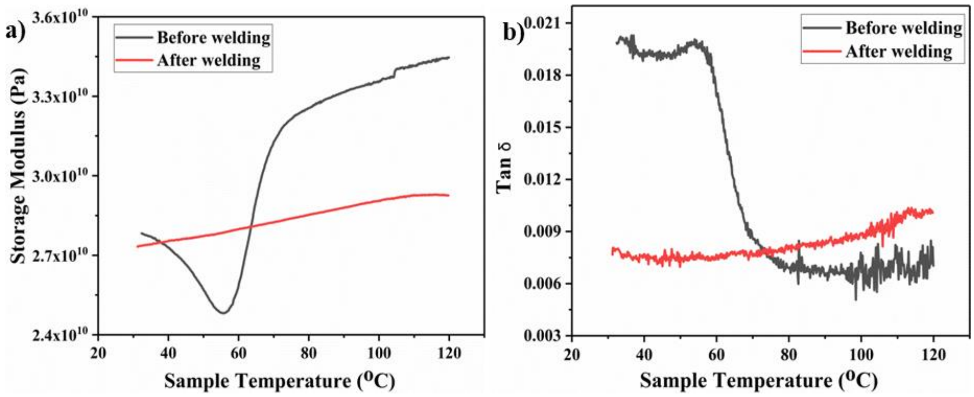

Fig. 5.8: a) Storage modulus and b) Damping capacity at 20 Hz

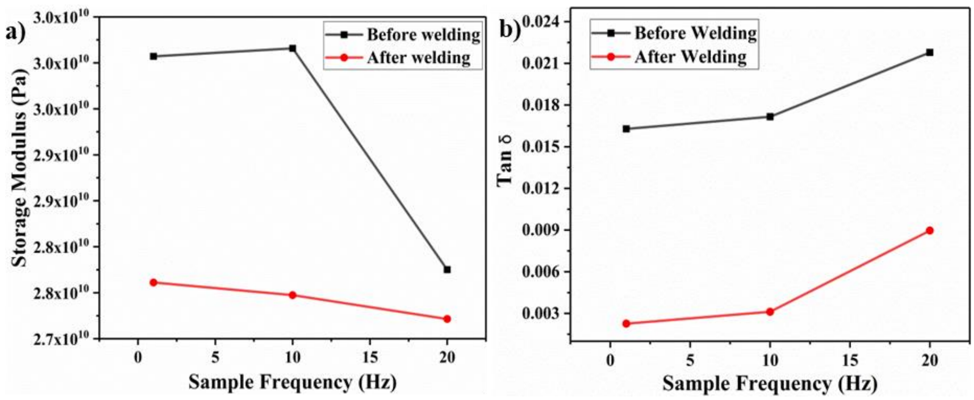

Fig. 5.9: a) Storage modulus and b) Damping capacity of the sample at room temperature

5.5 Hot plate actuation of the welded structure

A strip of dimension 65 mm × 2 mm ×1.2 mm was cut across the weld and used for hot plate actuation. The same type of sample has been used for studying the thermomechanical behaviour through electrical actuation (Joule heating) and laser actuation. Since the sample was annealed at 475^{o}C in a straight position after welding, the flat shape becomes the trained shape of the sample. The sample used for actuation studies is shown in Fig. 5.10. Strain was imposed in the welded sample to bend in a U shape. The bending was performed inside the ice bath which ensures martensite state during bending. After bending, the sample was actuated on a hot plate held at 65°C or 75°C. These temperatures were chosen as it was above the austenite finish temperature of the sample. The sample was not disturbed until imposed strain was completely recovered.

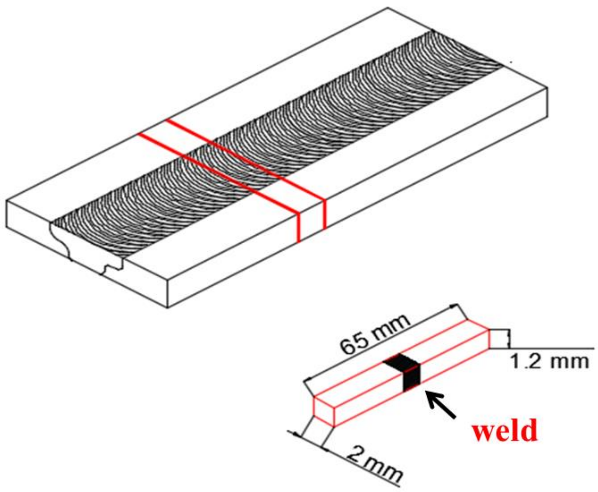

Fig. 5.10: Schematic of the sample used for actuation studies

The snapshots during strain recovery are shown in Fig. 5.11. The load applied for bending will convert the sample from twinned martensite into detwinned martensite. On heating, austenite transformation starts and the sample will return to initial straight position.

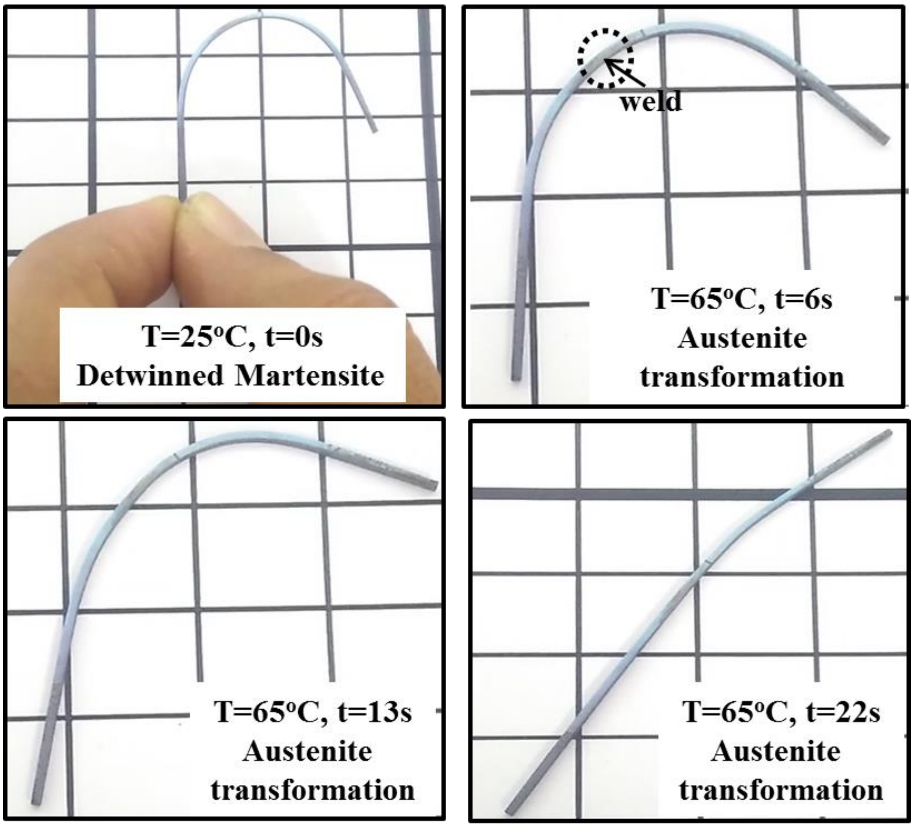

Fig. 5.11: Photographs of the sample during hot plate actuation

The actuation was quantified using recovery angle, which is the angle between two tangents drawn 5 mm from the weld centre on either side. The schematic of angle measurement and recovery angle vs time plot are shown in Fig. 5.12. The recovery angle was measured using the AutoCAD software from the images acquired during actuation. The method of angle measurement was similar to the method reported by J. P. Oliveira et al. [75]. When the hot plate was maintained at 65°C, the duration for complete strain recovery was noted to be 27 seconds. However, the hot plate at 75°C has reduced the recovery time to 13 s due to higher heating rate experienced by the sample.

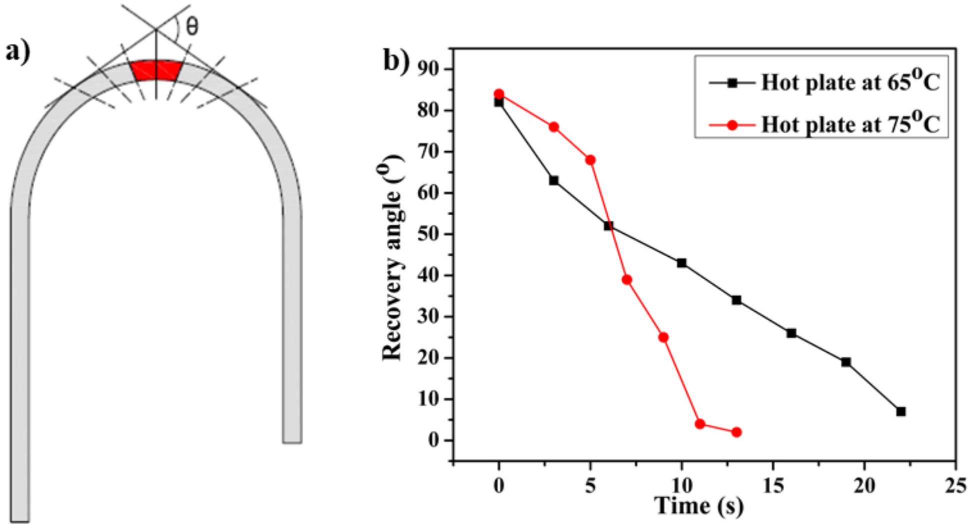

Fig. 5.12: a) Schematic of angle measurement and b) recovery angle as a function of time

5.6 Thermomechanical behaviour of welded structure using electrical actuation

5.6.1 Thermomechanical behaviour setup

The sample was mounted in the cantilever configuration with the bias load (50 g or 100 g) attached to the free end (Fig. 5.13). Before mounting in the cantilever configuration, the sample possess twinned martensite phase at room temperature. The application of bias load to the free end of the sample will apply deformation force and transform the sample to detwinned martensite phase. The minimum and maximum stress required to deform the material is called de-twinning start stress (σ_S) and de-twinning finish stress (σ_f) respectively.

Upon supply of electricity, the temperature of the sample increases above the austenite start temperature due to Joule heating. This temperature rise enables the solid state phase transformation of sample from detwinned martensite to high temperature austenite phase. Due to the phase change, the sample lifts up against the bias load. After a particular heating time, the electricity was cut off which in turn set the cooling of the sample. During cooling, the phase transformation from austenite to twinned martensite happens. Simultaneously, the bias load lowers down the sample and thereby induces detwinning martensite phase in the sample. Thus, the thermomechanical setup helps in understanding the cyclic behaviour of the welded sample.

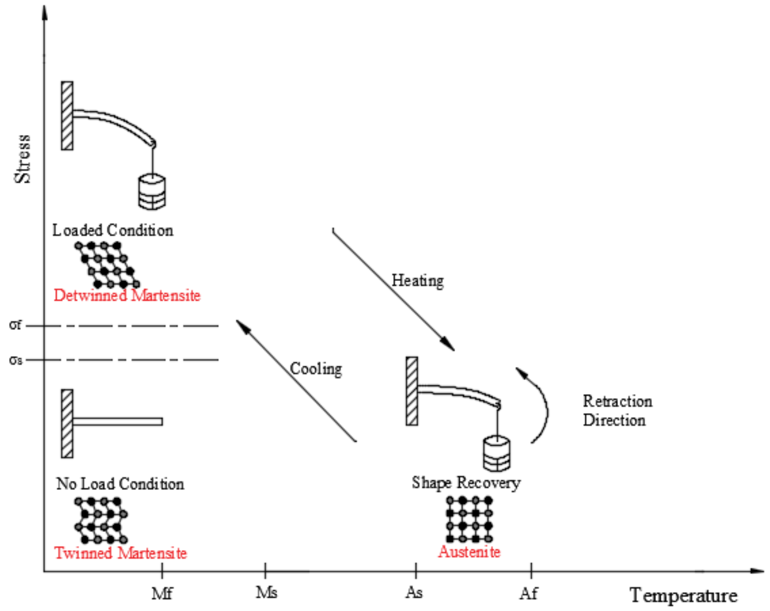

Fig. 5.13: Schematic showing the thermo-mechanical actuation of welded strip

The electricity required for actuation was supplied using a programmable power supply. The change in displacement during electrical stimulation (Joule heating) was measured using laser displacement sensor (LDS). The LDS data was logged using data acquisition system and a computer. Fig. 5.14 shows the sample configuration and components used for thermomechanical setup.

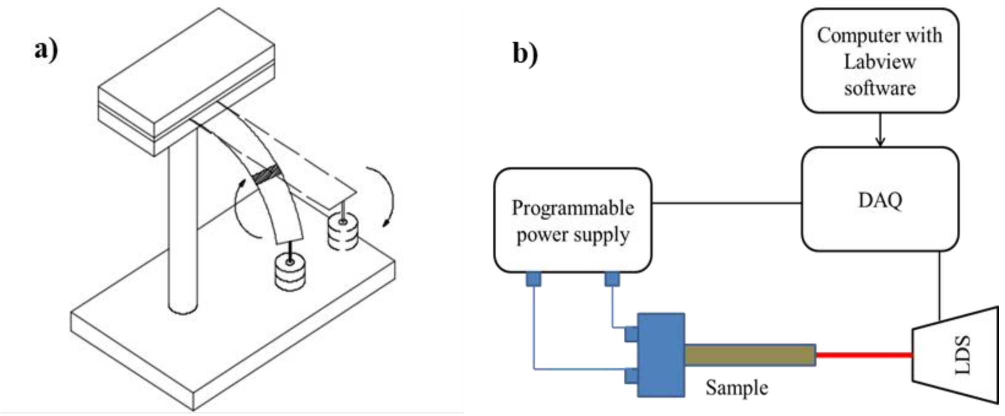

Fig. 5.14: a) Schematic of sample configuration used for thermomechanical behaviour and b) Schematic representation of the components used for thermomechanical behaviour

5.6.2 Influence of current on actuation behaviour

In case of electrical actuation i.e. Joule heating, the current is the key factor determining the heat generation. Here, the voltage was kept constant at 14 V and the current has been varied to study the thermomechanical behaviour. The current less than 3 A were unable to actuate the sample against the load. Also, the current above 5 A has created fumes/sparks in the crocodile clip connection to the sample. So, the optimum current values in the range 3-5 A have been used for the actuation. For each current value, three different heating times has been selected. The actual photograph of the sample with the bias load and thermal image during actuation is shown in Fig. 5.15. The temperature during actuation was evaluated using thermography camera (FLIR ONE thermal imager).

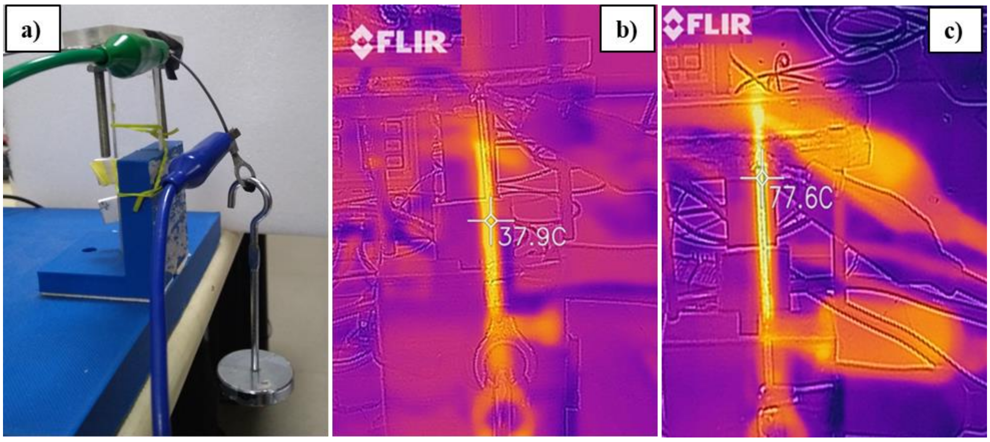

Fig. 5.15: a) Actual photograph of the sample with bias load and b-c) Thermal image during actuation at 3 A and 5 A respectively.

The displacement change during actuation was plotted as the displacement vs time graph for different current, heating time and cooling time (Fig. 5.16). The heating cycle enables increase in displacement with respect to time. The input current determines the maximum displacement and the rate of displacement of the sample against the bias load. When the electric supply is switched off, the cooling cycle initiates and the displacement begins to drop due to heat loss to the surrounding. On reaching the initial positon, the electric supply will be powered again to initiate the subsequent cycles. The higher current provides high heating rates and the effect is clearly reflecting in the heating curve i.e. the heating curve of 4 A and 5 A is almost straight. However, the heating cycles at 3 A displayed increase in displacement with positive slope. The displacement against the bias load 50 g was higher than the displacements against 100 g for all the actuation conditions.

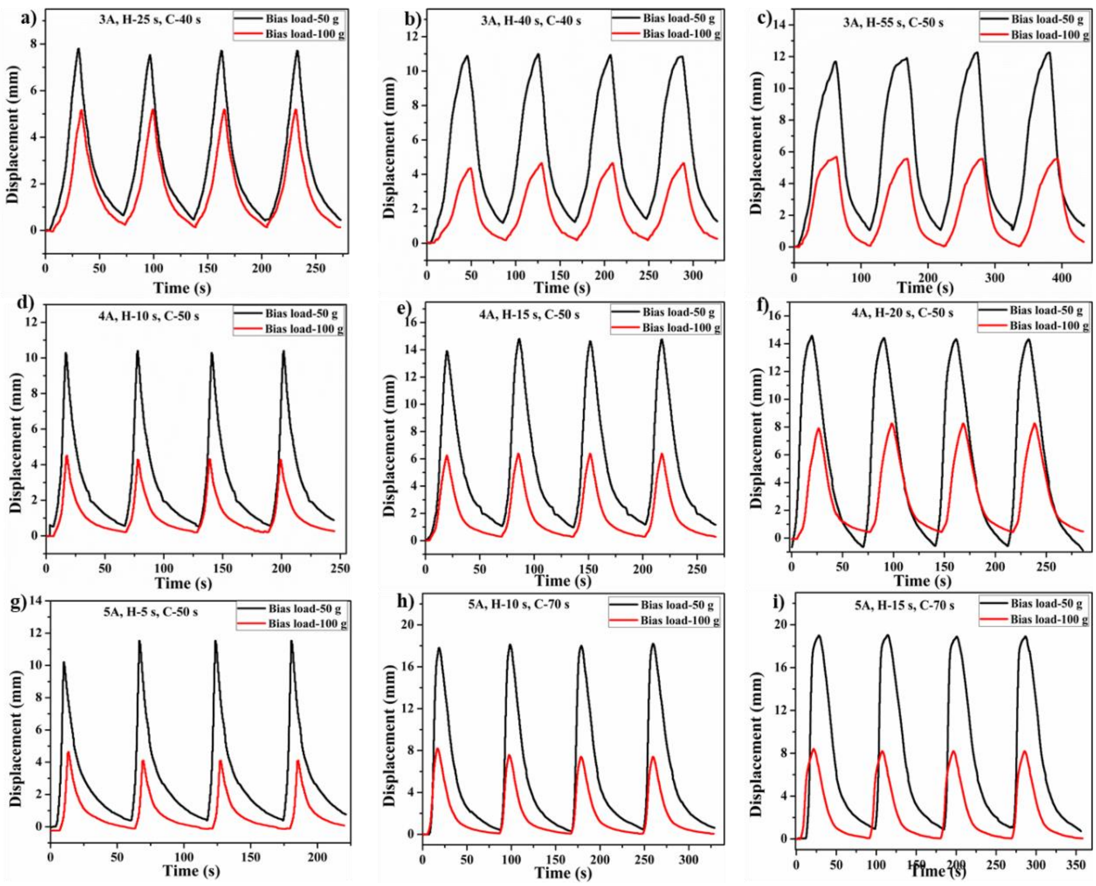

Fig. 5.16: a-i) Time vs. displacement graph during actuation at different currents

The comparison plot showing the maximum displacement, actuation speed and maximum temperature at different current is shown in Fig. 5.17. The actuation at higher currents has recorded higher displacements in a short period of time. A maximum displacement of 10.9 mm, 14.7 mm and 17.8 mm were attained for 3 A, 4 A and 5 A respectively. The maximum temperatures at actuation current of 3 A, 4 A and 5 A were 37.9^{o}C, 56.5^{o}C and 77.6^{o}C respectively. These actuation temperatures corroborate with the phase transformation temperature range as seen from the heating curve of the DSC plot (Fig. 5.1). The actuation speed is a crucial parameter defining the agility of an actuator. The actuation speed is the ratio of the displacement recovered to the heating time. The higher currents have recorded higher actuation speeds during actuation.

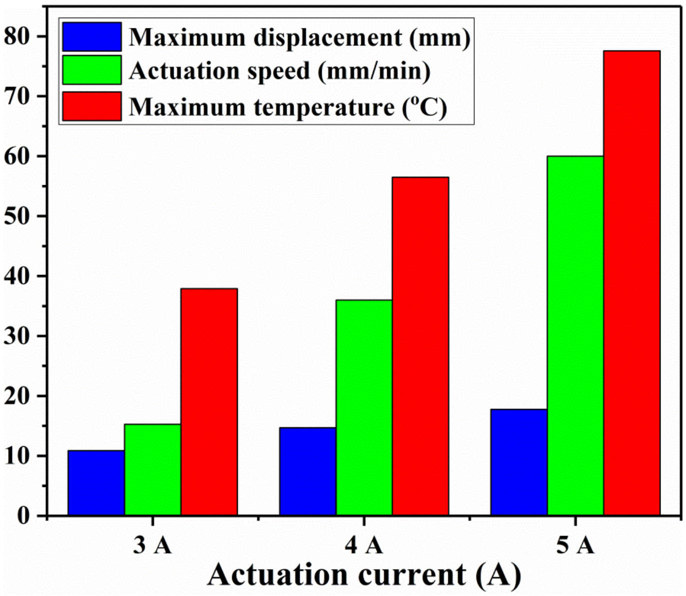

Fig. 5.17: Maximum displacement, speed of actuation and maximum temperature during electrical actuation

The high speed camera images during actuation at 5 A different time frames are shown in Fig. 5.18. It clearly depicts the lifting up of the welded sample against the load during electrical actuation.

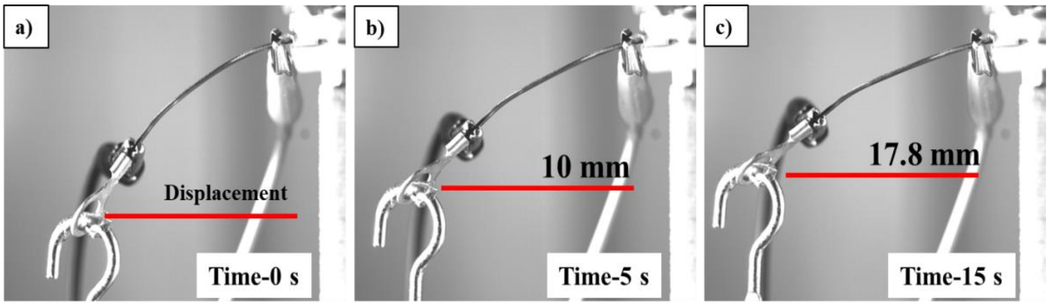

Fig. 5.18: Images taken using high speed camera (Photron fastcam miniux) during actuation at 5 A

5.6.3 Life cycle behaviour of the weld

The life cycles were performed at 5 A actuation current with a heating and cooling time of 5 s and 15 s respectively. The analysis was conducted up to 300 cycles and the samples didn't show any sign of failure. There was no significant reduction in displacements over the increase in the number of cycles. This ensured the quality of the weld during actuation against the bias loads in cantilever configuration.

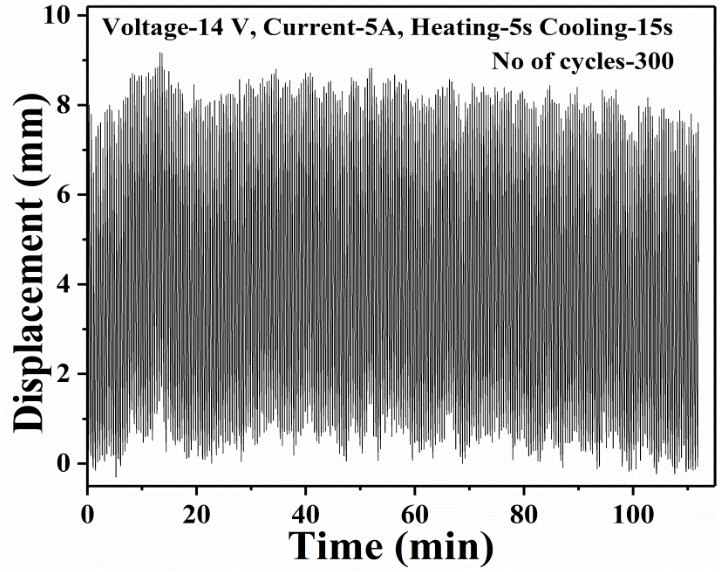

Fig. 5.19: Life cycle behaviour of friction stir welded NiTi through electrical actuation

5.6.4 Influence of perturbations on the actuation behaviour of the SMA structure

The actuation of the shape memory alloy structure depends upon various factors such as phase transformation temperatures, medium or method of actuation (hot water, oil, electrical or laser), ambient temperature, air flow etc. The understanding of actuation behaviour i.e. the power requirement, frequency of actuation etc. with respect to environmental perturbations is crucial for practical actuator applications. However, to the best of our knowledge, the influence of environmental disturbances such as ambient temperature and air flow velocity on the shape memory effect was not explored yet. In this study, an attempt has been made to evaluate the influence of ambient temperature and air flow velocity on the actuation characteristics of welded nitinol SMA. Using finite element method (FEM), the influence of environmental perturbation on the actuation characteristics of welded nitinol has been simulated. The change in actuation characteristics with respect to ambient temperature and air flow velocity is described in detail.

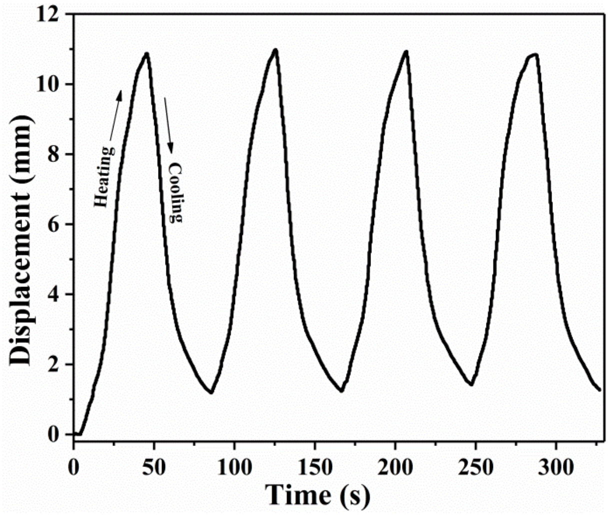

Fig. 5.20: Heating and cooling cycles during electrical actuation at 3 A

Fig. 5.20 shows the displacement of the SMA strip during heating and cooling cycles. A maximum displacement of 10.9 mm was attained at a current of 3 A against the 50 g bias load. The simulation was done to get the maximum temperature of 40^{o}C with variation in current against the environmental perturbations. Comsol Multiphysics 4.3a was used for simulating the mentioned conditions. The governing equations of the FEM are given in the following.

The heat generation in the sample during electricity supply is given by,

$$J = \sigma E \qquad (1)$$

$$E = - \nabla V \qquad (2)$$

Where J - Current Density, E - Electric Field, V- Electric potential.

The heat transfer due to conduction and convection is given by,

$$\rho C_p u.\nabla T + \nabla.q = \mathrm{Q} \qquad (3)$$

$$q = - k \nabla T \qquad (4)$$

$$Q = h_c A dT \qquad (5)$$

Where ρ-density of the sample, C_p-specific heat, u-velocity of flow, k-thermal conductivity, A-exposed surface area and h_c-convective coefficient.

The Navier-Stokes and continuity equation governing the fluid motion is given by,

$$\rho(u.\nabla)u = \nabla.[-pI + \mu(\nabla u+(\nabla u)^T)] + F \quad (6)$$

$$\rho \nabla.(u) = 0 \quad (7)$$

Where u- fluid velocity, p-pressure applied to the fluid, ρ-density of fluid, I-identity matrix, F-external force and μ-dynamic viscosity of fluid.

The meshed model of the sample and the flow domain is shown in Fig. 5.21a. The model was solved for the required actuation temperature against the variation in ambient temperature and airflow velocity. The temperature distribution of the sample and the effect of perturbations are shown in Fig. 5.21b and 5.22. A linear relationship between the required current against ambient temperature and air flow velocity was observed. The decrease in temperature has linearly increased the required current for actuation. Highest current of 6.9 A was required to get the actuation temperature at -5^{o}C ambient temperature. In case of higher air flow of 15 m/s, the sample needs 6.8 A to actuate. The decrease in ambient temperature or increase in airflow velocity leads to increase in heat transfer from the sample. Due to the increased heat transfer from the sample, the sample drains more electrical energy for actuation.

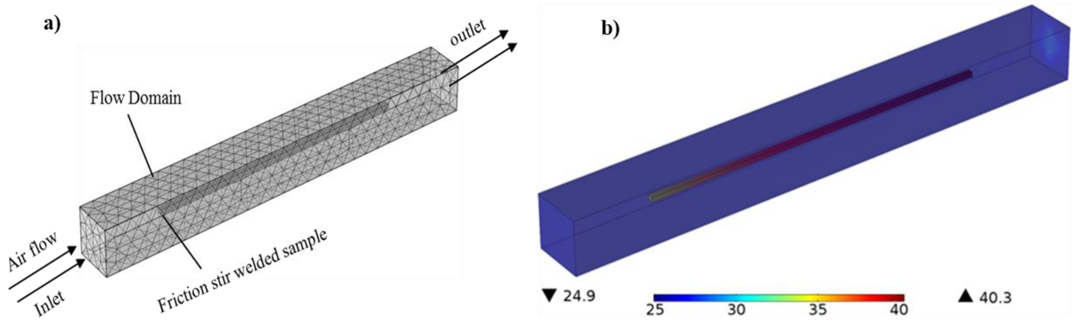

Fig. 5.21: a) Meshed model used for the simulation and b) Temperature distribution during heating cycle

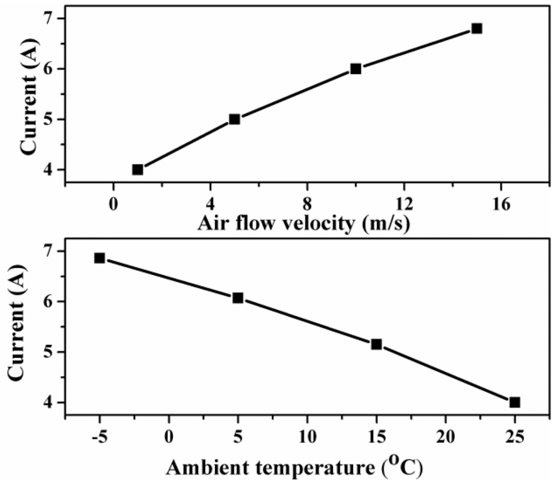

Fig. 5.22: Influence of flow velocity and ambient temperature on the actuation behaviour

5.7 Thermomechanical behaviour of welded structure using laser actuation

Based on the preliminary experiments mentioned in chapter 2, the laser actuation of the welded sample has been carried out. The details of laser, the scanning method and other details about the actuation methodology can be found in the section 2.6. The thermomechanical setup given in Fig. 5.13 remains the same along with laser beam acting as the heating source for actuation. The schematic of the laser actuation is given in Fig. 5.23. The laser powers in the range 10 to 50 W was used for actuation of the sample loaded with bias loads 50 g or 100 g. The number of passes required for actuation at different laser power varies. The number of passes for different power was selected based on the saturation of displacement at particular pass. For example, at laser power 10 W against the bias load 50 g, 13 passes were required for actuation i.e. even if the number of passes were increased above 13, the displacement remains constant. Fig. 5.24 shows the actual photograph of the sample before actuation and thermal images during actuation.

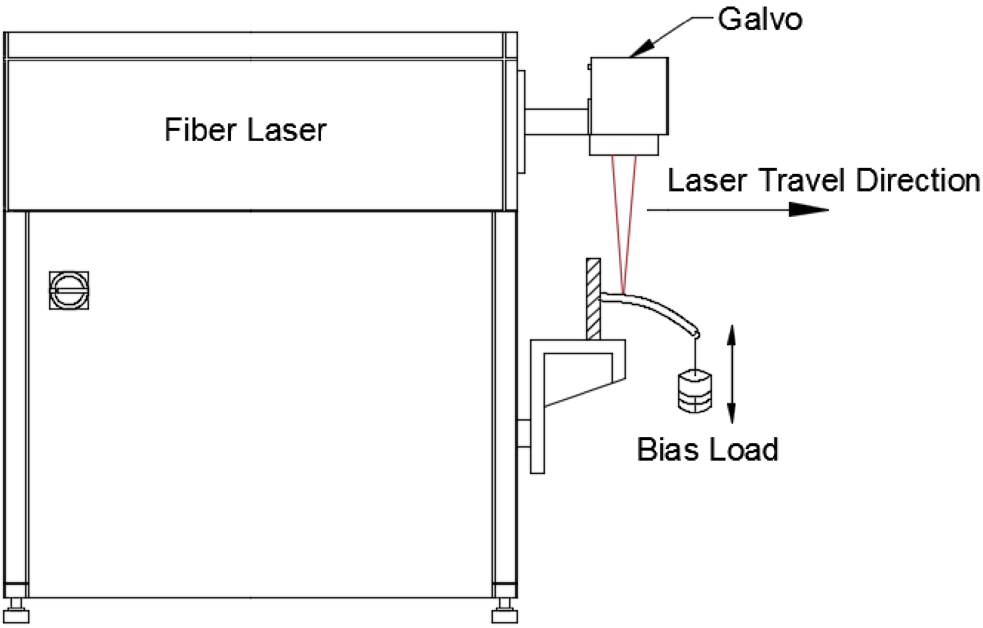

Fig. 5.23: Schematic of the experimental setup used for the laser actuation of welded NiTi alloy

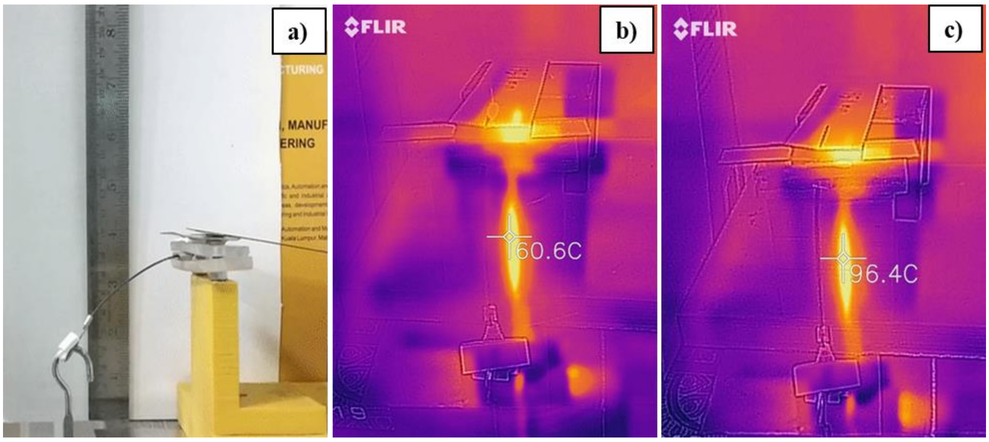

Fig. 5.24: a) Actual photograph of the sample before actuation, b-c) Thermal image of the sample during laser actuation at 20 W and 40 W respectively

The maximum displacement, required number of passes and time of actuation against the laser power is given in Fig. 5.25. In case of 50 g bias load, the minimum and maximum displacements were 20 mm and 28 mm for laser power 10 W and above 20 W respectively. As seen from the Fig. 5.25a, the displacement above specific power has been saturated. The displacement was saturated at 28 mm and 20 mm against 50 g and 100 g bias loads respectively. However, the number of passes and heating time required to attain the maximum displacement at particular laser power differs. So, in order to need to attain 28 mm displacement in a short time, then the higher power 50 W will be preferred. The minimum and maximum number of passes required for actuation was 3 and 15 for laser power 50 W and 10 W respectively (against 100 g bias load). The heating time i.e. time required for actuation has followed the same trend as of required number of passes. The minimum and maximum time required for actuation was 4.5 s and 22.3 s for laser power 50 W and 10 W respectively (against 100 g bias load).

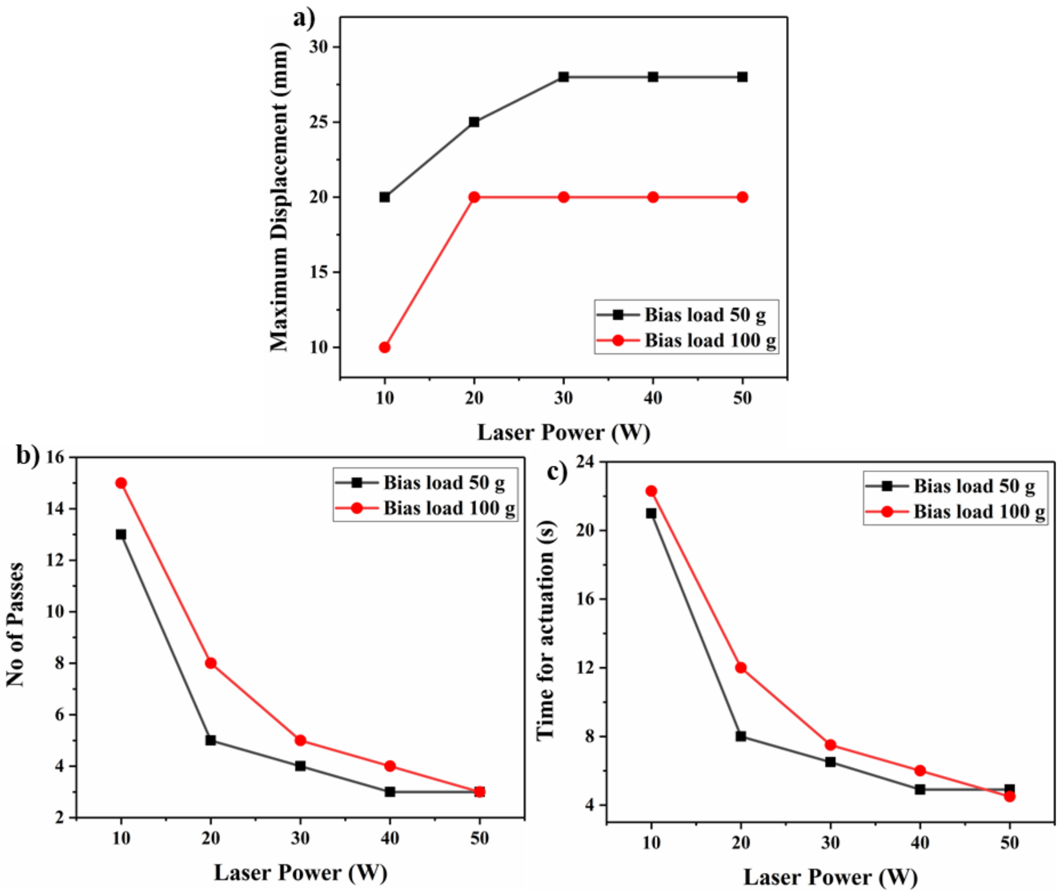

Fig. 5.25: a) Maximum displacement during laser actuation, b) Required number of passes for actuation at different powers and c) Time required for actuation at different laser powers

The comparison between the actuation speeds of electrical and laser actuation is shown in Fig. 5.26a. The laser actuation at 50 W against 50 g bias load has recorded the highest actuation speed of 342 mm/min. The laser actuation speeds were higher than the electrical actuation speeds due to the associated higher actuation temperatures experienced by the sample as shown in Fig.5.26b. The laser actuation is highly impulsive than the electrical actuation and the rate of heat generation is higher than the electrical actuation. Overall, the laser actuation has yielded better actuation characteristics compared to electrical actuation. Few shortcomings of the laser actuation are viz. i) Due to laser scanning, the laser spot moves along the length of the sample which have led to a jerky behaviour during lifting up against the bias load i.e. heat distribution or temperature in a particular region of the sample at an instant varies and ii) In case of laser actuation of strip (Fig. 5.23), the focal point of the laser spot changes during the lifting up of the sample i.e. region near to holder is at higher height than the region near the bias load. So, during scanning variation in heat generation might happen. Fig. 5.27 shows the high speed camera images taken during laser actuation at 50 W. The movement of laser beam is clearly visible in Fig. 5.27a-b. The impulsive nature of the laser actuation is clearly visible from the time frames of the images.

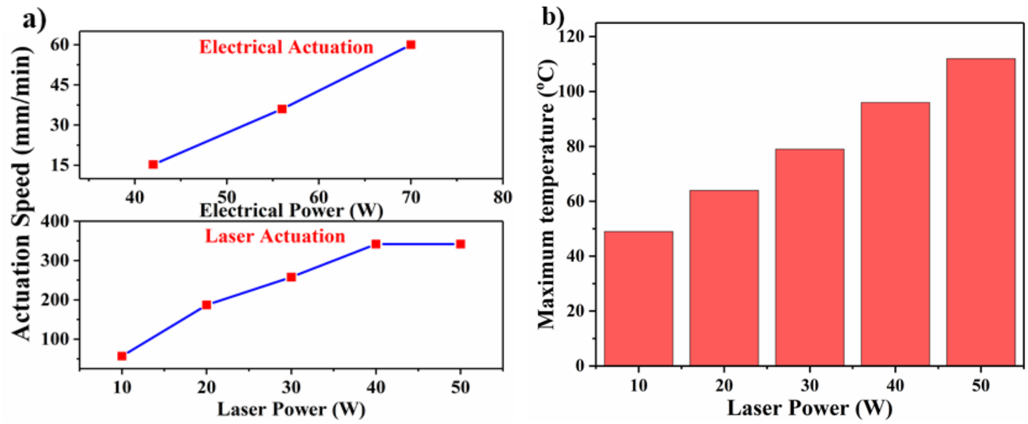

Fig. 5.26: a) Comparison of actuation speeds during electrical and laser actuation and b) Maximum temperature during laser actuation

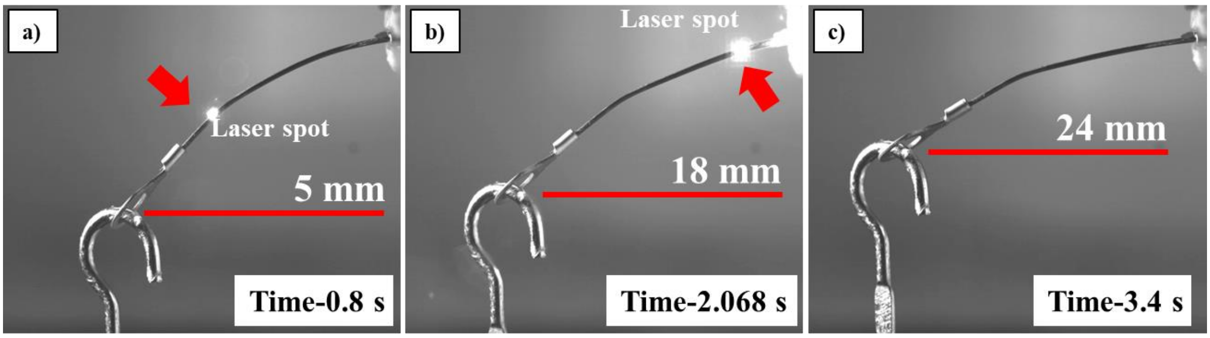

Fig. 5.27. High speed camera images during laser actuation at 50 W

5.8 Summary

The functional capabilities such as tensile cycling, damping properties and thermomechanical behaviour of the welded NiTi alloy have been investigated. The damping properties were retained after welding with reduced hysteresis compared to base metal. The actuation ability of the welded strip has been evaluated using bending-recovery method. The bended sample was able to recovery the imposed strain in short period of time. In case of all the actuation methodologies (hot plate, electrical and laser), the heating rate and the resultant temperature plays the important role in the actuation behaviour of the NiTi alloy. With respect to the actuation methods, the influence of critical parameter on the actuation behaviour has been explored in detail. The laser actuation using the scanning method has shown higher displacements due to the associated the higher temperatures during actuation.

Chapter 6

Investigations on the Corrosion Characteristics of Friction Stir Welded NiTi Alloy using Electrochemical Corrosion Testing

6.1Introduction

Besides the bulk mechanical properties, the surface characteristics play a significant role in deciding the applicability and performance of the material. Welding significantly affects the corrosion resistance of a material due to the changes in microstructure, distribution of inclusions, residual stress etc. NiTi SMA is employed in corrosion prone areas such as bio medical (physiological environment) and offshore oil/drilling fields (sea water or fracking fluid environment) [10,138]. Hence, it is extremely important to understand the corrosion behaviour of the welded NiTi to ensure stability and longevity of the structure. In this chapter, the electrochemical corrosion testing of welded NiTi alloy at different tool rotational speeds are discussed in detail.

6.2 Electrochemical corrosion testing

The samples of dimension 10 mm × 10 mm × 1.2 mm has been cut using wire electrical discharge machine from the weld zone of friction stir welded NiTi alloy at 1200 rpm. The sample was polished using SiC papers of various grades up to 1200 grit to remove flash or unwanted protrusion formed during welding. Both base metal and FSW samples were degreased in ethanol in an ultrasonic cleaner for 15 min. Then the samples were cleaned with distilled water and dried. Electrochemical measurements were carried out using GillAC potentiostat supplied by ACM instruments. The three electrode method was used where platinum acts as the counter electrode, Ag/AgCl (3 mol/1 KCl) as reference electrode and the NiTi samples as the working electrode. 3.5 wt % NaCl in de-ionized water was used as the test electrolyte. The schematic of the electrochemical corrosion testing is shown in Fig.

6.1. To evaluate the stability of the potential in the open circuit condition, each sample was immersed in the electrolyte for a period of 24 hours. Then electrochemical impedance spectroscopy (EIS) was measured in the frequency range of 10^4 Hz to 0.1 Hz with the sinusoidal amplitude of ±10 mV. The first scan was performed at 5th minute, followed by consecutive scans till 24 hours (1st, 3rd, 6th, 12th, 18th and 24th hour). The EIS spectra was modelled with electrochemical equivalent circuits (EEC) and fitted with the complex non-linear least square method using Zview^{TM} software to analyze the impedance behaviour. Finally, the potentiodynamic scan was done at a scan rate of 1 mV/s in the range from -300 mV to 3000 mV with respect to OCP.

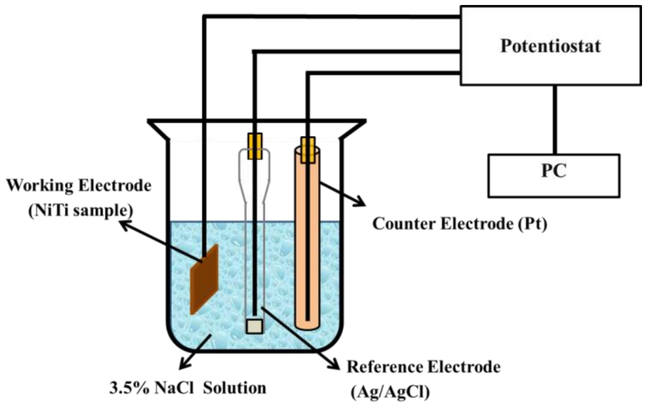

Fig. 6.1: Schematic of three electrode electrochemical setup used for corrosion testing

6.3Electrochemical corrosion test on welded NiTi and base material

6.3.1 Open circuit potential (OCP)

OCP of base metal and welded samples as the function of time over a period of 24 hours is shown in Fig. 6.2. On immersion of the NiTi surface in the electrolyte, the aggressive chloride ions (Cl^-) break the original thin oxide layer and attack the Ni-Ti bonds. This process will release Ni ions into the aqueous NaCl solution leading to localized decrease in Ni concentration. Consequently, the Ti in the Ni depleted region reacts with the dissolved oxygen and passivates with the corrosion products in the pitting sites i.e. the formation of characteristic oxide film mainly consisting of TiO_2 along with other Ti oxides such as TiO and Ti_2O_3 [139,140]. After an initial transient period (fluctuations due to pitting at the defect sites), the OCP reaches a stable value (formation of uniform oxide layer retards the corrosion process) and the longer immersion experienced a negligible change in OCP values. The saturation of OCP implies a steady state condition driven by dynamic equilibrium between formation of oxide film and repetitive dissolution of Ni ions. Initially, the OCP shows an increase trend for both samples. Then the OCP tends to decrease for a shorter time and notably the base metal experienced a steeper change before saturation.

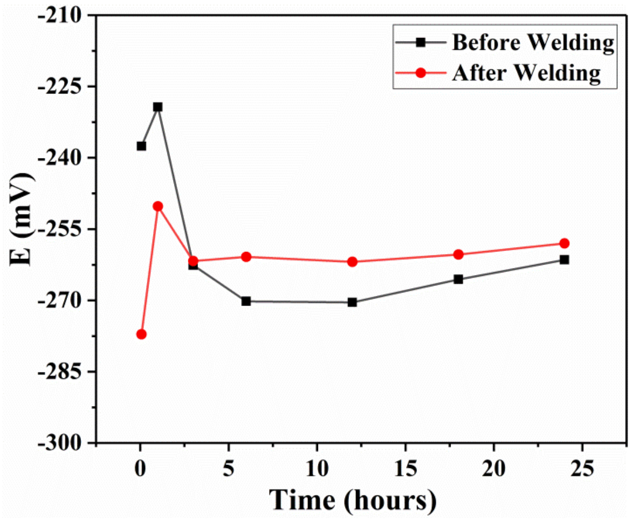

Fig. 6.2: Evolution of open circuit potential with respect to time for before and after welding

6.3.2 Electrochemical impedance spectroscopy

To assess temporal electrochemical response of before and after welding of NiTi alloys comprehensively, electrochemical impedance spectroscopy measurements were carried out in 3.5 wt.% NaCl solution as a function of immersion duration. The Nyquist, Bode impedance modulus, and Bode phase angle plot are shown in Fig. 6.3, Fig. 6.4, and Fig. 6.5 respectively.

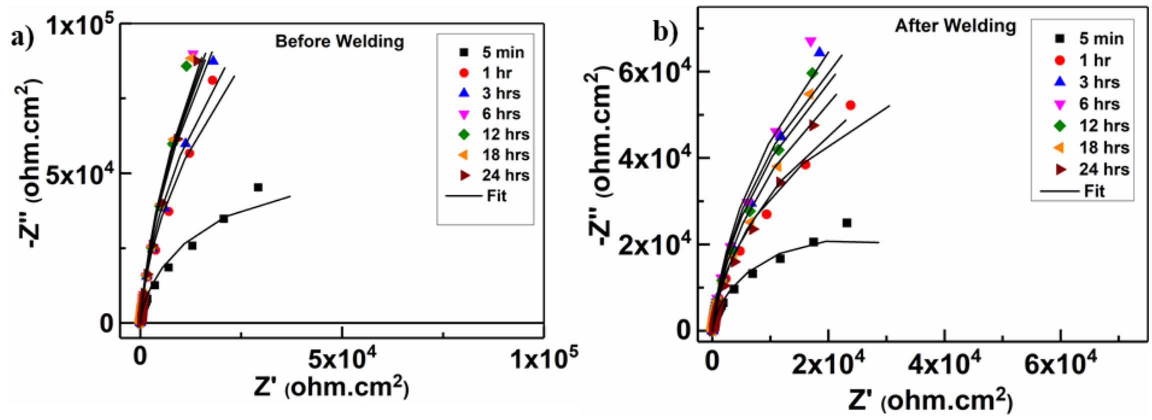

Fig. 6.3: Nyquist plot as a function of immersion duration in the 3.5 wt. % NaCl solution for a) Before welding and b) After welding

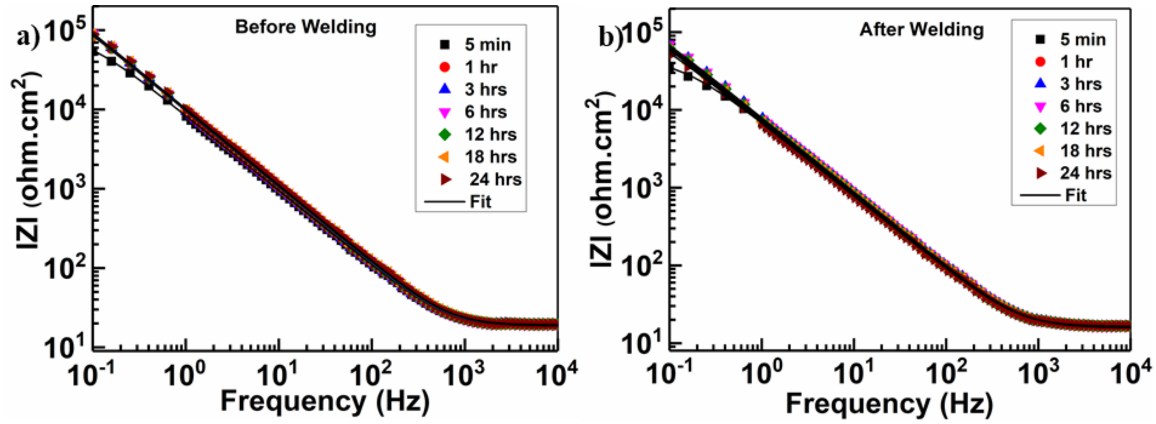

Fig. 6.4: Bode impedance modulus plot as a function of immersion duration in the 3.5 wt. % NaCl solution for a) Before welding and b) After welding

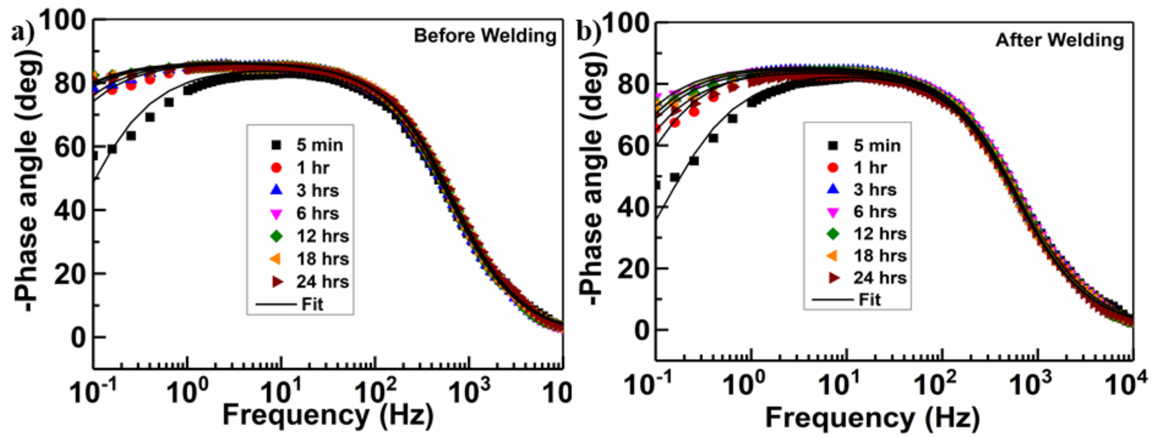

Fig. 6.5: Bode phase angle plot as a function of immersion duration in the 3.5 wt. % NaCl solution for a) Before welding and b) After welding

To account for depression of Nyquist plots caused by electrode inhomogeneity constant phase element (CPE) is used instead of a pure capacitor and is mathematically expressed as

$$Z_{CPE} = \frac{1}{T(j\omega)^{\alpha}} \quad ; -1 \leq \alpha \leq 1 \qquad (6.1)$$

Where T, α, j, and ω represents the CPE coefficient, CPE index, complex unit to define an imaginary number (and is given by $j = \sqrt{-1}$) and angular frequency (which is related to frequency, f, as $\omega = 2\pi f$) respectively.

The various elements in proposed EEC (Fig. 6.6) are the R_s represents the corrosive electrolyte resistance; $CPE_{(Ox)}$ represents the capacitance of oxide thin film layer; $R_{(OX)}$ represents the resistance of oxide thin film layer. Table. 6.1 shows the EEC elements' value extracted from EIS spectra fitting for the base metal and welded NiTi alloy. The chi-square (χ^2) value in the order of 10^{-3} shows good agreement of simulation data with the experiment for all the samples. It is evident that for all the sample the magnitude of $R_{(ox)}$ is significantly larger. For base metal, the magnitude of $R_{(ox)}$ for initial 5 minutes and final 24 hours immersion was 94102 Ωcm^2 and 683290 Ωcm^2 respectively. The welded NiTi shows lower magnitude of $R_{(ox)}$ for initial and final immersion duration with 46564 Ωcm^2 and 157790 Ωcm^2 suggesting less protectiveness of oxide layer as compared to base metal.

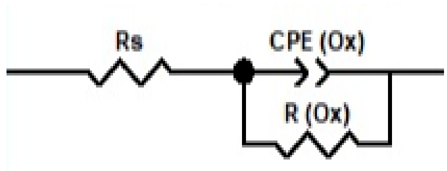

Fig. 6.6: Equivalent circuit for the corrosion behaviour of NiTi alloy in 3.5 % NaCl solution

Table 6.1: Electrical parameters obtained from the equivalent circuit diagram for the impedance spectra of before welding and after welding NiTi alloy as a function of immersion duration in 3.5% NaCl solution

Description	Samples/ EC parameters	R_s	$CPE_{(OX)}$-T	$CPE_{(OX)}$-α	$R_{(Ox)}$	χ^2 - Value
	Units	Ωcm^2	$\Omega^{-1} cm^{-2} s^{\alpha}$	-	Ωcm^2	-
Before welding	5 min	18.58	2.0826E-5	0.94717	94102	0.0027498
	1 hr.	18.91	1.7618E-5	0.96347	395450	0.0023517
	3 hrs.	19.01	1.7374E-5	0.96607	469350	0.0024505
	6 hrs.	19.07	1.7288E-5	0.96543	705460	0.002624
	12 hrs.	19.07	1.7182E-5	0.96326	799930	0.0024082
	18 hrs.	19.01	1.6863E-5	0.96357	762750	0.0023625
	24 hrs.	19	1.6678E-5	0.96258	683290	0.0022723
After welding	5 min	15.69	2.5675E-5	0.93604	46564	0.0027313
	1 hr.	16.13	2.2367E-5	0.95557	135720	0.002013
	3 hrs.	16.21	2.184E-5	0.95617	254970	0.0017427
	6 hrs.	16.23	2.211E-5	0.95709	292090	0.001992
	12 hrs.	16.32	2.334E-5	0.95334	236770	0.0018445
	18 hrs.	16.24	2.4718E-5	0.94726	205670	0.0018059
	24 hrs.	16.27	2.6108E-5	0.94074	157790	0.0018286

6.3.3 Potentiodynamic polarization curve

Potentiodynamic polarization measurements were conducted to understand the passivation tendency and overall corrosion characteristics of the NiTi samples in 3.5 % NaCl solution. The potentiodynamic polarization curves and the extracted electrochemical values of untreated and surface treated samples are shown in Fig. 6.7 and Table 6.2 respectively. The termination of the passivation process specifies the breakdown potential (E_{BD}) after which the passive current density increases rapidly. After the breakdown potential, the passive film formed over the sample surface dissociates and leads to formation of pits. The surface morphology of the samples after corrosion testing is shown in Fig. 6.9. The pits in the base metal sample were comparatively deeper and distributed across the entire surface whereas fewer shallow pits were seen in welded sample. This is due to the fact that the E_{BD} of FSP sample was slightly higher than the untreated sample. The current density (I_{corr}) of the welded sample was one order higher than the base metal. The current density values indicate that the welded sample displays lower corrosion resistance. The corrosion potential (E_{corr}) of welded sample has shown a negative shift compared to the base metal sample. Fig. 6.8 shows the corrosion rate of the samples. The corrosion rate has increased after welding. The corrosion rate of base metal and the welded sample were 6.2 $\times 10^{-4}$ mm/year and 2.68 $\times 10^{-3}$ mm/year respectively.

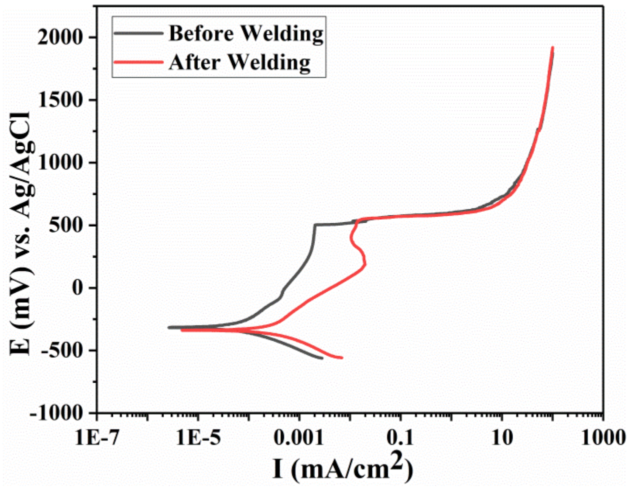

Fig. 6.7: Polarization curves of the NiTi alloy before and after welding

Table 6.2: The electrochemical parameters derived from potentiodynamic polarization measurements

Samples	**E_{corr} (mV)**	**I_{corr} (mA/cm^2)**	**βa (mV/dec)**	**βc (mV/dec)**	**Polarization resistance LPR ($ohm. Cm^2$)**	**E_{BD} (mV)**
Before welding	-315.6	3.78×10^{-5}	176.5	114.7	18.70	502.1
After welding	-338.5	1.5×10^{-4}	136.0	99.6	18.9	558.6

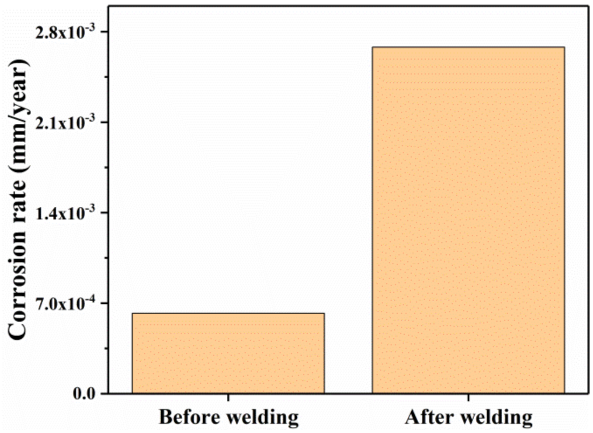

Fig. 6.8: Corrosion rates of the samples

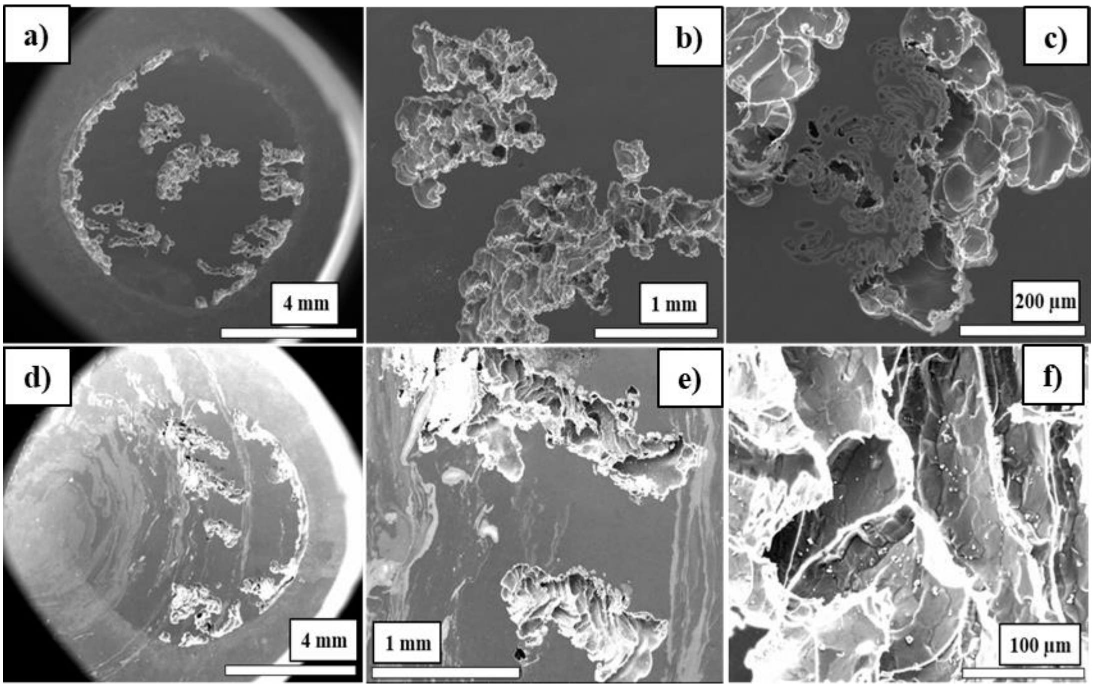

Fig. 6.9: SEM morphologies after corrosion testing in 3.5% NaCl solution a-c) Before welding and d-f) After welding

6.4 Electrochemical corrosion test of welded samples at different tool rotational speeds

This section discusses the electrochemical corrosion testing of friction stir welded NiTi alloy at 800 rpm and 1000 rpm. Fig. 6.11 shows the open circuit potential of the samples. The OCP of welded samples were more negative than the base metal. Initially, the OCP of 1000 rpm weld has decreased steeply and then increased after 2 hours before saturation.

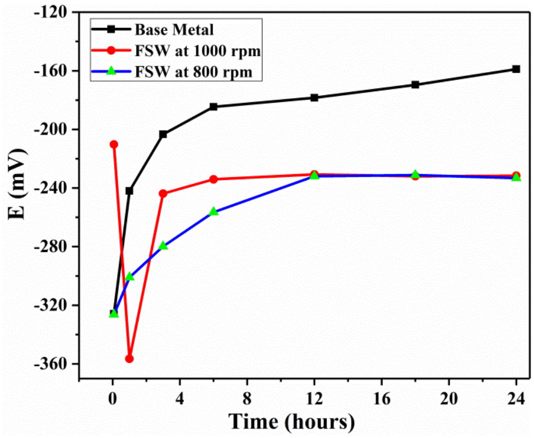

Fig. 6.10: Open circuit potential for base metal and friction stir welded NiTi alloy

The Nyquist plot, bode impedance and phase angle plots are shown in Fig. 6.12-14 respectively. In case of Nyquist plot, both base metal and the weld has straight lines corresponding to any diffusion reactions and absorption of corrosion products in the surface. The impedance value of the 1000 rpm weld was lower than the base metal and 800 rpm weld. In case of 1000 rpm weld, there exists a deviation of phase angle from 90° signifying the inhomogeneous formation of corrosion products on the surface.

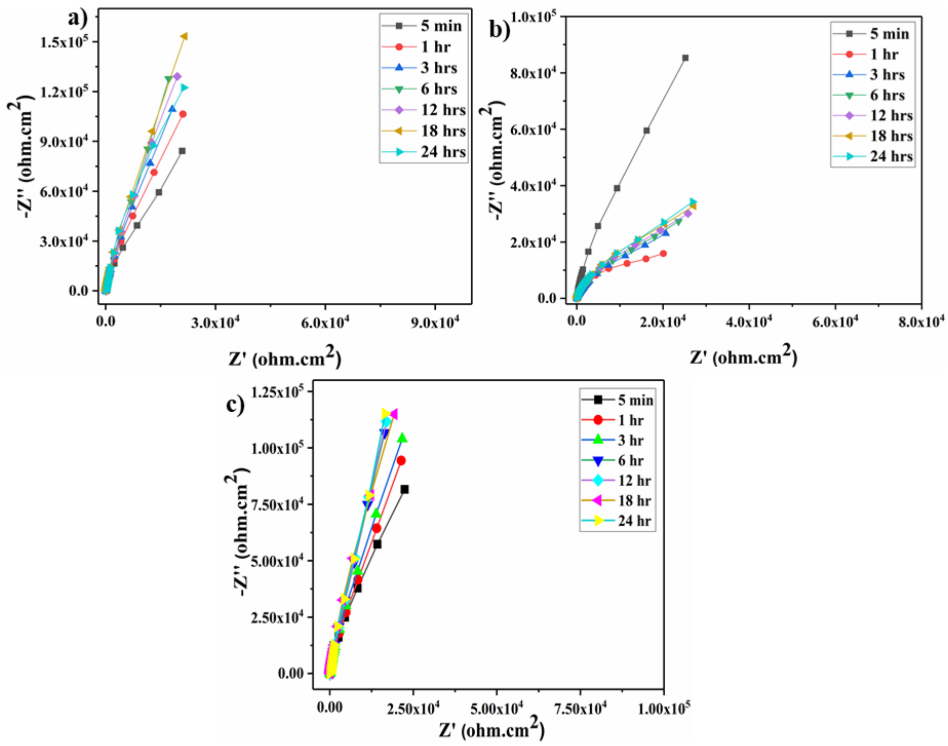

Fig. 6.11: Nyquist plot as function of immersion time a) Base metal, b) FSW at 1000 rpm and c) FSW at 800 rpm

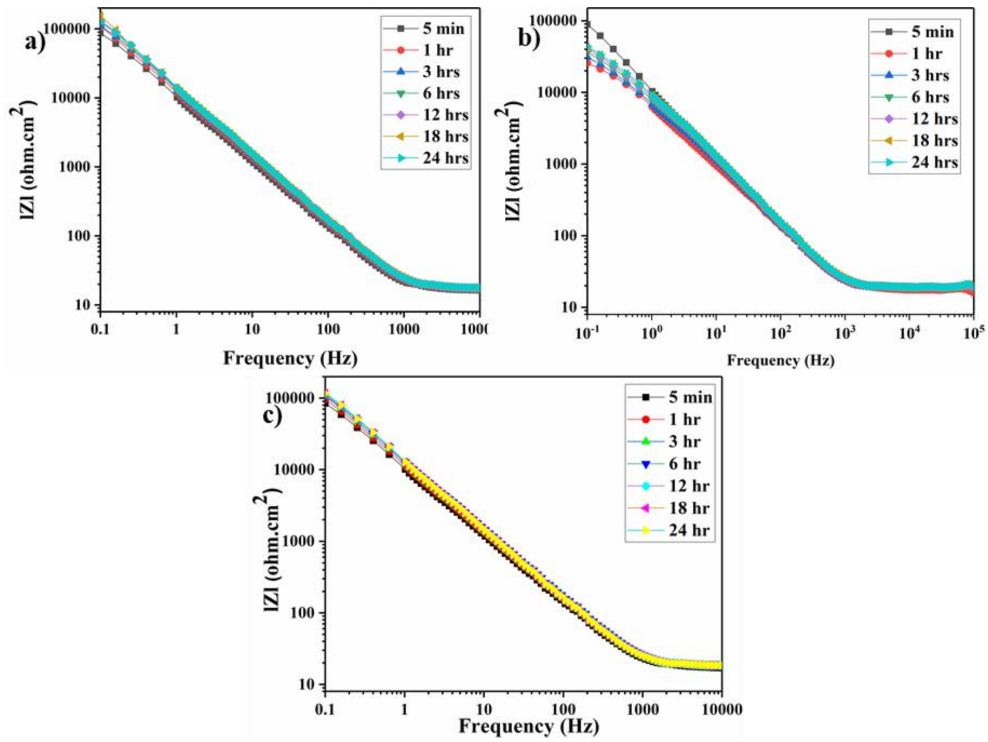

Fig. 6.12: Bode impedance plot as function of immersion time a) Base metal, b) FSW at 1000 rpm and c) FSW at 800 rpm

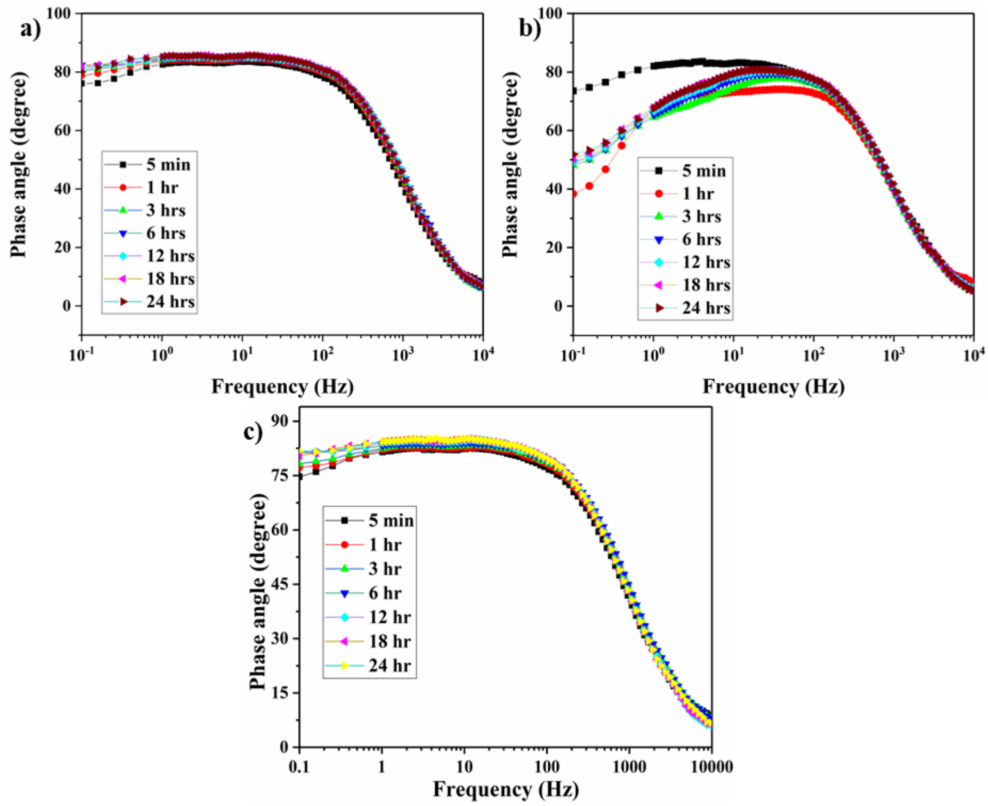

Fig. 6.13: Bode phase angle plot as function of immersion time a) Base metal, b) FSW at 1000 rpm and c) FSW at 800 rpm

The anodic potentiodynamic behaviour of the weld is shown in Fig. 6.14. The breakdown potential (E_{BD}) has reduced to a lower value of 350 mV for the weld made at 1000 rpm. Due to this, the weld has shown susceptibility to pitting corrosion. The current density value of 1000 rpm weld was 1.5×10^{-4} mA/cm^2 which is one order higher than the base metal confirming reduction in corrosion resistance after welding. The corrosion rates of the sample are shown in Fig. 6.15. Interestingly, the weld at 800 rpm has exhibited the lowest corrosion rate of 3.46 $\times10^{-4}$ mm/year. The corrosion rates of base metal and 1000 rpm weld were 4.97 $\times10^{-4}$ mm/year and 1.62 $\times10^{-3}$ mm/year respectively. Fig. 6.16 shows the scanning electron microscope images after corrosion testing. The pitting sites in the weld are clearly visible whereas the base metal and 800 rpm weld were free form pits. The transgranular corrosion was evident from the SEM morphologies. The Cl^- ions in the electrolyte preferably attack the grains and only the grain boundaries will be retained.

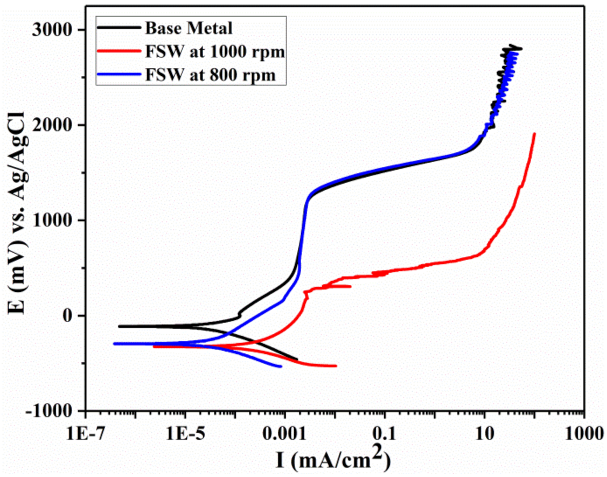

Fig. 6.14: Potentiodynamic polarization curve of the base metal and friction stir welded NiTi alloy

Table 6.3: Electrochemical parameters derived from potentiodynamic polarization measurements

Samples	E_{corr} (mV)	I_{corr} (mA/cm^2)	βa (mV/dec)	βc (mV/dec)	Polarization resistance LPR (ohm. Cm^2)	E_{BD} (mV)
Base metal	-118.83	4.62×10^{-5}	348.92	215.44	82.616	1275
FSW 1000 rpm	-326.13	1.5×10^{-4}	195.78	146.69	20.22	350
FSW 800 rpm	-294.09	3.2×10^{-5}	306.4	179.1	80.859	1295

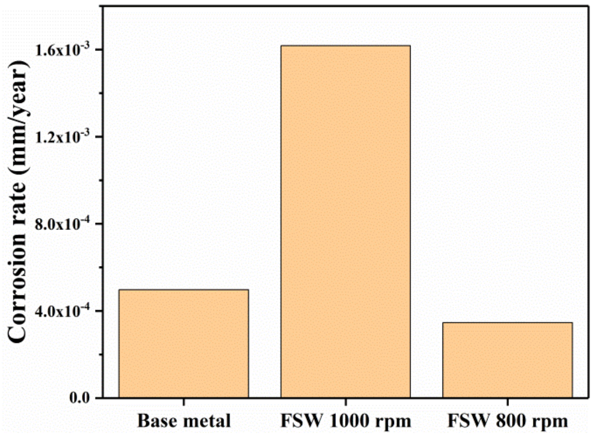

Fig. 6.15: Corrosion rates at different tool rotational speeds

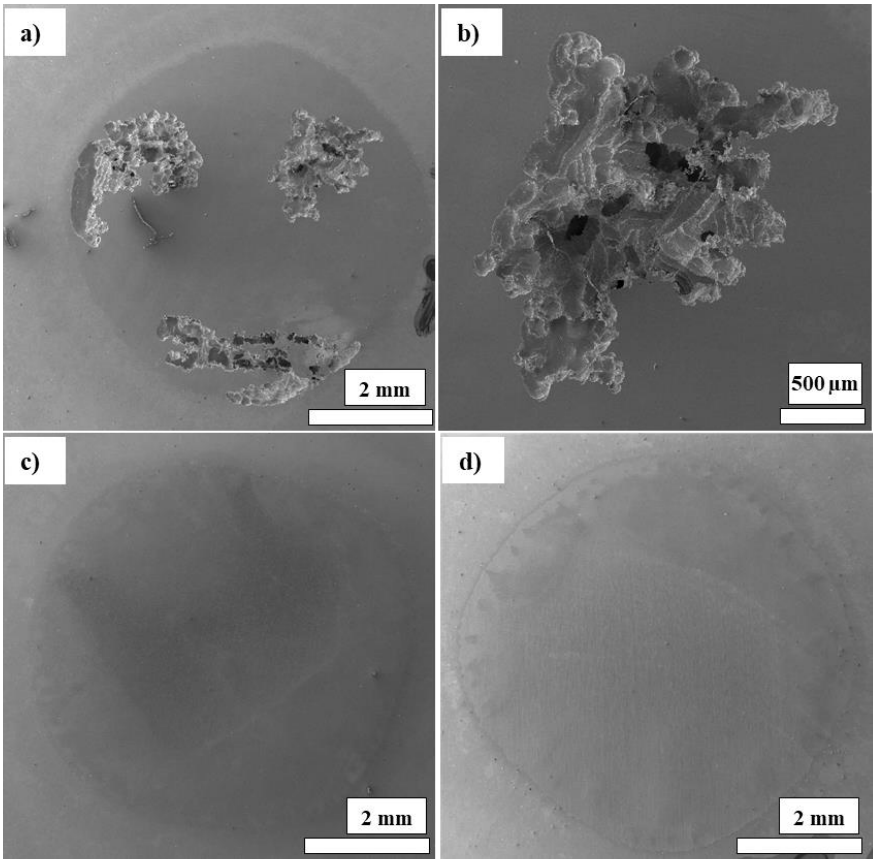

Fig. 6.16: SEM images of the samples after corrosion testing a-b) FSW at 1000 rpm, c) FSW at 800 rpm and c) Base metal

6.5 Influence of friction stir welding on the corrosion behaviour of the NiTi alloy

As we know, the friction stir welding is a thermomechanical process which affects the grain sizes significantly. The grain refinement taking place in a material subjected to a deformation process alters the grain boundary density, orientation and residual stresses [141,142]. The fine grained material with higher grain boundary densities changes the atomic coordination, reactivity and diffusion rates of the surfaces. In case of FSW, the induced frictional heat and severe plastic deformation causes dynamic recrystallization and leads to grain refinement in the processed zone [108,143]. More details can be found in the section 3.4 of chapter 3. The weld at 800 rpm has lowest grain size compared to other welds. This would have enabled the formation of stable oxide layer in the surface hampering the corrosion. In FSW, a asymmetry in the strain rate and temperature distribution across the processing region (i.e. the pin region experience more plastic deformation and temperature than the side regions) generates different zones such as stir or nugget zone, thermo-mechanically affected zone (TMAZ) and heat affected zone (HAZ). Typically, the stir zone contains finer grains than the other regions. The size of the stir zone is approximately equal to the tool pin diameter (5 mm) and hence, the welded sample invariably contains zones with varying grain sizes as shown in Fig. 6.17 [143,144]. The finer grains than the base metal have enhanced the corrosion behaviour of the welded sample (1200 rpm) as evident from the higher breakdown corrosion potential. However, the interface of different zones (formed due to difference in grain sizes) could have prevented the uniform formation of passive oxide layer as evident from the lower magnitude of $R_{(ox)}$ (Table. 6.1). Apart from the grain size, the presence of tungsten inclusions and residual stress in the weld may affect the corrosion behaviour.

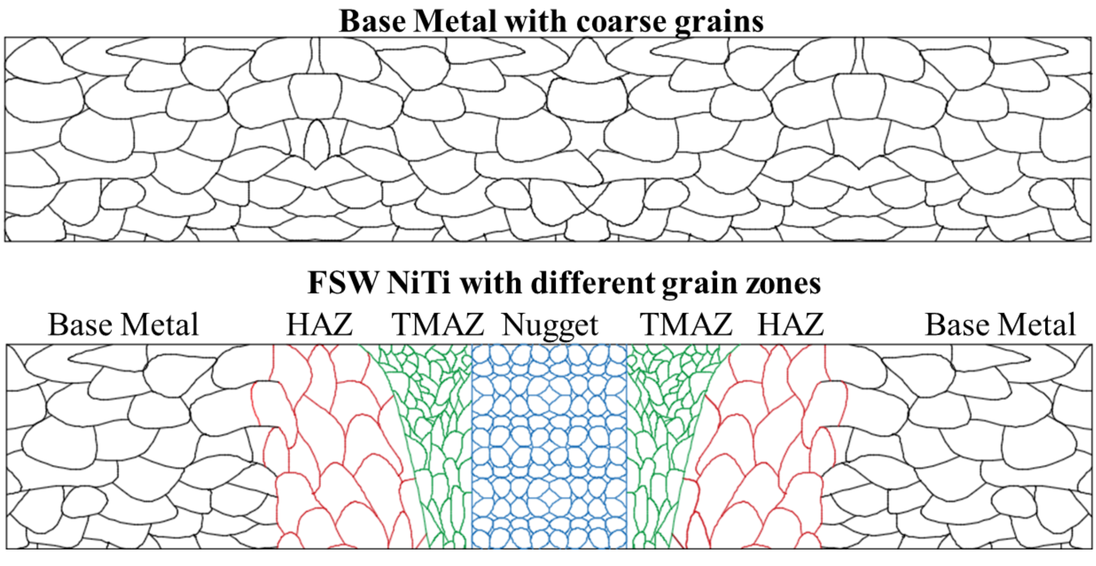

Fig. 6.17: Schematic of cross section microstructures of NiTi alloy a) Before welding and b) After welding

6.6 Summary

The corrosion behaviour of the friction stir welded NiTi alloy at different tool rotational speeds has been investigated in detail. The electrochemical corrosion testing has given more insights in to the thermodynamic stability, passivation tendency, pitting formation etc. of the welded NiTi alloy. The lower tool rotational speed (800 rpm) exhibited the better corrosion resistance whereas the higher rotational speed (1200 rpm) showed the least corrosion resistance. Notably, the weld at 1000 rpm and 1200 rpm were susceptible to formation of pits. The corrosion rates of weld at 800 rpm and 1200 rpm were 3.46×10^{-4} mm/year and 2.68×10^{-3} mm/year respectively. The variation in the corrosion behaviour of the NiTi alloy at different tool rotational speeds could be attributed to the grain size, tungsten inclusions, inhomogeneous grain zones etc.

Chapter 7

Influence of Surface Mechanical Attrition Treatment and Laser Shock Peening on the Corrosion Behaviour of Friction Stir Welded NiTi Alloy

7.1 Introduction

To improve the functional characteristics and corrosion resistance of nitinol alloys, various surface layers such as titanium oxide, titanium nitride, calcium phosphate etc. has been reported widely [145–148]. On the other hand, surface mechanical treatments are surface deformation process which usually induces compressive residual stresses and work hardening close to the surface. Unlike surface coatings and thermal treatments, the surface mechanical treatments such as shot peening, surface mechanical attrition treatment, laser shock peening and deep rolling are preferred surface modification technology because it enhances fatigue strength and cyclic behaviour of components. While preferring the surface mechanical treatments such as SMAT and LSP, it is important to understand the influence of the surface treatments on the corrosion behaviour. In this chapter, the SMAT and LSP of friction stir welded NiTi alloy have been discussed. The influence of these surface treatments on corrosion behaviour of the welded NiTi alloy has been evaluated using electrochemical corrosion testing.

7.2 Surface mechanical attrition treatment

SMAT is a cold working process where hard balls of high impact energy will indent the surface. Each impact on the sample surface causes severe plastic deformation at high strain rates [149,150]. Only flat sample surfaces are suitable for SMAT process. SMAT process is slightly different from conventional shot peening process. In shot peening, small balls (diameter 0.2 – 1 mm) will impact the work surface at higher velocities up to 100 m/s. In case of SMAT process, smooth surfaced hard balls having diameter 3- 10 mm will be used at velocities 1-20 m/s.

SMAT was carried out in a setup developed by surface engineering and heat treatment research group of IIT Indore (Headed by Dr. Santhosh Hosmani). The system consists of a vibrating chamber having capability to supply a constant frequency of 100 Hz. The hardened steel balls of diameter 6 mm were used and the stand-off distance of the sample was maintained at 25 mm. During SMAT, the impacts of the balls are random-multi directional and cannot be controlled. So, in order to ensure that the entire surface of the NiTi sample has been indented, three different time durations viz. 1 hour, 1.15 hour and 1.5 hour were used. The schematic of the SMAT process is shown in Fig. 7.1.

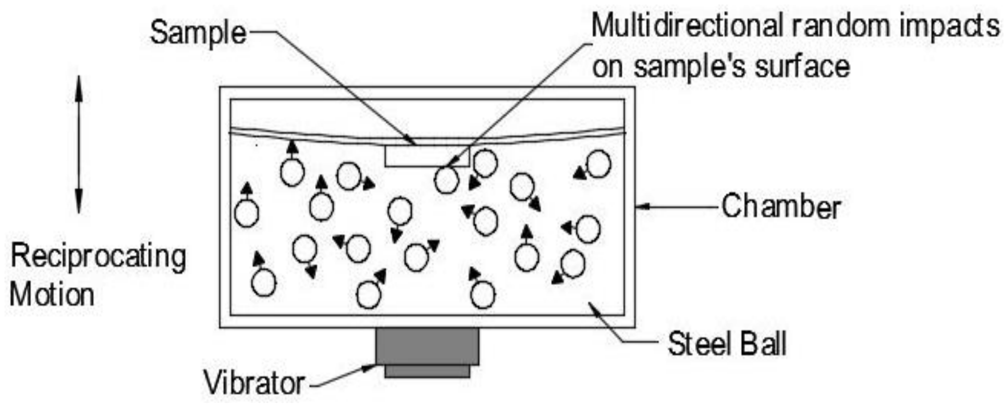

Fig. 7.1: Schematic of the SMAT process

7.3 Laser shock peening

LSP is a non-contact method which induces beneficial high magnitude compressive residual stresses to depth four times greater than conventional shot peening process [151]. Fig. 7.2 shows the process schematic of LSP. These compressive stresses are resultant of high magnitude shock waves generated upon irradiation using high energy laser. Usually, laser wavelength of 1064 nm having pulse width in nanoseconds will be used for peening. Laser spot size, pulse duration and laser energy are the important parameters affecting the LSP process [152–154]. Transparent overlays such as water or glass will cover the sample during peening which serves as a confining medium for better shock wave propagation. The parameters used for LSP is given in the Table 7.1. The laser spot size was 0.6 mm and in each spot three laser shots were made. The peening was carried out at the focal point (30 cm). Then the laser spot was moved and the subsequent laser spot was made 50 % overlap with the previous peened spot. The overlap was made to ensure complete coverage of the sample surface.

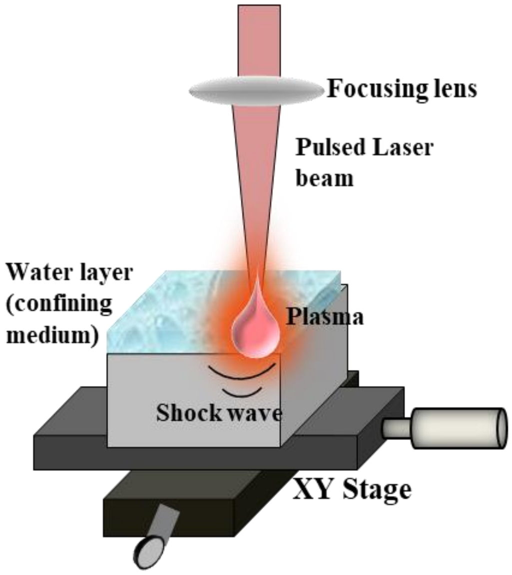

Fig. 7.2: Schematic of the LSP process

Table 7.1: Details about the parameters used for LSP process

Parameter/Conditions	**Value**
Laser wavelength	1064 nm
Mode of operation	Q-switched, single shot
Laser fluence	60 J/cm^2
Laser pulse duration	9 ns
Laser spot size	0.6 mm
Overlap between the spots	50 %
Thickness of water layer above the sample	3 mm

7.4 Surface morphology before corrosion testing

The samples of dimension 10 mm × 10 mm × 1.2 mm has been cut using wire electrical discharge machine from the friction stir weld region made at the tool rotational speed of 1000 rpm. Then the welded sample was polished using SiC papers of various grades up to 1200 grit. After polishing, they were cleaned using distilled water and sonicated for 15 min. After cleaning, the surface treatments such as LSP and SMAT have been applied to the welded samples. Before corrosion testing, the surface morphology has been studied using SEM. Fig. 7.3 shows the surface morphology of the samples. The SMAT and LSP process has significantly affected of the sample surface. The surface of the base metal was smooth and free from any surface irregularities (Fig. 7.3a-b). In the SMAT sample surface, the micro dents are clearly visible due to the striking of the hard balls (Fig. 7.3c-d). All the SMAT samples viz. 1 hr SMAT, 1.15 hr SMAT, and 1.5 hr SMAT had the same surface morphology. The LSP samples have definite circular pattern representing the impinging of the high energy laser shots along with surface pores clearly visible across the sample.

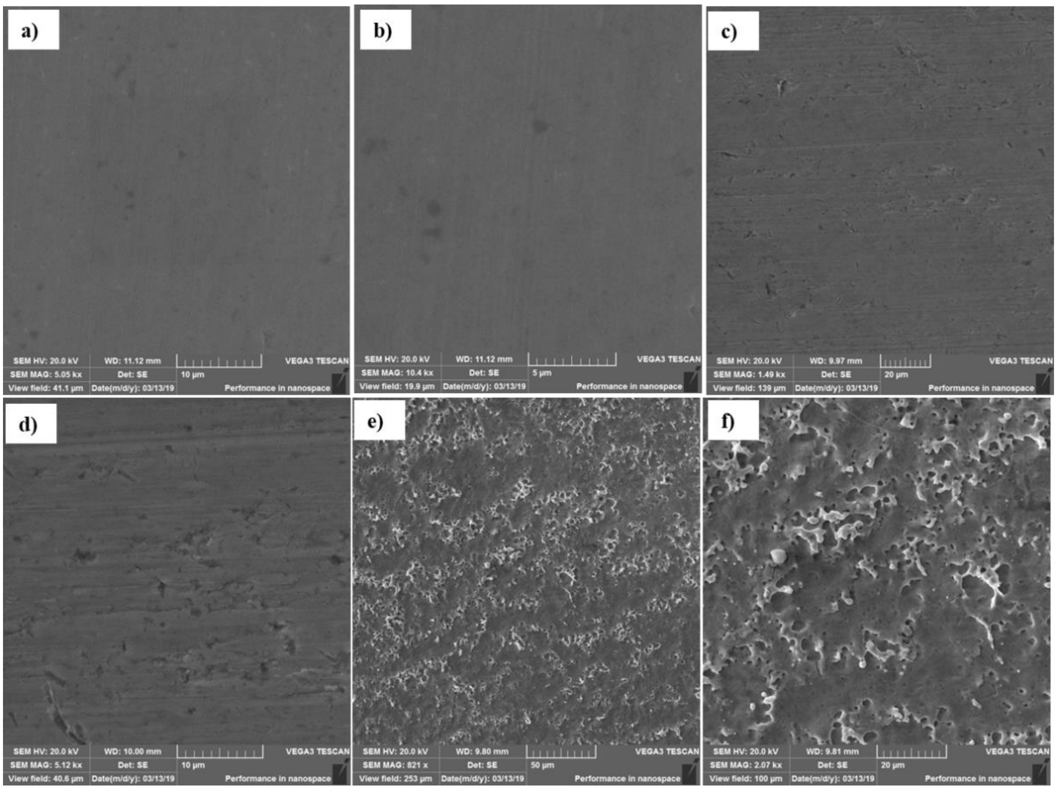

Fig. 7.3: SEM images of the samples before corrosion testing a-b) Base metal, c-d) SMAT and e-f) LSP

7.5 Open circuit potential

More details on the electrochemical corrosion testing conditions can be found in section 6.2 (Chapter 6). Open circuit potential is the measurement of sample potential with respect to the reference electrode when no external driving potential or current applied to the corrosion system. This measurement gives insight in to the thermodynamic tendency of the metal sample with the environment. At open circuit potential, the rate of cathodic and anodic reactions taking place in the metal surface will be in equilibrium. When NiTi surface interacts with the NaCl solution, the aggressive Cl^- ions attacks and dissociates the original oxide layer from the NiTi surface. Once the ions break the Ni-Ti bond, Ni ions dissolute into the electrolyte and formation of titanium oxides in the surface happens simultaneously. Due to the dissolutions and subsequent recovery, the potential in the open circuit condition fluctuates. The first stage on OCP curve has fluctuations due to the repetitive dissolution and formation of oxide layer. After longer immersion time, equilibrium exists between the corrosion and recovery leading to constant OCP. Fig. 7.4 shows the OCP of the surface peened samples. The E_{OCP} value of 1.15 hr SMAT sample was more negative whereas the 1 hr SMAT has more positive values. The more positive potential signifies noble behaviour and the sample is thermodynamically more stable with less susceptibility to corrosion.

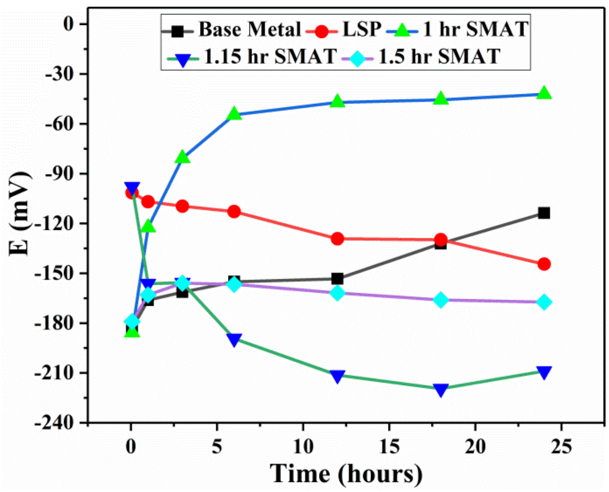

Fig. 7.4: Evolution of open circuit potential with respect to time for peened samples

7.6 Electrochemical impedance spectroscopy

The EIS measurements will give information on the general corrosion tendency and variation in the corrosion mechanism at any stage during corrosion testing. EIS was evaluated at consecutive intervals until 24 hours. The Nyquist, Bode impedance modulus, and Bode phase angle plot are shown in Fig. 7.5, Fig. 7.6, and Fig. 7.7 respectively. The EIS spectra was modelled with electrochemical equivalent circuits and fitted with the complex non-linear least square method. More information about the equivalent circuits can be found in the section 6.3.2 (Chapter 6). The equivalent circuit and extracted values from EIS spectra fitting is shown in Fig. 7.8 and Table 7.2 respectively. The chi-square (χ^2) value in the order of 10^{-3} shows good agreement of fitted data with the experiment for all the samples. $R_{(ox)}$ signifies the resistance of the characteristic titanium layer formed over the sample surface. For all the samples, the $R_{(ox)}$ will increase over time and the maximum values can be found for the 24th hour. For base metal, the magnitude of $R_{(ox)}$ for initial 5 minutes and final 24 hours immersion was 468760 Ωcm^2 and 1.095×10^6 Ωcm^2 respectively. At final 24th hour, the 1.15 hr SMAT had the lowest $R_{(ox)}$ of 936020 Ωcm^2 whereas the LSP sample has shown the highest $R_{(ox)}$ value of 2.807×10^6 Ωcm^2. If the $R_{(ox)}$ is higher, then the sample have lesser tendency to corrode and formation of pits in the surface will be avoided. As per the resistance of the oxide layer was concerned, the LSP surface shows less susceptibility to corrosion compared to the other samples. In order to ascertain the statement, the potentiodynamic polarization test has to be carried out.

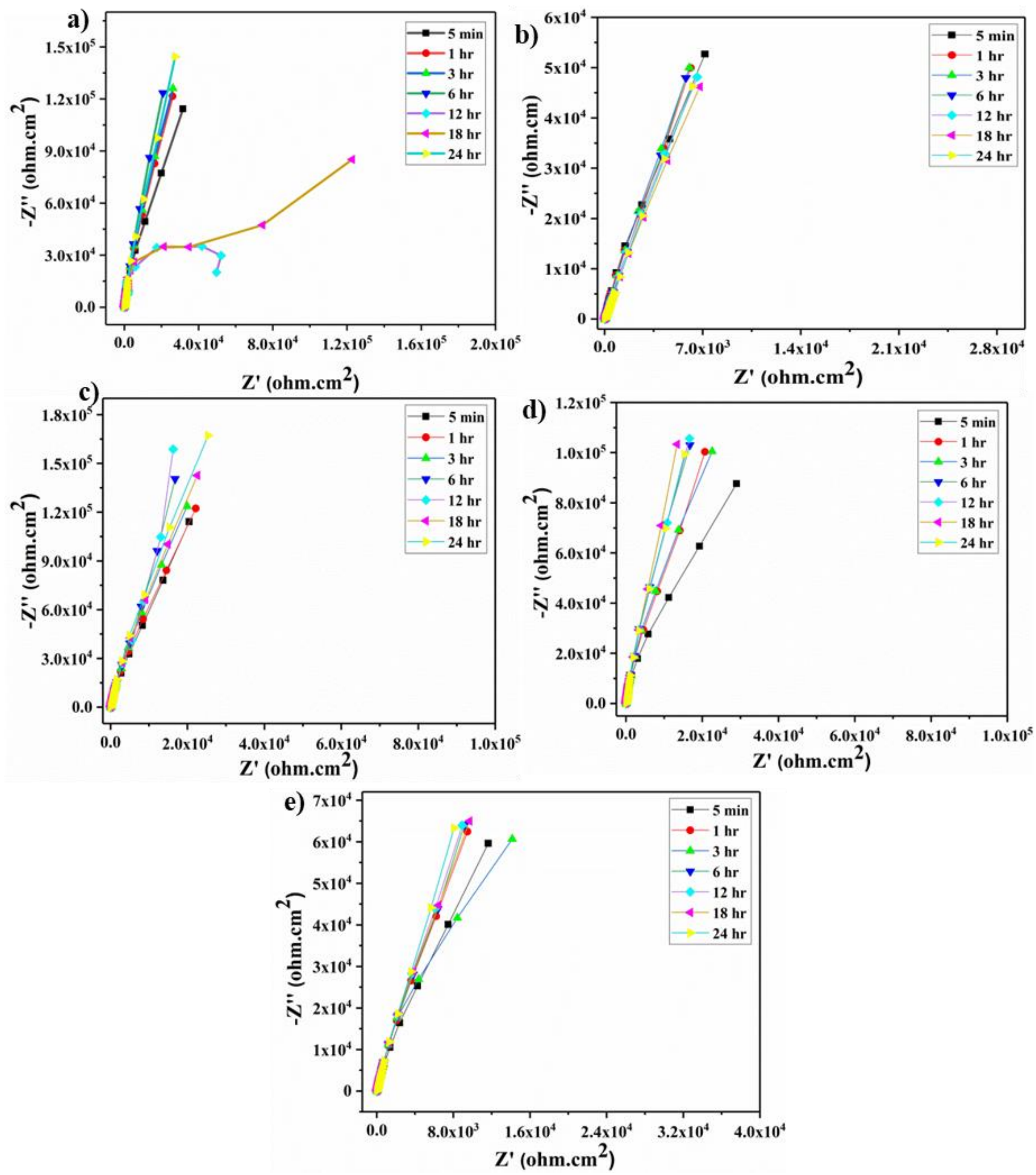

Fig. 7.5: Nyquist plot as a function of immersion duration a) Base metal, b) LSP, c) 1 hr SMAT, d) 1.15 hr SMAT, and e) 1.5 hr SMAT

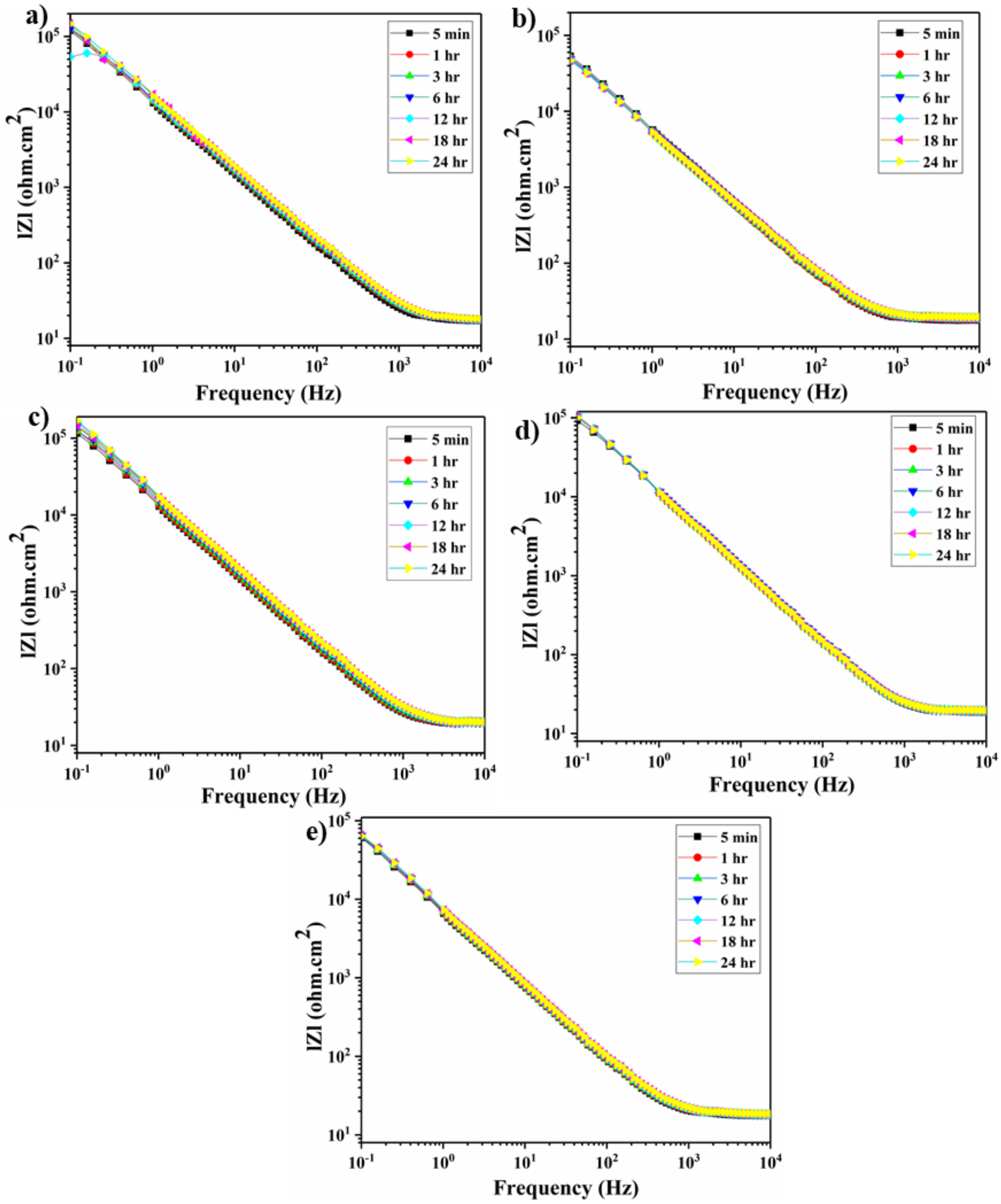

Fig. 7.6: Bode impedance modulus plot as a function of immersion duration a) Base metal, b) LSP, c) 1 hr SMAT, d) 1.15 hr SMAT, and e) 1.5 hr SMAT

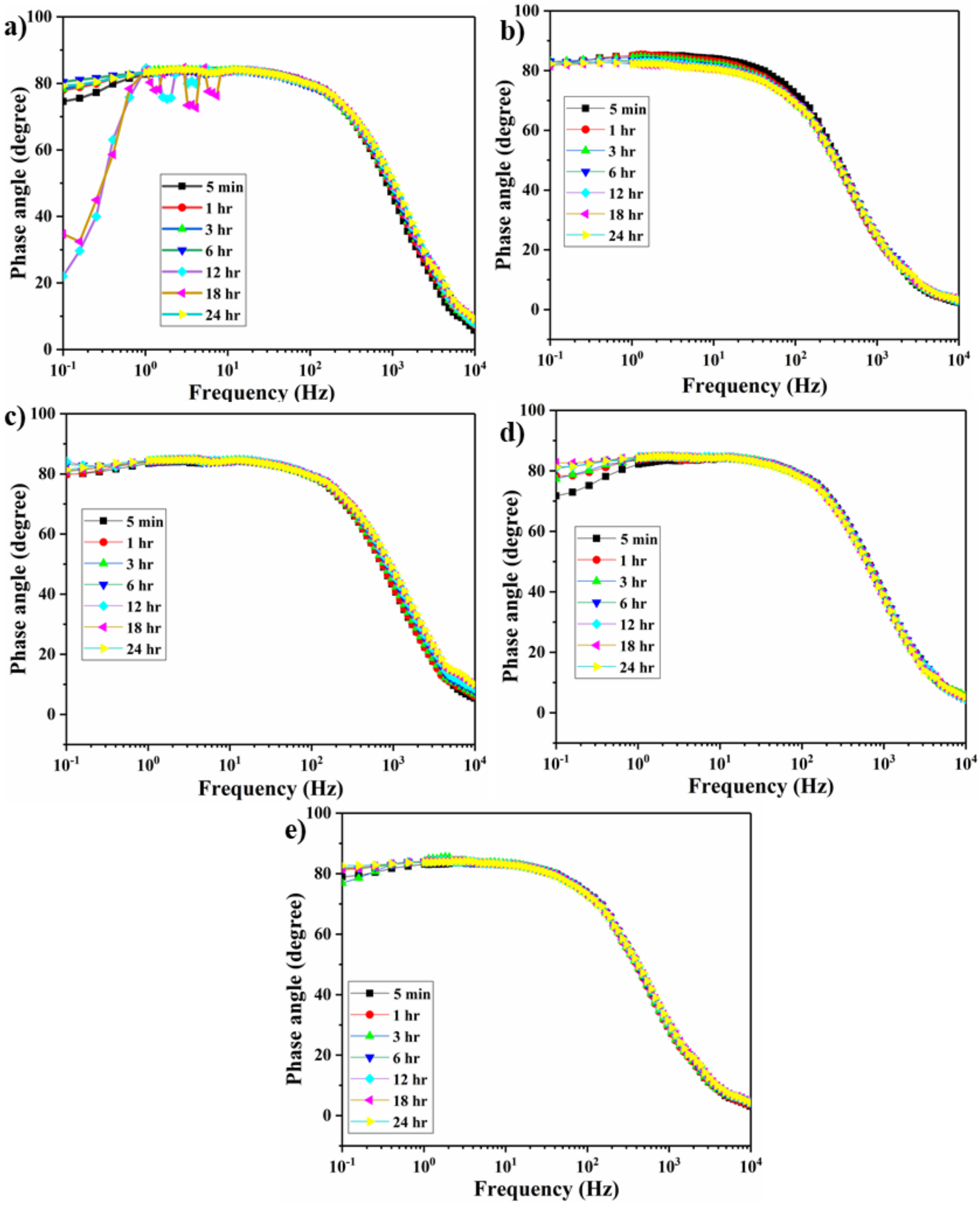

Fig. 7.7: Bode phase angle plot as a function of immersion duration a) Base metal, b) LSP, c) 1 hr SMAT, d) 1.15 hr SMAT, and e) 1.5 hr SMAT

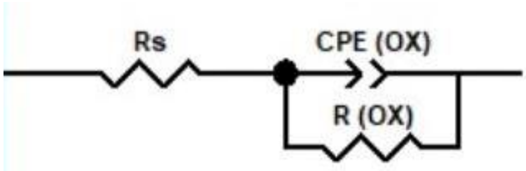

Fig. 7.8: Equivalent circuit for the corrosion behaviour of surface peened NiTi alloy in 3.5 % NaCl solution

Table 7.2: Electrical parameters obtained from the equivalent circuit diagram for the impedance spectra of surface peened NiTi alloy as a function of immersion duration in 3.5% NaCl solution

Description	**Samples/ EC parameters**	**R_s**	**$CPE_{(OX)}$-T**	**$CPE_{(OX)}$-P**	**$R_{(Ox)}$**	**χ^2 - Value**
	Units	Ωcm^2	$\Omega^{-1} cm^{-2} s^{\alpha}$	-	Ωcm^2	-
Base metal	5 min	16.8	1.289E-5	0.95377	468760	0.0026714
	24 hrs.	17.9	1.05E-5	0.94579	1.0954E6	0.0018491
LSP	5 min	17.7	2.953E-5	0.95628	654590	0.0019372
	24 hrs.	19.5	3.368E-5	0.92377	2.8073E6	0.0020449
1 hr SMAT	5 min	19.5	1.295E-5	0.9528	797580	0.0027236
	24 hrs.	19.9	9.91E-6	0.95159	1.972E6	0.0033191
1.15 hr SMAT	5 min	19.6	1.486E-5	0.95742	286730	0.006052
	24 hrs.	19.8	1.487E-5	0.95516	936020	0.0029658
1.5 hr SMAT	5 min	17.6	2.600E-5	0.94464	450670	0.0016015
	24 hrs.	18.5	2.398E-5	0.93946	1.619E6	0.001672

7.7 Potentiodynamic polarization analysis

Potentiodynamic anodic polarization test is the characterization to obtain current-potential relationship of a metal specimen. When the potential of the sample is increased slowly in the positive direction, the sample becomes anode and tends to corrode. The current-potential relation under controlled process conditions give information about the corrosion rates, passivation tendency, pitting etc. In a short period of time, the overall current-potential relationship can be recorded. The anodic polarization curve and the extracted values are given in Fig. 7.9 and Table 7.3 respectively. Corrosion potential, E_{corr} signifies the ionization tendency of the material in the electrolyte whereas the corrosion current, I_{corr} represents the flow of current at open circuit potential due to the oxidation and reduction reactions. The lower corrosion current signifies that the sample surface has better corrosion resistance. The surface peening treatment has enhanced the corrosion resistance of the NiTi alloy as observed from the lower corrosion currents in the order of 10^{-5} mA/cm^2. It is noteworthy to observe that the as welded NiTi alloy at 1000 rpm and 1200 rpm has shown higher corrosion currents in the order of 10^{-4} mA/cm^2 (Chapter 6). The breakdown potential (E_{BD}) of the all the samples were more than 1200 mV signifying good corrosion resistance. However, the LSP sample has exhibited the lowest breakdown potential of 406 mV.

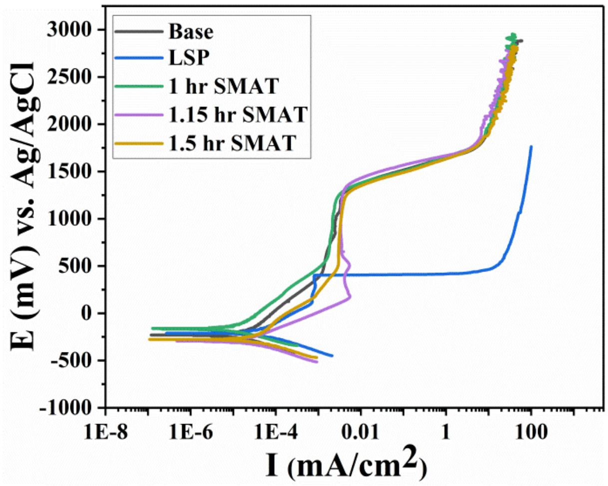

Fig. 7.9: Polarization curves of the friction stir welded NiTi alloy after peening

Table 7.3: The electrochemical parameters derived from potentiodynamic polarization measurements.

Samples	E_{corr} (mV)	I_{corr} (mA/cm^2)	βa (mV/dec)	βc (mV/dec)	Polarization resistance LPR (ohm. Cm^2)	E_{BD} (mV)
Base metal	-233.24	1.51×10^{-5}	335.78	151.78	74.308	1266
LSP	-210.66	3.45×10^{-5}	242.05	125.79	16.94	406
SMAT 1 hr	-161.72	1.2×10^{-5}	332.11	148.52	73.804	1264
SMAT 1.15 hr	-294.8	1.94×10^{-5}	176.42	122.89	108.33	1331
SMAT 1.5 hr	-282.46	2.45×10^{-5}	318.08	117.07	71.12	1284

The corrosion rates of the surface peened samples are shown in Fig. 7.10. All the samples have demonstrated the least corrosion rates in the order of 10^{-4} mm/year. The LSP has exhibited the high corrosion rate of 3.7×10^{-4} mm/year compared to the other samples. The surface morphology of the samples after corrosion testing is shown in Fig. 7.11 and 7.12.

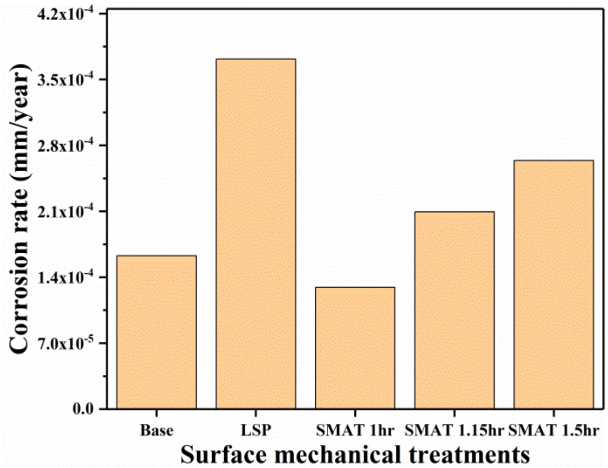

Fig. 7.10: Corrosion rates of the surface peened samples

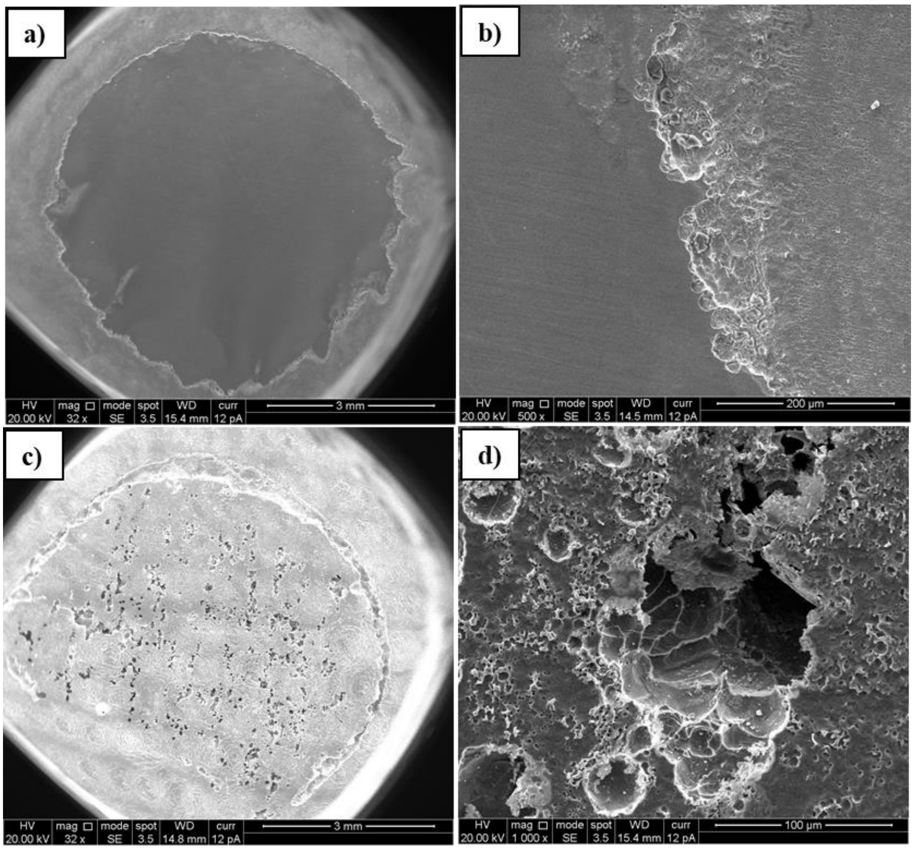

Fig. 7.11: SEM images of the samples after corrosion testing a-b) Base metal and c-d) LSP samples

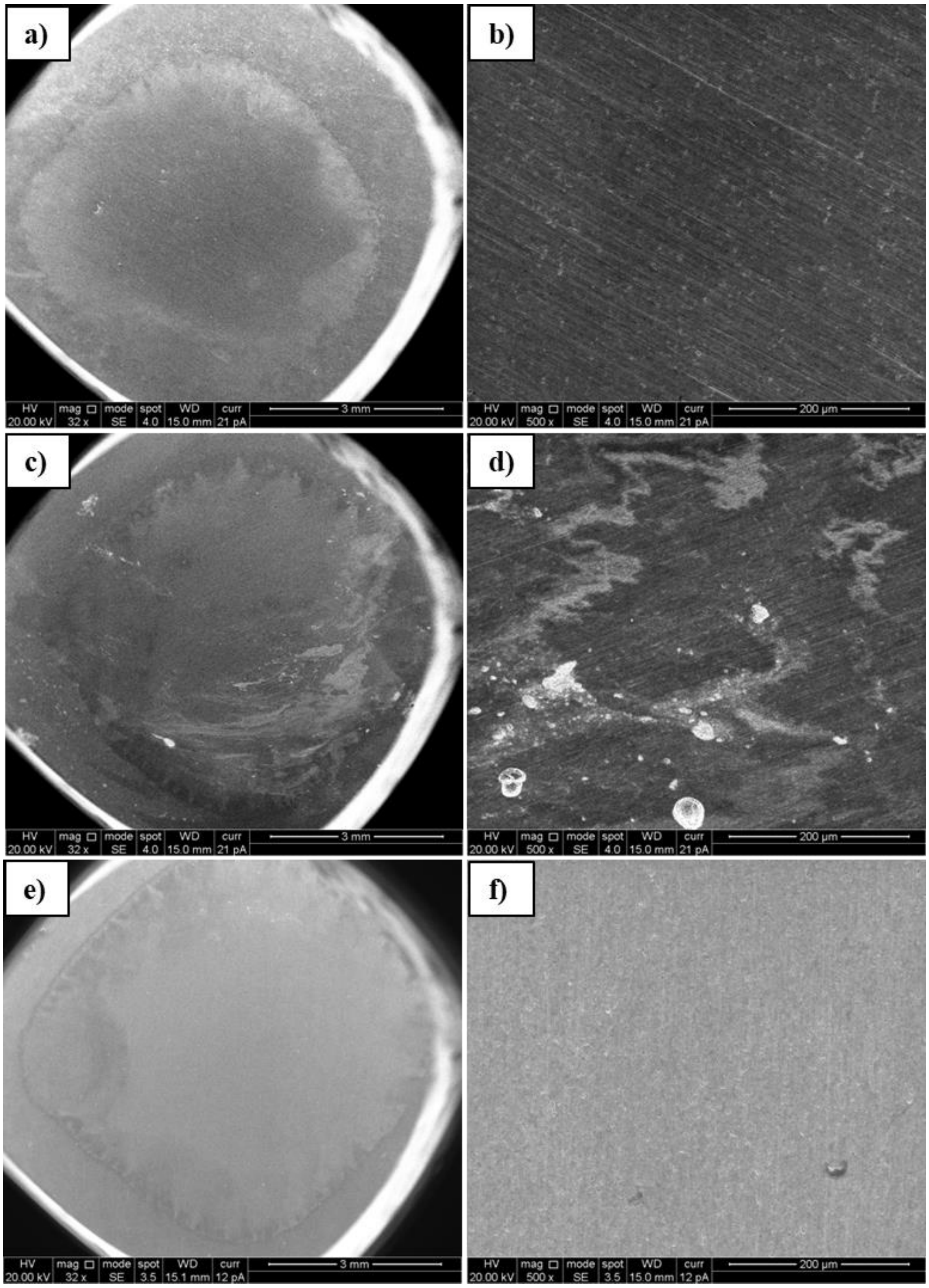

Fig. 7.12: SEM images of the samples after corrosion testing a-b) 1 hr SMAT, c-d) 1.15 hr SMAT and e-f) 1.5 hr SMAT

7.8 Influence of SMAT and LSP on the corrosion behaviour

There are many reports where the grain refinement of various materials (steels, Ti alloy, Mg alloy, NiTi) has improved the corrosion resistance due to better kinetics of passive film formation over the surface [155–159]. SMAT and LSP lies under the category of severe plastic deformation (SPD) processes which are known to produce nanocrystalline structures due to the associated high strain rates (10^2-10^3 s^{-1}) [107,149]. Hu et al. has observed that the severely deformed surface layer of SMAT NiTi contains nanocrystallites and amorphous structure [105]. It is obvious that the nanocrystalline structures possess large volume of grain boundaries and triple junctions. These surface dislocations and defects act as nucleating sites for the formation of more uniform and dense passive film [103]. The presence of amorphous structure on SMAT NiTi surface would increase the overall corrosion resistance. This is due to the fact that amorphous structure is chemically homogenous without any grain boundaries and precipitates which in turn significantly improves the resistance to pitting corrosion [160]. The surface of the SMAT samples was free from pit formation (Fig. 7.12). S. Olumi et al. showed that nano-crystallization of NiTi surface leads to significant increase in the amount of Ti atoms on the surface than Ni atoms and eventually enabled the formation of more titanium oxide in the alloy surface [161]. Thereby, the high quality passive oxide film formed over the nanocrystalline surface has offered better corrosion resistance than the coarse (base metal) or micro grained (welded) counterpart. Hence, the release of Ni ions having potentially negative effects (toxic, allergic or even carcinogenic) to human beings or failure of components due to pitting can be prevented through SMAT of NiTi alloy. The schematic of NiTi with nanocrystallites is shown in Fig.7.13. Though, LSP possess nanocrystalline surface, the presence of micro pores in the surface would have acted as the sites prone to pitting. This would have led to the early breakdown of oxide layer as notified by the lowest breakdown potential.

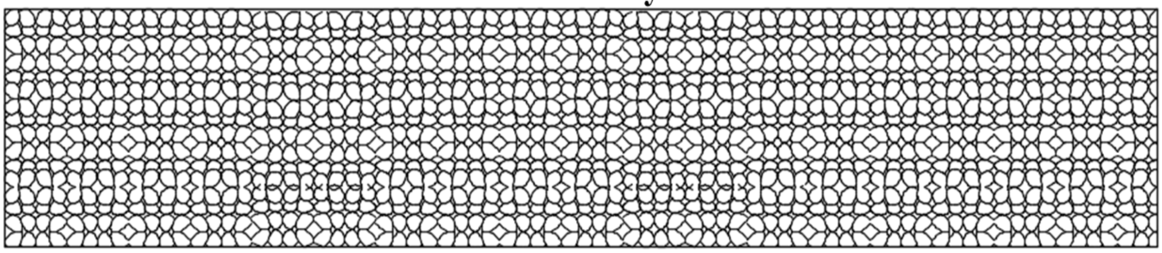

Fig. 7.13: Schematic of nanocrystallites in SMAT and LSP surfaces

7.10 Summary

The surface peening treatments such as SMAT and LSP has been applied over the friction stir welded NiTi alloy. The influence of the peening treatments on the corrosion behaviour of the NiTi alloy has been investigated in detail using electrochemical corrosion testing. Both the peening treatments have enhanced the corrosion resistance of the friction stir welded NiTi alloy. The presence of nanocrystalline surface might be attributed to the improvement in corrosion resistance compared to the non-peened friction stir welded NiTi alloy. All the samples have exhibited low corrosion rates in the order 10^{-4} mm/year. Notably, the 1 hr SMAT sample has recorded the lowest corrosion current of 1.2×10^{-5} mA/cm^2 and the least corrosion rate of 1.295×10^{-4} mm/year.

Chapter 8

Conclusions and Future Scope

8.1 Conclusions

The friction stir welding of NiTi shape memory alloy has been successfully carried out and has yielded promising results. The influence of tool rotational speeds on the weld properties has also been investigated. Apart from material characterization, the smart functional capabilities and corrosion behaviour have been evaluated in detail. The results of the work can be summarized as follows,

- FSW is a feasible method to join NiTi SMA as the weld has formed without intermetallics and the shape memory behaviour was retained after welding.
- The high temperature and deformation during welding causes dynamic recrystallization in NiTi alloy. Recrystallized grain size in the nugget has increased with the increasing rotational speed due to considerable rise in peak temperature and higher strain rate.
- Due to solid-state nature of the welding, austenite and martensite phases in base metal were retained in the weld without any inter transformation during welding.
- The phase transformation temperatures of the weld produced at 800 rpm was near identical to the base metal. However, the welds at 1000 and 1200 rpm have shown a marginal drift from the transformation temperatures of the base metal as they were significantly affected by high temperature during processing. The asymmetry of weld condition across the weld has led to drift in transformation temperatures in nugget, advancing, and retreating sides.
- Due to grain refinement, the weld at 1000 rpm has shown 17 % higher yield strength compared to the base metal. The weld joint efficiency at 800 rpm

and 1200 rpm was low and further optimization of welding parameters is required for improving the weld structural integrity.

- The centre region of the weld has shown variation in the weld composition due to the inclusions of tungsten from the welding tool. Apart from the centre region, the weld has composition close to the base metal ensuring good compositional compatibility.
- Tool wear was noticed for all the tool rotational speeds due to the harsh thermomechanical conditions experienced during FSW process. The tool wear was maximum for the weld at 1200 rpm due to which the particular weld has shown poor mechanical strength.
- The temperature distribution and strain rate at different tool rotational speeds has been evaluated using finite element analysis. The simulation has given better insight into the variation in the properties of NiTi alloy after welding. The maximum temperature and strain rate were predicted for the higher rotational speed 1200 rpm as 1094°C and 226 s^{-1} respectively.
- Tensile cycling behaviour of the weld has been explored at three different strain percentages 2.5, 3.5 and 4.5. The maximum stress of 590 MPa was recorded for 4.5% strain.
- The NiTi alloy has showed damping capabilities after welding. However, the hysteresis of the transformation has reduced compared to the base metal.
- The actuation ability of the welded structure has been evaluated using bending-recovery method. The welded structure has recovered the complete strain during hot plate actuation.
- The thermomechanical behaviour using electrical has shown the weld ability to actuate at different actuation parameters. At 5 A current, the maximum displacement of 17.8 mm was attained at the higher actuation speed of 60 mm/min. The life cycle analysis has been conducted up to 300 cycles and the sample didn’t show any sign for failure.
- The laser actuation was impulsive compared to the electrical actuation. The higher displacement and actuation speed of 28 mm and 342 mm/min was

achieved using laser actuation. However, the laser actuation based on scanning method has shown jerky behaviour during actuation.

- The corrosion behaviour of the weld has been studied using electrochemical corrosion testing. The weld at 800 rpm has exhibited better corrosion resistance than the other welds. The corrosion rates increased with the tool rotational speeds and the weld at 1200 rpm has shown the highest corrosion rate of 2.68×10^{-3} mm/year.

- The peening methods such as SMAT and LSP have improved the corrosion resistance of the friction stir welded NiTi alloy. They exhibited the lowest corrosion rates in the order of 10^{-4} mm/year. The SMAT process has showcased better corrosion resistance than the LSP.

8.2 Scope for future work

Though, FSW works well for the NiTi alloy, there are few challenges which have to be addressed to further extend the technology. Some recommendation for future work is as follow,

- Detailed investigation should be carried out to find out the ways to improve the tool life and widen the process parameters used for welding NiTi alloy.

- Since, the FSW is desirable for lap joints; the feasibility for the fabrication of bimetal composites of NiTi alloy (shape memory layer over pseudoelastic layer or other such combinations for showing TWSME) can be explored.

- Efforts should be taken to improve the tensile cyclic properties of the friction stir welded NiTi alloy.

- The low cycle and high cycle fatigue properties of the friction stir welded NiTi alloy should be evaluated.

- Investigations on the usage of interlayers such as copper to improve the weld properties can be performed.

- Influence of SMAT and LSP on the mechanical and fatigue properties of the weld can be studied.

References

[1] Thin film shape memory alloys:Fundamentals and device applications. Cambridge university press; 2009.

[2] Lagoudas DC, editor. Shape memory alloys:modelling and engineering applications. Springer; 2008.

[3] Mohd Jani J, Leary M, Subic A, Gibson MA. A review of shape memory alloy research, applications and opportunities. Mater Des 2014;56:1078–113.

[4] Mohd Jani J, Leary M, Subic A, Mark A. Gibson c. A review of shape memory alloy research applications and opprtunities. Bull Alloy Phase Diagrams 1980;1:93–5. doi:10.3868/s110-003-014-0039-x.

[5] Barbarino S, Flores EIS, Ajaj RM, Dayyani I, Friswell MI. A review on shape memory alloys with applications to morphing aircraft. Smart Mater Struct 2014;23:063001--. doi:10.1088/0964-1726/23/6/063001.

[6] Lagoudas DC. Shape Memory Alloys: Modeling and Engineering Applications. vol. 1. Springer; 2008. doi:10.1007/978-0-387-47685-8.

[7] Sun L, Huang WM, Ding Z, Zhao Y, Wang CC, Purnawali H, et al. Stimulus-responsive shape memory materials: A review. Mater Des 2012;33:577–640. doi:10.1016/j.matdes.2011.04.065.

[8] Yamauchi K, Ohkata I, Tsuchiya K, Miyazaki S. Shape Memory and Superelastic Alloys: Applications and Technologies. Woodland publishing limited; 2011.

[9] Machado LG, Machado LG, Savi M a, Savi M a. Medical applications of shape memory alloys. Brazilian J Med Biol Res 2003;36:683–91.

[10] Elahinia MH, Hashemi M, Tabesh M. Manufacturing and processing of NiTi implants : A review. Prog Mater Sci 2012;57:911–46. doi:10.1016/j.pmatsci.2011.11.001.

[11] Pelton AR, Stöckel D, Duerig TW. Medical Uses of Nitinol. Mater Sci Forum 2000;328:63–70.

[12] Kwok DTK, Schulz M, Hu T, Chu C, Chu PK. Surface Treatments of Nearly Equiatomic NiTi Alloy (Nitinol) for Surgical Implants. Biomed Eng Trends Mater Sci Intech 2011.

[13] Morgan NB. Medical shape memory alloy applications — the market and its products. Mater Sci Eng A 2004;378:16–23. doi:10.1016/j.msea.2003.10.326.

[14] Shape memory alloy actuators: Design, fabrication and experimental evaluation. John Wiley and Sons, Ltd; 2016.

[15] Oliveira JP, Miranda RM, Fernandes FMB. Welding and Joining of NiTi Shape Memory Alloys : A Review. Prog Mater Sci 2017;88:412–66. doi:10.1016/j.pmatsci.2017.04.008.

[16] Kannan TDB, Ramesh T, Sathiya P. A Review of Similar and Dissimilar Micro-joining of Nitinol. J Miner Met Mater Soc 2016;68:1227–45. doi:10.1007/s11837-016-1836-y.

[17] Mohd Jani J, Leary M, Subic A, Gibson MA. A review of shape memory alloy research, applications and opportunities. Mater Des 2014;56:1078–113.

[18] Lagoudas DC. Shape memory alloys: Modeling and engineering applications. springer; 2008.

[19] Friend PC, Allen PD, Webster J, Clark D, Goffin PK. Comparative study of Joining Methods for a SMART Aerospace Application. Cranf Univ Eng Dr Thesis 2007.

[20] Liu B, Wang Q, Hu S, Zhang W, Du C. On thermomechanical behaviors of the functional graded shape memory alloy composite for jet engine chevron. J Intell Mater Syst Struct 2018;29:2986–3005. doi:10.1177/1045389X18781257.

[21] Izquierdo J, González-marrero MB, Bozorg M, Fernández-pérez BM. Multiscale electrochemical analysis of the corrosion of titanium and nitinol for implant applications. Electrochim Acta 2016;203:366–78.

doi:10.1016/j.electacta.2016.01.146.

[22] Ozbulut OE, Hurlebaus S, Desroches R. Seismic response control using shape memory alloys: A review. J Intell Mater Syst Struct 2011;22:1531–49.

[23] Saadat S, Salichs J, Noori M, Davoodi H, Bar-on I, Suzuki Y, et al. An Overview of Vibration and Seismic Application of NiTi Shape Memory Alloy. Smart Mater Struct 2002;11:218–29.

[24] Choi E, Park S, Cho B, Hui D. Lateral reinforcement of welded SMA rings for reinforced concrete columns. J Alloys Compd 2013;577:S756–9. doi:10.1016/j.jallcom.2012.02.135.

[25] Mesquita TR, Martins LP, Martins RP. Welding strength of NiTi wires. Dental Press J Orthod 2018;23:58–62. doi:10.1590/2177-6709.22.3.058-062.oar.

[26] Tam B, Khan MI, Zhou Y. Mechanical and Functional Properties of Laser-Welded Ti-55 . 8 Wt Pct Ni Nitinol Wires. Metall Mater Trans A 2011.

[27] Zoeram AS, Rahmani A. Characterization the microstructure of pulsed Nd : YAG welding method in low frequencies ; correlation with tensile and fracture behavior in laser-welded nitinol joints. Smart Mater Struct 2017;055030.

[28] Chan CW, Man HC. Laser welding of thin foil nickeltitanium shape memory alloy. Opt Lasers Eng 2011;49:121–6. doi:10.1016/j.optlaseng.2010.08.007.

[29] Schlossmacher P, Haas T, Schüssler A. Laser-Welding of a Ni-Rich TiNi Shape Memory Alloy : Mechanical Behavior. Le J Phys IV 1997;07:C5-251-C5-256. doi:10.1051/jp4:1997539.

[30] Tuissi A, Besseghini S, Ranucci T, Squatrito F, Pozzi M. Effect of Nd-YAG laser welding on the functional properties of the Ni – 49 . 6at .% Ti 1999;275:813–7.

[31] Oliveira JP, Fernandes FMB, Miranda RM, Schell N, Ocaña JL. Effect of laser welding parameters on the austenite and martensite phase fractions of NiTi. Mater Charact 2016;119:148–51. doi:10.1016/j.matchar.2016.08.001.

[32] Hsu YT, Wang YR, Wu SK, Chen C. Effect of CO 2 Laser Welding on the Shape-Memory and Corrosion Characteristics of TiNi Alloys 2001;32:569–76.

[33] Crăciunescu C, Mitelea I. Combined effects in quasidisimilar NiTi joints manufactured by pulsed laser welding. Mater Sci Eng A 2018;737:364–72. doi:10.1016/j.msea.2018.09.014.

[34] Wang W, Yang X, Li H, Cong F, Liu Y. Effect of Laser Welding Parameters on Formation of NiTi Shape Memory Alloy Welds 2014;2014.

[35] Tam B, Khan MI, Zhou Y. Mechanical and Functional Properties of Laser-Welded Ti-55 . 8 Wt Pct Ni Nitinol Wires 2011:2166–75. doi:10.1007/s11661-011-0639-6.

[36] Chan CW, Man HC, Yue TM. Effects of Process Parameters upon the Shape Memory and Pseudo-Elastic Behaviors of Laser-Welded NiTi Thin Foil 2011. doi:10.1007/s11661-011-0623-1.

[37] Mehrpouya M, Gisario A, Brotzu A, Natali S. Laser welding of NiTi shape memory sheets using a diode laser. Opt Laser Technol 2018;108:142–9. doi:10.1016/j.optlastec.2018.06.038.

[38] Weglowski MS, S B, A P. Electron beam welding- Techniques and trends-Review. Vacuum 2016;130:72–92. doi:10.1016/j.vacuum.2016.05.004.

[39] Yang D, Jiang HC, Zhao MJ, Rong LJ. Microstructure and mechanical behaviors of electron beam welded NiTi shape memory alloys. Mater Des 2014;57:21–5.

[40] Ikai A, Kimura K. TIG Welding and Shape Memory Effect of TiNi Shape Memory Alloy. J Intell Mater Syst Struct 1996;7:646–55.

[41] Oliveira JP, Barbosa D, Fernandes FMB, Miranda RM. Tungsten inert gas (TIG) welding of Ni-rich NiTi plates : functional behavior. Smart Mater Struct 2016;25.

[42] Eijk C Van Der, Fostervoll H, Sallom ZK, Akselsen OM. Plasma Welding of NiTi to NiTi , Stainless Steel and Hastelloy C276. ASM Mater Solut Conf

2003:13–5.

[43] Delobelle V, Delobelle P, Liu Y, Favier D, Louche H. Resistance welding of NiTi shape memory alloy tubes. J Mater Process Tech 2013;213:1139–45. doi:10.1016/j.jmatprotec.2013.01.013.

[44] Nishikawa M, Tanaka H, Kohda M, Nagaura T, Watanabe K, Nishikawa M, et al. BEHAVIOUR OF WELDED PART OF Ti-Ni SHAPE MEMORY. J Phys Colloq 1982.

[45] Tam B, Pequegnat A, Khan MI. Resistance Microwelding of Ti-55 . 8 wt pct Ni Nitinol Wires and the Effects of Pseudoelasticity. Metall Mater Trans A 2012;43. doi:10.1007/s11661-012-1115-7.

[46] Lohwasser D, Chen Z, editors. Friction stir welding: From basics to applications. Woodland publishing limited; 2009.

[47] Mishra RS, Ma ZY. Friction stir welding and processing. Mater Sci Eng R 2005;50:1–78. doi:10.1016/j.mser.2005.07.001.

[48] Padhy GK, Wu CS, Gao S. Friction stir based welding and processing technologies - processes, parameters, microstructures and applications: A review. J Mater Sci Technol 2018;34:1–38. doi:10.1016/j.jmst.2017.11.029.

[49] Chowdhury SM, Chen DL, Bhole SD, Cao X. Tensile properties of a friction stir welded magnesium alloy: Effect of pin tool thread orientation and weld pitch. Mater Sci Eng A 2010;527:6064–75. doi:10.1016/j.msea.2010.06.012.

[50] Lee WB, Jung SB. The joint properties of copper by friction stir welding. Mater Lett 2004;58:1041–6. doi:10.1016/j.matlet.2003.08.014.

[51] Gangwar K, Ramulu M. Friction stir welding of titanium alloys: A review. Mater Des 2018;141:230–55. doi:10.1016/j.matdes.2017.12.033.

[52] Liu FC, Hovanski Y, Miles MP, Sorensen CD, Nelson TW. A review of friction stir welding of steels: Tool, material flow, microstructure, and properties. J Mater Sci Technol 2018;34:39–57. doi:10.1016/j.jmst.2017.10.024.

[53] London B, Mahoney M, Pelton A. Use of Friction Stir Processing and Friction Stir Welding For Nitinol Medical Devices. United States Pat Appl Publ 2006:US 2006/0283918 Al.

[54] Barcellona A, Fratini L, Palmeri D, Maletta C, Brandizzi M, Engineering M. Friction stir processing of NiTi Shape Memory Alloy: Microstructural Characterization. Int J Mater Form 2010;3:1047–50.

[55] Blair L, Jennifer F, Alan P, Christian F, Murrey M. Friction stir processing of Nitinol. Frict Stir Weld Process III 2005:67–74.

[56] Shinoda T, Owa T, Magula V. Microstructural analysis of friction welded joints in TiNi alloy. Weld Int 1999;13:180–5. doi:10.1080/09507119909447361.

[57] Shinoda T, Tsuchiya T, Takahashi H. Functional properties of friction welded near-Equiatomic TiNi shape memory alloy. Trans Japan Weld Soc 1991;22.

[58] Zhang W, Ao SS, Oliveira JP, Zeng Z, Luo Z, Hao ZZ. Effect of ultrasonic spot welding on the mechanical behaviour of NiTi shape memory alloys. Smart Mater Struct 2018;27. doi:10.1016/j.jhazmat.2007.01.073.

[59] Zhang W, Ao S, Oliveira JP, Zeng Z, Huang Y, Luo Z. Microstructural characterization and mechanical behavior of NiTi shape memory alloys ultrasonic joints using Cu interlayer. Materials (Basel) 2018;11. doi:10.3390/ma11101830.

[60] Juntao L, Yanjun Z, Lishan C. Effects of severe plastic deformation and heat treatment on transformation behavior of explosively welded duplex TiNi−TiNi. Pet Sci 2007;4:107–12. doi:10.1007/bf03187464.

[61] Yan Z, Cui LS, Zheng YJ. Microstructure and martensitic transformation behaviors of explosively welded NiTi/NiTi laminates. Chinese J Aeronaut 2007;20:168–71. doi:10.1016/S1000-9361(07)60027-2.

[62] XING T yong, ZHENG Y jun, CUI L shan, MI X jun. Influence of aging on damping behavior of TiNi/TiNi alloys synthesized by explosive welding. Trans Nonferrous Met Soc China (English Ed 2009;19:1470–3.

doi:10.1016/S1003-6326(09)60053-4.

[63] Li J, Zheng Y, Cui L. Transformation characteristics of TiNi/TiNi alloys synthesized by explosive welding. Front Mater Sci China 2007;1:351–5. doi:10.1007/s11706-007-0065-2.

[64] Jiang X, Jiang D, Zheng Y, Cui L. Transformation behavior of explosively welded TiNi/TiNi laminate after diffusion annealing and aging. Mater Res Bull 2013;48:5033–5. doi:10.1016/j.materresbull.2013.04.031.

[65] Xing T, Zheng Y, Cui L. Transformation and Damping Characteristics of NiTi/NiTi Alloys Synthesized by Explosive Welding. Mater Trans 2006;47:658–60. doi:10.2320/matertrans.47.658.

[66] Belyaev S, Rubanik V, Resnina N, Rubanik V, Lomakin I. Functional properties of "Ti50Ni50-Ti 49.3Ni50.7" shape memory composite produced by explosion welding. Smart Mater Struct 2014;23. doi:10.1088/0964-1726/23/8/085029.

[67] Senkevich KS. A Study of the microstructure of diffusion joints of TiNi-base alloys. Met Sci Heat Treat 2014;55:675–9. doi:10.1007/s11041-014-9689-x.

[68] Senkevich KS, Shlyapin SD. Investigation of the process of diffusion bonding of alloys based on titanium nickelide. Weld Int 2012;26:736–8. doi:10.1080/09507116.2011.653156.

[69] Kejanli H, Ta M. Transient liquid phase (tlp) diffusion bonding of Ti 45 Ni 49 Cu 6 P / M components using Cu interlayer. Int J Adv Manuf Technol 2009:695–9. doi:10.1007/s00170-008-1860-3.

[70] Otsuka K, Ren X. Physical metallurgy of Ti-Ni-based shape memory alloys. Prog Mater Sci 2005;50:511–678. doi:10.1016/j.pmatsci.2004.10.001.

[71] Frenzel J, Wieczorek A, Opahle I, Maaß B, Drautz R, Eggeler G. On the effect of alloy composition on martensite start temperatures and latent heats in Ni-Ti-based shape memory alloys. Acta Mater 2015;90:213–31. doi:10.1016/j.actamat.2015.02.029.

[72] Frenzel J, George EP, Dlouhy A, Somsen C, Wagner MF, Eggeler G.

Influence of Ni on martensitic phase transformations in NiTi shape memory alloys. Acta Mater 2010;58:3444–58.

[73] Chan CW, Man HC, Yue TM. Effects of Process Parameters upon the Shape Memory and Pseudo-Elastic Behaviors of Laser-Welded NiTi Thin Foil. Metall Mater Trans A 2011;42A:2264–70. doi:10.1007/s11661-011-0623-1.

[74] Oliveira JP, Barbosa D, Fernandes FMB, Miranda RM. Tungsten inert gas (TIG) welding of Ni-rich NiTi plates : functional behavior. Smart Mater Struct 2016;25:1–7. doi:10.1088/0964-1726/25/3/03LT01.

[75] Oliveira JP, Fernandes FMB, Schell N, Miranda RM. Shape memory effect of laser welded NiTi plates. Funct Mater Lett 2015;8:1–5. doi:10.1142/S1793604715500691.

[76] Schmidt HNB. Material flow in butt friction stir welds in AA2024-T3. Acta Mater 2006;54:1199–209. doi:10.1016/j.actamat.2005.10.052.

[77] Guerra M, Schmidt C, Mcclure JC, Murr LE, Nunes AC. Flow patterns during friction stir welding. Mater Charact 2003;49:95–101. doi:10.1016/S1044-5803(02)00362-5.

[78] Kumar R, Pancholi V, Bharti RP. Material flow visualization and determination of strain rate during friction stir welding. J Mater Process Tech 2018;255:470–6. doi:10.1016/j.jmatprotec.2017.12.034.

[79] Zhu XK, Chao YJ. Numerical simulation of transient temperature and residual stresses in friction stir welding of 304L stainless steel. J Mater Process Tech 2004;146:263–72. doi:10.1016/j.jmatprotec.2003.10.025.

[80] Sadeghian B, Taherizadeh A, Atapour M. Simulation of weld morphology during friction stir welding of aluminum- stainless steel joint. J Mater Process Tech 2018;259:96–108. doi:10.1016/j.jmatprotec.2018.04.012.

[81] Prasanna P, Rao BS, Rao GKM. Finite element modeling for maximum temperature in friction stir welding and its validation 2010:925–33. doi:10.1007/s00170-010-2693-4.

[82] Chen ZW, Cui S. Strain and strain rate during friction stir welding /

processing of Al-7Si-0 . 3Mg alloy. IOP Conf Ser Mater Sci Eng 2009;012026. doi:10.1088/1757-899X/4/1/012026.

[83] Arora A, Zhang Z, De A, Debroy T. Strains and strain rates during friction stir welding. Scr Mater 2009;61:863–6. doi:10.1016/j.scriptamat.2009.07.015.

[84] Nandan R, Roy GG, Lienert TJ, Debroy T. Numerical modelling of 3D plastic flow and heat transfer during friction stir welding of stainless steel. Sci Technol Weld Join 2006;11:526–37. doi:10.1179/174329306X107692.

[85] Khandkar MZH, Khan JA, Reynolds AP. Prediction of temperature distribution and thermal history during friction stir welding : input torque based model. Sci Technol Weld Join 2003:165–74. doi:10.1179/136217103225010943.

[86] Prabu SSM, Mithun R, Muralidharan M, Nath T. Thermo-mechanical behavior of shape memory alloy spring actuated using novel scanning technique powered by ytterbium doped continuous fi ber laser. Smart Mater Struct 2019;28.

[87] Lee HT, Kim MS, Lee GY, Kim CS, Ahn SH. Shape Memory Alloy (SMA)-Based Microscale Actuators with 60% Deformation Rate and 1.6 kHz Actuation Speed. Small 2018;14. doi:10.1002/smll.201801023.

[88] Hu Z, Rajini Kanth B, Tamang R, Varghese B, Sow CH, Mukhopadhyay PK. Visible microactuation of a ferromagnetic shape memory alloy by focused laser beam. Smart Mater Struct 2012;21. doi:10.1088/0964-1726/21/3/032003.

[89] Zaidi S, Lamarque F, Prelle C, Carton O, Zeinert A. Contactless and selective energy transfer to a bistable micro-actuator using laser heated shape memory alloy. Smart Mater Struct 2012;21. doi:10.1088/0964-1726/21/11/115027.

[90] Okamura H, Yamaguchi K, Ono R. Light-driven actuator with shape memory alloy for manipulation of macroscopic Objects. Int J Optomechatronics 2009;3:277–88. doi:10.1080/15599610903391150.

[91] Carton O, Lejeune M, Lamarque F, Zaidi S, Zeinert A. Thermo-mechanical

characterization of optical thin films filters deposited onto shape memory alloy micro-actuators. Smart Mater Struct 2014;23. doi:10.1088/0964-1726/23/12/125035.

[92] Yan XJ, Yang DZ. Corrosion resistance of a laser spot-welded joint of NiTi wire in simulated human body fluids. J Biomed Mater Res - Part A 2006;77:97–102. doi:10.1002/jbm.a.30378.

[93] Chan CW, Man HC, Yue TM. Susceptibility to stress corrosion cracking of NiTi laser weldment in Hanks' solution. Corros Sci 2012;57:260–9. doi:10.1016/j.corsci.2011.12.010.

[94] Yan XJ, Yang DZ, Liu XP. Corrosion behavior of a laser-welded NiTi shape memory alloy. Mater Charact 2007;58:623–8. doi:10.1016/j.matchar.2006.07.010.

[95] Bharathi D, Kannan T, Sathiya P, Ramesh T. Experimental investigation and characterization of laser welded NiTinol shape memory alloys. J Manuf Process 2017;25:253–61. doi:10.1016/j.jmapro.2016.12.006.

[96] Yan XJ, Yang DZ, Liu XP. Electrochemical behavior of YAG laser-welded NiTi shape memory alloy. Trans Nonferrous Met Soc China (English Ed 2006;16:572–6. doi:10.1016/S1003-6326(06)60100-3.

[97] Dong P, Yao R, Yan Z, Yan Z, Wang W, He X, et al. Microstructure and corrosion resistance of laser-welded crossed nitinol wires. Materials (Basel) 2018;11. doi:10.3390/ma11050842.

[98] Datta S, Raza MS, Saha P, Pratihar DK. Effects of process parameters on the quality aspects of weld-bead in laser welding of NiTinol sheets. Mater Manuf Process 2019;34:648–59. doi:10.1080/10426914.2019.1566608.

[99] Ye C, Cheng GJ. Controlled Nanocrystallization of NiTi Shape Memory Alloy by Laser Shock Peening. Proc ASME 2011 Int Manuf Sci Eng Conf 2011:443–8. doi:10.1115/msec2011-50294.

[100] Zhang R, Mankoci S, Walters N, Gao H, Zhang H, Hou X, et al. Effects of laser shock peening on the corrosion behavior and biocompatibility of a

nickel–titanium alloy. J Biomed Mater Res - Part B Appl Biomater 2018:1–10. doi:10.1002/jbm.b.34278.

[101] Ye C, Suslov S, Fei X, Cheng GJ. Bimodal nanocrystallization of NiTi shape memory alloy by laser shock peening and post-deformation annealing. Acta Mater 2011;59:7219–27. doi:10.1016/j.actamat.2011.07.070.

[102] Wang H, Pöhl F, Yan K, Decker P, Gurevich EL, Ostendorf A. Effects of femtosecond laser shock peening in distilled water on the surface characterizations of NiTi shape memory alloy. Appl Surf Sci 2019;471:869–77. doi:10.1016/j.apsusc.2018.12.087.

[103] Hu T, Xin YC, Wu SL, Chu CL, Lu J, Guan L, et al. Corrosion behavior on orthopedic NiTi alloy with nanocrystalline/amorphous surface. Mater Chem Phys 2011;126:102–7. doi:10.1016/j.matchemphys.2010.11.061.

[104] Hu T, Wen CS, Sun GY, Wu SL, Chu CL, Wu ZW, et al. Wear resistance of NiTi alloy after surface mechanical attrition treatment. Surf Coatings Technol 2010;205:506–10. doi:10.1016/j.surfcoat.2010.07.023.

[105] Hu T, Chu CL, Wu SL, Xu RZ, Sun GY, Hung TF, et al. Microstructural evolution in NiTi alloy subjected to surface mechanical attrition treatment and mechanism. Intermetallics 2011;19:1136–45. doi:10.1016/j.intermet.2011.03.020.

[106] Hu T, Chen L, Wu SL, Chu CL, Wang LM, Yeung KWK, et al. Graded phase structure in the surface layer of NiTi alloy processed by surface severe plastic deformation. Scr Mater 2011;64:1011–4. doi:10.1016/j.scriptamat.2011.02.008.

[107] Hu T, Wen CS, Lu J, Wu SL, Xin YC, Zhang WJ, et al. Surface mechanical attrition treatment induced phase transformation behavior in NiTi shape memory alloy. J Alloys Compd 2009;482:298–301. doi:10.1016/j.jallcom.2009.04.004.

[108] Nandan R, Debroy T, Bhadeshia HKDH. Recent advances in friction-stir welding – Process , weldment structure and properties. Prog Mater Sci 2008;53:980–1023. doi:10.1016/j.pmatsci.2008.05.001.

[109] Pourali M, Abdollah-zadeh A, Saeid T, Kargar F. Influence of welding parameters on intermetallic compounds formation in dissimilar steel / aluminum friction stir welds. J Alloys Compd 2017;715:1–8. doi:10.1016/j.jallcom.2017.04.272.

[110] Chen H, Fu L, Liang P. Microstructure , texture and mechanical properties of friction stir welded butt joints of 2A97 Al-Li alloy ultra-thin sheets. J Alloys Compd 2017;692:155–69. doi:10.1016/j.jallcom.2016.08.330.

[111] Mishra RS, Ma ZY. Friction stir welding and processing. Mater Sci Eng R 2005;50:1–78. doi:10.1016/j.mser.2005.07.001.

[112] Zhang Y, Jiang S, Hu L. Investigation of Dynamic Recrystallization of NiTi shape memory alloy subjected to local canning compression. Metals (Basel) 2017:1–10. doi:10.3390/met7060208.

[113] Huang K, Logé RE. A review of dynamic recrystallization phenomena in metallic materials. Mater Des 2016;111:548–74. doi:10.1016/j.matdes.2016.09.012.

[114] Sakai T, Belyakov A, Kaibyshev R, Miura H, Jonas JJ. Dynamic and post-dynamic recrystallization under hot , cold and severe plastic deformation conditions. Prog Mater Sci 2014;60:130–207. doi:10.1016/j.pmatsci.2013.09.002.

[115] Jiang S, Zhang Y, Zhao Y. Dynamic recovery and dynamic recrystallization of NiTi shape memory alloy under hot compression deformation. Trans Nonferrous Met Soc China 2013;23:140–7.

[116] Dixit S, Madhu HC, Kailas S V, Chattopadhyay K. Role of insert material on process loads during FSW. Int J Adv Manuf Technol 2017.

[117] Jiang S, Zhang Y, Zhao Y. Dynamic recovery and dynamic recrystallization of NiTi shape memory alloy under hot compression deformation. Trans Nonferrous Met Soc China 2013;23:140–7. doi:10.1016/S1003-6326(13)62440-1.

[118] Yang D, Jiang HC, Zhao MJ, Rong LJ. Microstructure and mechanical

behaviors of electron beam welded NiTi shape memory alloys. Mater Des 2014;57:21–5.

[119] Cullity BD. Elements of X-Ray diffraction. Addison-Wesley publishing company, Inc; n.d.

[120] Zeng Z, Yang M, Oliveira JP, Song D, Peng B. Laser welding of NiTi shape memory alloy wires and tubes for multi-functional design applications. Smart Mater Struct n.d.;25:1–10.

[121] Wang J, Su J, Mishra RS, Xu R, Baumann JA. Tool wear mechanisms in friction stir welding of Ti-6Al-4V alloy. Wear 2014;321:25–32. doi:10.1016/j.wear.2014.09.010.

[122] Siddiquee AN, Pandey S. Experimental investigation on deformation and wear of WC tool during friction stir welding (FSW) of stainless steel. Int J Adv Manuf Technol 2014;73:479–86. doi:10.1007/s00170-014-5846-z.

[123] Mani Prabu SS, Madhu HC, Perugu CS, Akash K, Mithun R, Kumar PA, et al. Shape memory effect, temperature distribution and mechanical properties of friction stir welded nitinol. J Alloys Compd 2019;776:334–45. doi:10.1016/j.jallcom.2018.10.200.

[124] Rai R, De a, Bhadeshia HKDH, DebRoy T. Review: friction stir welding tools. Sci Technol Weld Join 2011;16:325–42. doi:10.1179/1362171811Y.0000000023.

[125] Kato H, Yasuda Y, Sasaki K. Thermodynamic assessment of the stabilization effect in deformed shape memory alloy martensite. Acta Mater 2011;59:3955–64.

[126] Evirgen A, Karaman I, Santamarta R, Pons J, Hayrettin C, Noebe RD. Relationship between crystallographic compatibility and thermal hysteresis in Ni-rich NiTiHf and NiTiZr high temperature shape memory alloys. Acta Mater 2016;121:374–83.

[127] Roca P La, Isola L, Vermaut P, Malarría J. Relationship between grain size and thermal hysteresis of martensitic transformations in Cu-based shape

memory alloys. Scr Mater 2017;135:5–9.

[128] Chansoria P, Solanki P, Dasgupta MS. Parametric study of transient temperature distribution in FSW of 304L stainless steel. Int J Adv Manuf Technol 2015:1223–39. doi:10.1007/s00170-015-7102-6.

[129] Song M, Kovacevic R. Thermal modeling of friction stir welding in a moving coordinate system and its validation. Int J Mach Tools Manuf 2003;43:605–15. doi:10.1016/S0890-6955(03)00022-1.

[130] R V vignesh, R P, M A, S, Thirumalini J G, Ram MSSS. Numerical modelling of thermal phenomenon in friction stir welding of aluminum plates. IOP Conf Ser Mater Sci Eng 2016. doi:10.1088/1757-899X/149/1/012208.

[131] Roy BS, Medhi T, Saha SC. Material Flow Modeling in Friction Stir Welding of AA6061-T6 Alloy and Study of the Effect of Process Parameters. Int J Mater Metall Eng 2015;9:658–66.

[132] Cho J, Boyce DE, Dawson PR. Modeling strain hardening and texture evolution in friction stir welding of stainless steel 2005;398:146–63. doi:10.1016/j.msea.2005.03.002.

[133] Jing N. Investigation of the bouncing behaviour of two rubber balls. Mettler Toledo Therm Anal Usercom 40 n.d.:1–4.

[134] Zahedi F, Amiri I. Carboxylated multiwalled carbon nanotubes effect on dynamic mechanical behavior of soft fi lms composed of multilayer polymer structure. Polymer (Guildf) 2018;151:187–96. doi:10.1016/j.polymer.2018.07.044.

[135] Saud SN, Hamzah E, Abubakar T. Effect of Ta Additions on the Microstructure , Damping , and Shape Memory Behaviour of Prealloyed Cu-Al-Ni Shape Memory Alloys. Scanning 2017;2017. doi:10.1155/2017/1789454.

[136] Mielczarek A, Riehemann W, Vogelgesang S, Tonn B. Mechanical and fatigue properties of Cu - Al - Mn shape memory alloys with influence of mechanical cycling on amplitude dependence of internal friction at room

temperature. Solid State Phenom 2008;137:145–54. doi:10.4028/www.scientific.net/SSP.137.145.

[137] Jose, Grassi. Dynamic Properties of NiTi Shape Memory Alloy and Classic Structural Materials : A Comparative Analysis Dynamic properties of NiTi shape memory alloy and classic structural materials : a comparative analysis DA SILVA Niédson José 1a , GRASSI Estephanie No. Mater Sci Forum 2010. doi:10.4028/www.scientific.net/MSF.643.37.

[138] Patil D, Song G. A Review of Shape Memory Material's Applications in the Offshore Oil and Gas Industry. Smart Mater Struct 2017;26. doi:10.1039/b000000x/1.

[139] Xin Y, Wu S, Yeung K. Corrosion products and mechanism on NiTi shape memory alloy in physiological environment. J Mater Res 2010:350–8. doi:10.1557/JMR.2010.0051.

[140] Gao A, Hang R, Bai L, Tang B, Chu PK. Electrochimica Acta Electrochemical surface engineering of titanium-based alloys for biomedical application. Electrochim Acta 2018;271:699–718. doi:10.1016/j.electacta.2018.03.180.

[141] Ralston KD, Birbilis N, Davies CHJ. Revealing the relationship between grain size and corrosion rate of metals. Scr Mater 2010;63:1201–4. doi:10.1016/j.scriptamat.2010.08.035.

[142] Ralston KD, Birbilis N. Effect of Grain Size on Corrosion : A Review. Corrosion 2010;66:1–13.

[143] Mishra RS, Ma ZY. Friction stir welding and processing. Mater Sci Eng R Reports 2005;50:1–78. doi:10.1016/j.mser.2005.07.001.

[144] Reynolds AP. Visualisation of material flow in autogenous friction stir welds. Sci Technol Weld Join 2000;5:120–4.

[145] Zhang D, Zeng W, Zi Z, Chu PK. Corrosion resistance of TiN coated biomedical nitinol under deformation. Mater Sci Eng C 2009;29:1599–603. doi:10.1016/j.msec.2008.12.022.

[146] Wang S, Li Y, Zhao T. Effect of thermal oxidation on the surface characteristics and corrosion behavior of a Ta-implanted Ti-50 . 6Ni shape memory alloy. Int J Miner Metall Mater 2012;19:1134–41. doi:10.1007/s12613-012-0682-3.

[147] Hassel AW. medical treatment of NiTi for applications. Minim Invasive Ther Allied Technol 2004;13:240–7.

[148] Neelakantan L, Swaminathan S, Spiegel M, Eggeler G, Walter A. Selective surface oxidation and nitridation of NiTi shape memory alloys by reduction annealing. Corros Sci 2009;51:635–41. doi:10.1016/j.corsci.2008.12.018.

[149] Aliofkhazraei M, editor. Handbook of mechanical nanostructuring. WILEY-VCH; 2015.

[150] Taylor P, Azadmanjiri J, Berndt CC, Kapoor A, Wen C, Azadmanjiri J, et al. Development of Surface Nano-Crystallization in Alloys by Surface Mechanical Attrition Treatment (SMAT). Crit Rev Solid State Mater Sci 2014. doi:10.1080/10408436.2014.978446.

[151] Laser shock peening:Performance and proces simulation. Woodland publishing limited; n.d.

[152] Gujba AK, Medraj M. Laser Peening Process and Its Impact on Materials Properties in Comparison with Shot Peening and Ultrasonic Impact Peening. Materials (Basel) 2014:7925–74. doi:10.3390/ma7127925.

[153] Guo W, Sun R, Song B, Zhu Y, Li F, Che Z, et al. Surface & Coatings Technology Laser shock peening of laser additive manufactured Ti6Al4V titanium alloy. Surf Coatings Technol 2018;349:503–10.

[154] Sathyajith S, Kalainathan S, Swaroop S. Optics & Laser Technology Laser peening without coating on aluminum alloy Al-6061-T6 using low energy Nd : YAG laser. Opt Laser Technol 2013;45:389–94.

[155] Liu KT, Duh JG. Grain size effects on the corrosion behavior of Ni50.5 Ti49.5 and Ni45.6Ti49.3Al5.1 film. J Electroanal Chem 2008;618:45–52. doi:10.1016/j.jelechem.2008.02.020.

[156] Wang XY, Li DY. Mechanical and electrochemical behavior of nanocrystalline surface of 304 stainless steel. Electrochim Acta 2002;47:3939–47.

[157] Balakrishnan A, Lee BC, Kim TN, Panigrahi BB. Corrosion Behaviour of Ultra Fine Grained Titanium in Simulated Body Fluid. Trends Biomater Artif Organs 2008;22:58–64.

[158] Sarlak H, Atapour M, Esmailzadeh M. Corrosion behavior of friction stir welded lean duplex stainless steel. Mater Des 2015;66:209–16. doi:10.1016/j.matdes.2014.10.060.

[159] Liu Q, Ma Q, Chen G, Cao X, Zhang S, Pan J, et al. Enhanced corrosion resistance of AZ91 magnesium alloy through refinement and homogenization of surface microstructure by friction stir processing. Corros Sci 2018;138:284–96. doi:10.1016/j.corsci.2018.04.028.

[160] Nie FL, Zheng YF, Cheng Y, Wei SC, Valiev RZ. In vitro corrosion and cytotoxicity on microcrystalline , nanocrystalline and amorphous NiTi alloy fabricated by high pressure torsion. Mater Lett 2010;64:983–6. doi:10.1016/j.matlet.2010.01.081.

[161] Olumi S, Sadrnezhaad SK, Atai M. The Influence of Surface Nanocrystallization Induced by Shot Peening on Corrosion Behavior of NiTi Alloy. J Mater Eng Perform 2015;24:3093–9. doi:10.1007/s11665-015-1570-6.